**Modulating Cardiac Dynamics: The Prediction, Prevention and Control of Cardiac Alternans**

A DISSERTATION
SUBMITTED TO THE FACULTY OF
UNIVERSITY OF MINNESOTA
BY

**Kanchan Kulkarni**

IN PARTIAL FULFILLMENT OF THE REQUIREMENTS
FOR THE DEGREE OF
DOCTOR OF PHILOSOPHY

Adviser: Dr. Alena Talkachova

December 2017

without the support of and constant encouragement by my parents and sister. My friends here in Minnesota have been my extended family and made graduate school fun and fulfilling!

**Dedication**

This thesis is dedicated to my family, Jyoti, Vijay, Ketki, Amit, Urvi and Kyro.
For their eternal love, and faith in me.

## Table of Contents

## List of Tables

# List of Figures

x

# CHAPTER 1: INTRODUCTION

## 1.1 Overview of Cardiac Electrophysiology and Arrhythmias

The human heart is a fascinating machine whose mechanical and electrical synergy creates a powerful and efficient dynamic system that beats tirelessly over two billion times in an average lifespan. It comprises an intricate synchronous electrical system whose rhythmic activation enables the mechanical contraction and relaxation that result in a heartbeat. An abnormal heart rhythm (arrhythmia) can be caused by functional irregularities in cardiac electrical activity. Arrhythmias are exhibited as unstable variations in cardiac cellular electrical impulses, also known as action potential durations (APDs). An alarming number of people have been reported to manifest sudden cardiac death (SCD) as the first symptom of cardiac arrhythmias, leading to an estimated 600,000 fatalities per year. Efforts for decreasing this substantial number have led to the proliferation of medical devices, aimed at restoring the normal electrical activity in diseased and failing hearts, with over 3 million pacemaker implantations reported in the past decade. However, given the complex spatiotemporal dynamics and non-linearity of the human heart, *predicting the onset of arrhythmias and preventing the transition from steady state to unstable rhythms has been an extremely challenging task.*

In order for the heart to function properly, it needs to contract and relax in a coordinated fashion. The mechanical contractions of the heart are triggered by electrical waves of excitation propagating through the cardiac tissue. In healthy hearts, the electrical impulses originate in the heart's own natural pacemaker, the sinoatrial (SA) node in the

right atrium. From the SA node, the electrical impulse excites the atria and causes it to contract. Then, after a short delay to allow enough time for the ventricles to fill up, the electrical wave travels through the atrioventricular (AV) node, which serves as the electrical connection between the atria and the ventricles, to the Purkinje fibers via the Bundle of His. Finally, the Purkinje fibers will carry the electrical wave to the ventricles causing them to contract. Fig.1.1 depicts the cellular electrical activity corresponding to different regions of the heart and its correlation to the average activity recorded on an electrocardiogram (ECG).
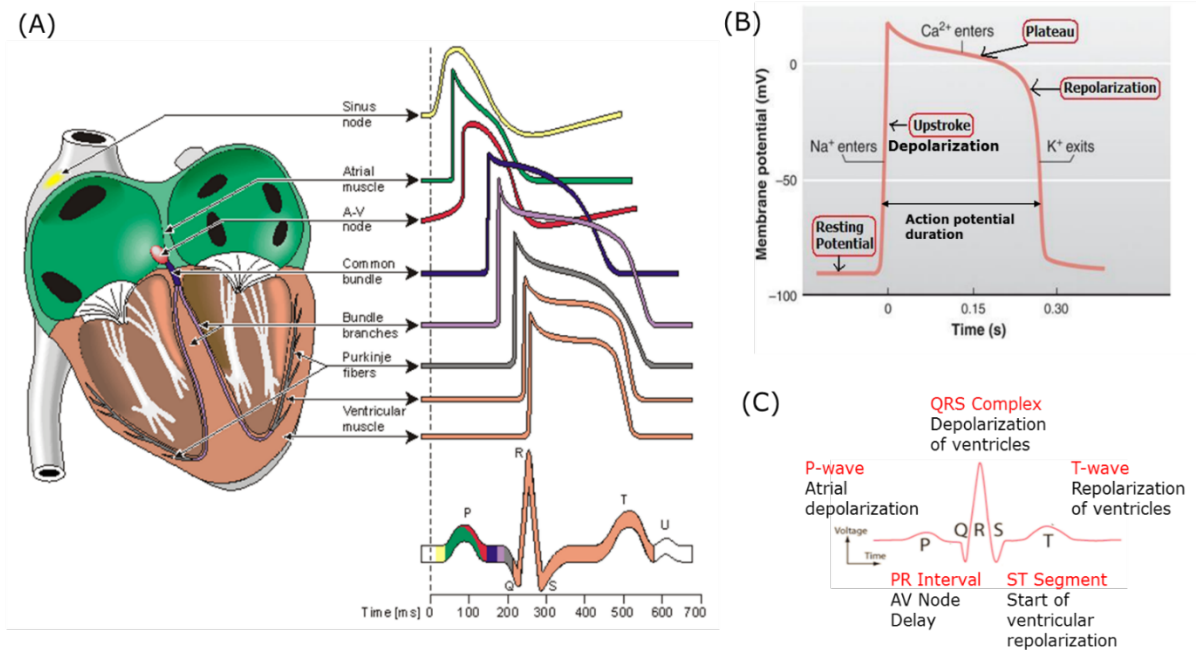


*Figure 1.1. (A) [Adapted from (Malmivuo and Plonsey, 'Bioelectromagnetism')] Electrophysiology of the heart with voltage or action potential waveforms for each region shown distinctly along with cumulative ECG trace. (B) Ventricular action potential trace showing different phases of activation. (C) Correlation between ECG trace and activation of different regions of the heart.*

The contraction of the heart is a phenomenon that is brought about by a well-timed summation of single cardiomyocyte contractions. The contraction of each myocyte is triggered by the electrical wave of excitation that originates from the SA node as discussed in the previous section. Each time a myocyte is triggered, the properties of transmembrane ion channels (e.g. sodium, potassium, calcium, etc.) change and a complex movement of ions in and out of the cell takes place, thereby causing a cyclic change in the membrane potential. This sequence of changes in the membrane potential is known as the action potential. The action potential of one myocyte will act as the stimulus to surrounding cells through gap junctions and diffusion, thus, eliciting an action potential in downstream cells in the conduction system. This process is repeated until the electrical signal propagates through the entire heart causing it to contract.

Arrhythmias are any abnormality in the rhythm or normal electrical conduction system of the heart, as described previously. Some common types of arrhythmias are described in Table 1.1.

| Type of Arrhythmia | Description |
|---|---|
| Ventricular Tachycardia (VT) | Regular but rapid heart rhythm of the ventricles, resulting in abnormally high heart rates. |
| Ventricular Fibrillation (VF) | Irregular, chaotic, and rapid ventricular rhythm that causes the ventricles to quiver. This results in the |

| | heart to not be able to contract or pump blood. |
|---|---|
| Atrial Fibrillation (AF) | Irregular, chaotic rhythm of the atria. This causes no atrial hemodynamic input to the ventricles and the stasis of blood in the atria can result in clot formation and stroke. |
| Atrial Flutter or Tachycardia | Abnormally high atrial rate. |
| Bradycardia | Slow heart rhythm. |
| Heart block | Electrical activity in the heart is either disrupted or completely blocked as the impulse travels from the SA node to the ventricles. |

*Table 1.1. Common examples of cardiac arrhythmias.*

## 1.2 Current Pacemakers and Therapies

Cardiac pacemakers are being used as a therapeutic device to regulate the heart function and rhythm in patients with abnormal cardiac electrical activity. From treatment of bradycardia, heart block and ventricular dysfunction to defibrillation devices that reset the electrical activity, a vast array of devices have been designed to regulate cardiac function. Past two decades have seen an immense improvement in the pacemaker technology, yet they have had limited efficiency in arrhythmia prevention due to two major drawbacks. Firstly, the pacing schemes in contemporary pacemakers are based on periodic

stimulation approach. In periodic stimulation there is a dependence of the diastolic interval (DI) (cardiac relaxation phase), on the preceding APD leading to an inherent feedback. The presence of feedback makes the heart more susceptible to electrical destabilization and formation of alternans, a beat-to-beat alternation of the APD in the heart. Observed as a periodic variation in the amplitude or shape of the T-wave in an electrocardiogram (ECG), alternans is believed to be a direct precursor to ventricular fibrillation (VF) or abnormal disordered electrical activity of the heart [1-4]. VF can then lead to SCD which is one of the leading causes of natural death in the US. Previous studies have established a plausible link between alternans and ventricular arrhythmias suggesting that elimination of alternans could lead to the prevention of VF and eventual arrhythmias in the heart [3, 5-7].

Secondly, there has been an increasing need for a more physiologically relevant pacing technique with one approach being to incorporate heart rate variability (HRV) information in pacemakers. Under normal conditions, the heart rate is never constant and is a cumulative result of a complex interplay between different physiological systems. Clinically, low HRV has been known to be a marker of arrhythmias [8-11]. However, recent numerical simulations have shown that incorporation of HRV in pacing can have a contradictory pro-arrhythmic effect in the presence of feedback, while being ineffective in the absence of feedback [12]. Understanding the effect of HRV on feedback modulation forms an important aspect in the design and development of anti-arrhythmic pacing.

Inspite of the above mentioned shortcomings, *most contemporary pacemakers still use periodic stimulation to restore normal cardiac rhythm, potentially promoting electrical instability in the heart*. This creates a pressing need to better understand paced cardiac

dynamics and develop anti-arrhythmic pacing techniques that would prevent cardiac arrhythmias. ***The focus of my research was to develop and implement a novel anti-arrhythmic pacing mechanism that eliminates the inherent electrical instabilities of periodic pacing and prevents abnormal cardiac rhythms.***

## 1.3 Organization of Thesis

**Chapter 2** presents an overview of the electrophysiological concepts pertinent to the research and elaborates on the concepts of 'Restitution', 'Feedback' and 'Cardiac Alternans'. Background information on paced cardiac dynamics and the use of high resolution optical mapping for the study of cardiac arrhythmias is also provided. The rest of the thesis is divided into three main parts:

**PART 1:** Prediction of cardiac alternans: Here, **Chapter 3** describes the pacing methodology used to induce alternans and the analytical, non-linear dynamical approach used to characterize the bifurcation to alternans from steady state cardiac rhythm. Details of the experimental investigations performed and the results are also provided. The goal of this project was to implement a pacing technique that can be used to characterize the transition to alternans, which in turn could be potentially used to predict the onset of alternans prior to their occurrence.

**PART 2:** Prevention and Control of alternans: **Chapter 4** elaborates the preliminary experiments performed to investigate the effect of incorporating stochasticity or HRV, in periodic pacing. This study utilized the traditional open loop optical imaging technique to compare the propensity of stochastic and periodic pacing, to the temporal onset of alternans. **Chapter 5** details the design and implementation of a novel, real-time

closed loop system that enables beat-by-beat cardiac control. Furthermore, it details the experiments performed using the closed loop control system, to investigate the anti-arrhythmic benefits of 'feedback elimination' (Constant DI pacing) compared with a) traditional periodic pacing that has 'feedback inherent'; and b) pacing with HRV which corresponds to 'feedback modulation'. This encompasses a detailed spatio-temporal assessment of the effect of feedback elimination using beat-to-beat cardiac control, on the prevention and control of cardiac alternans.

**PART 3:** Investigating effects of parasympathetic modulation of the heart: **Chapter 6** describes an investigative study performed to evaluate the effects of modulating the M2R-Girk4-RGS6 dependent parasympathetic pathway using isolated whole murine hearts. The chapter details the structural and ventricular electrophysiological effects of parasympathetic stimulation in mice with gain and loss-of parasympathetic function.

**Chapter 7** summarizes the work completed as part of this dissertation by highlighting the major findings and discussing the possible future directions for different aspects of this research.

# CHAPTER 2: BACKGROUND

## 2.1 Paced Cardiac Dynamics

The heart comprises of excitable cells that elicit an electrical signal (voltage) in response to a stimulus. As described briefly in the preceding section, cardiomyocytes fire an action potential with each electrical stimulus applied. Action potential firing is an all-or-nothing phenomenon wherein a sub-threshold stimulus would elicit no response while a super-threshold stimulus would generate an action potential. As shown in Fig.2.1, the rate of firing of action potentials can also be controlled by changing the rate of stimulation or the time duration between two consecutive stimuli, denoted here as the Basic Cycle Length (BCL). As we decrease the BCL, we observe a shortening in APD as action potentials fire at a faster rate. This shortening in APD with increase in heart rate is known as electrical restitution.
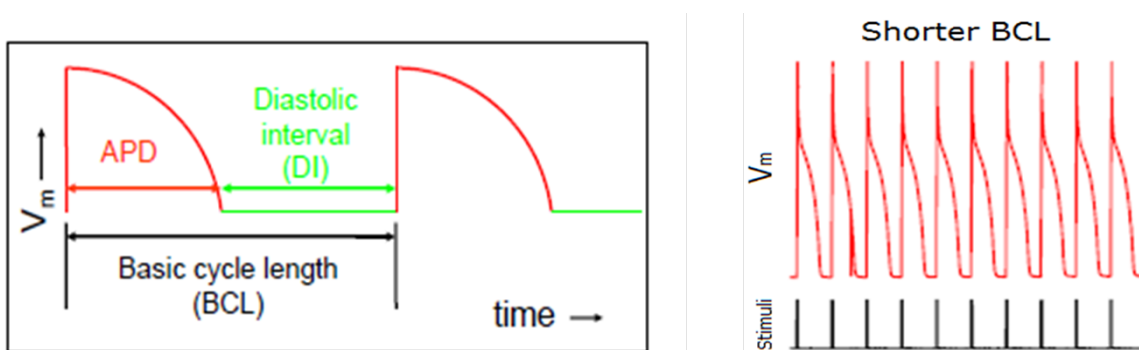


*Figure 2.1: Paced cardiac response (black lines indicate stimuli)*

## 2.2 Electrical Restitution and Cardiac Alternans

Electrical restitution is a fundamental characteristic of cardiac cells and plays a vital role in maintaining stable electrical function of the heart. At a given heart rate, a shorter

8

APD enables a longer DI interval and in turn, sufficient time for the heart to refill with blood. As the heart is paced at progressively increasing rates, it bifurcates from a constant APD response at lower frequencies to alternating long-short APD, or alternans, at higher frequencies [13-15]. As seen from Fig.2.2, under normal conditions, the heart elicits an action potential (AP) for every electrical stimulus applied. A sufficiently large basic cycle length (BCL), time interval between two consecutive stimuli, ensures a constant identical AP for every stimulus, leading to a 1:1 response. However, as the BCL is decreased, at a certain pacing rate the heart transitions to a 2:2 alternating long-short AP response, giving rise to alternans.
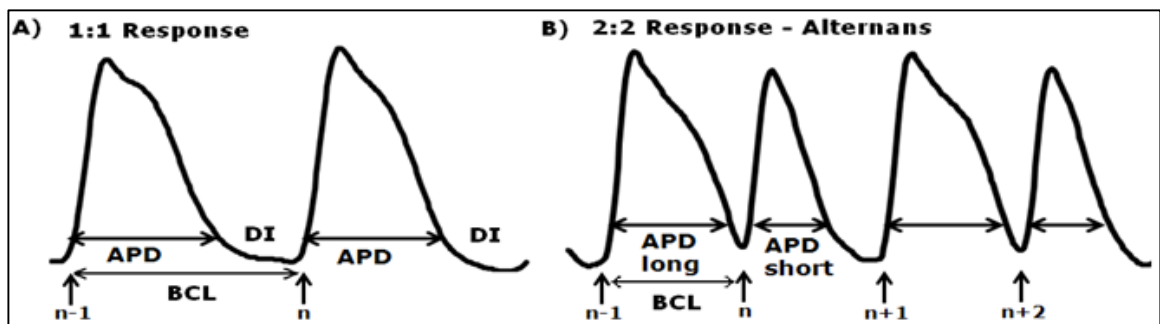


*Figure 2.2: Action potential traces showing A) Constant APD at higher BCL; B) APD alternans at lower BCL*

## 2.3 Feedback

In one of the first studies to characterize APD alternans formation, Nolasco and Dahlen used a one-dimensional mapping model with the assumption of constant periodic pacing [16]. Specifically, they proposed that the APD generated by the (n+1)[st] stimulus, $APD_{n+1}$, was completely determined by the preceding DI, $DI_n$:

$$APD_{n+1} = f(DI_n) \tag{1}$$

9

where, $f$ is the restitution curve. For periodic stimulation, APD and DI are also related through the pacing relation:

$$APD_n + DI_n = BCL \qquad (2)$$

where, $BCL_n = BCL$ is constant. Under Eq.2, there is a partial dependence of the DI on the preceding APD leading to an inherent feedback.

Fig.2.3 illustrates the concept of feedback during periodic stimulation. The feedback curve represented by Eq. 2 has a slope of -1 during periodic pacing (Fig.2.2B). It can be seen from the cobweb diagrams in Fig.2.3, that different responses are generated under the pacing relation of Eq.2 and depending on the slope of restitution. Stable 1:1 responses are elicited for a slope less than one, whereas we get unstable electrical activity and alternans for a slope greater than one. The APD responses for these representative cases are shown in Fig.2.4.
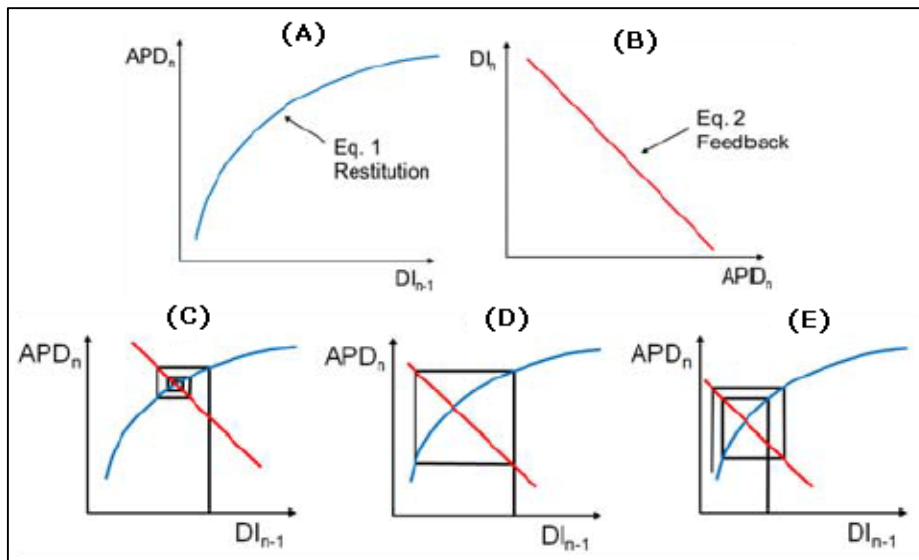


*Figure 2.3: A), B) Representative curves for Eqs. 1 and 2 respectively; C), D) and E) Cobweb diagrams for mapping model in Eq.1 combined with periodic pacing, for restitution slope S< 1, S = 1 and S > 1 respectively*

Based on Eqs.1 and 2, the restitution hypothesis was proposed and alternans was predicted to occur when the magnitude of the slope of the restitution curve, S, exceeded one [7, 13, 17], i.e.

$$S = |f'| \geq 1 \tag{3}$$
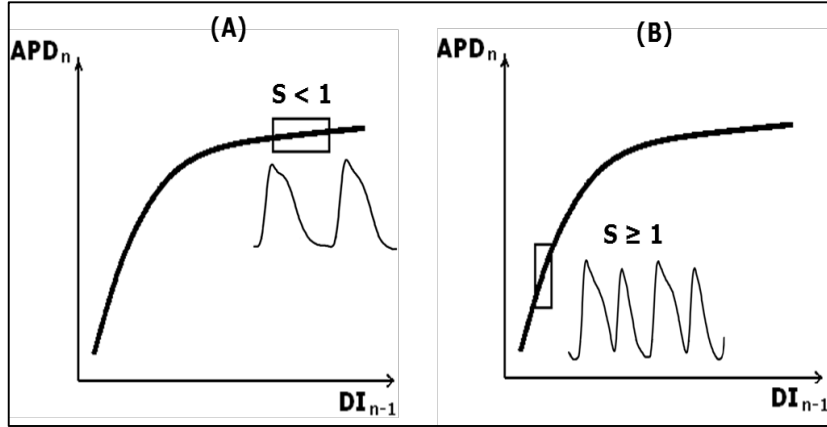


*Figure 2.4: APD restitution curve; A) Stable 1:1 response for S<1; B) APD alternans at for S ≥1*

This led to the proposition that flattening the slope of the restitution curve can help prevent the formation of alternans and eventual VF, with several experimental studies demonstrating the correlation of alternans with steep restitution slopes [13-15].

The presence of feedback causes small changes in DI to translate into subsequent changes in the APD, thus enhancing the electrical instability in the heart [12, 18-21]. Maintaining a constant DI would eliminate the pacing relation given by Eq.2 making the formation of alternans mathematically inexplicable. In the absence of feedback, the mapping model in Eq.1 would return a single constant $APD_{n+1}$ value for a fixed $DI_n$. Based on Eq.2, the following relation can be derived:

$$\Delta DI_{n,n-1} = -\Delta APD_{n,n-1} \tag{4}$$

11

Eq.4 describes the feedback inherent in periodic pacing and indicates that small changes in DI are inversely proportional to small changes in APD. Based on Eq.4, the slope of restitution can be modified to the following:

$$\Delta APD_{n+1,n} = S\left(-\Delta APD_{n,n-1}\right) \tag{5}$$

It is apparent from Eq.5 that for a slope S < 1, small changes in APD die out whereas for S > 1, small changes in APD get enhanced during subsequent pacing cycles leading to electrical instability of the heart. However, by maintaining a constant DI, the relation between APD and DI expressed by Eq.2 can be eliminated, thus eliminating feedback. In this case we would generate a constant APD during each pacing cycle corresponding to the fixed DI.
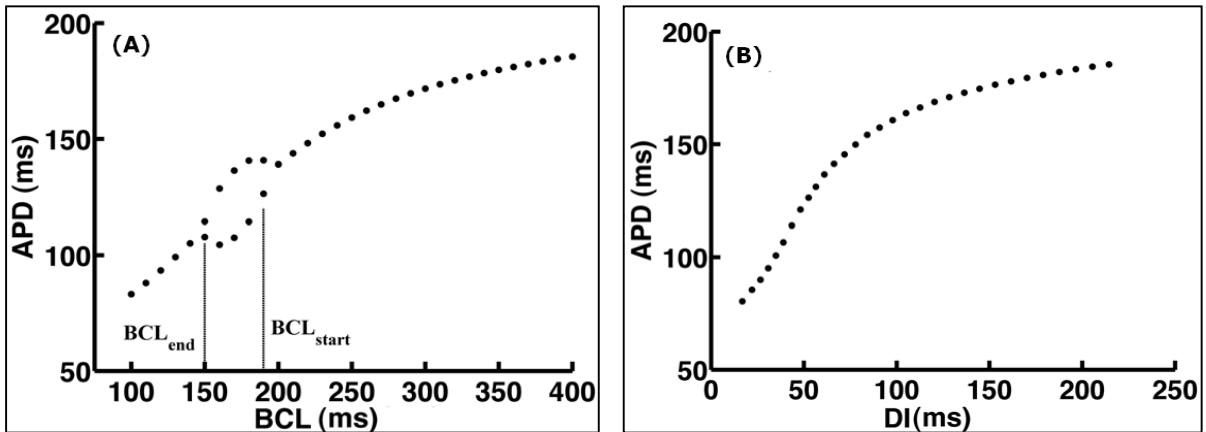


*Figure 2.5: Change in APD for an ionic model of a canine cardiac action potential paced with A) periodic pacing protocol with constant BCL; B) constant DI pacing protocol[12]*

Numerical simulation results of the proposed anti-arrhythmic effects of feedback elimination have been published recently [12, 22]. Figs.2.5A and B, show the formation of alternans as BCL is progressively decreased for the case of periodic and constant DI pacing protocols respectively. As seen from Fig.2.5, elimination of feedback by maintaining a constant DI prevented the formation of alternans in an ionic model of isolated cardiac

myocyte. Thus, eliminating feedback and the dependence of DI on preceding APD could control the formation of alternans and have beneficial anti-arrhythmic effects.

## 2.4  Heart Rate Variability

Another important physiological phenomenon that needs consideration is the presence of HRV and its effect on feedback modulation in the heart. HRV ensures deviation of the heart from constant periodic beating under normal conditions and is modulated by various physiological factors like sympathetic and parasympathetic nerve activity, thermoregulation, respiration, etc [23]. HRV, the variation in time interval between heartbeats, can be observed as a change in the RR interval on the ECG (Fig.2.6).
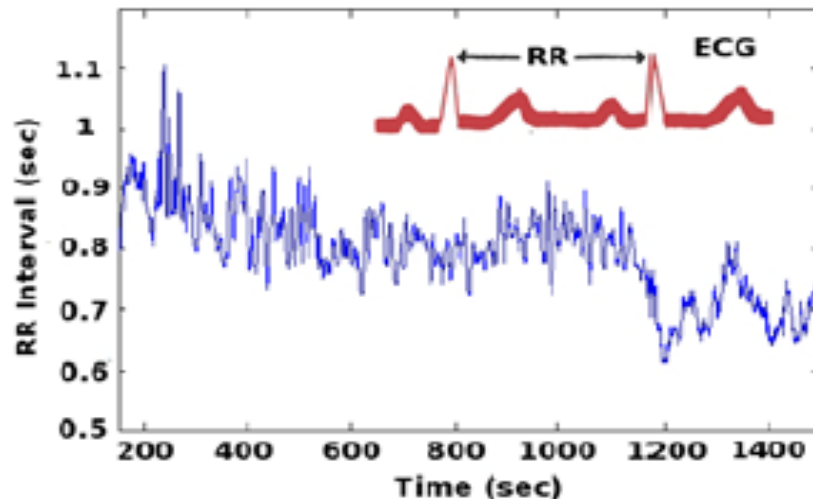


*Figure 2.6: ECG trace of adult male during sinus rhythm* [24]

A major limitation of the restitution hypothesis apart from its basis on periodic pacing, is the fact that it does not account for the presence of physiological HRV, which can alter cardiac dynamics and hence, the prediction of alternans. HRV can modulate the feedback characteristics, leading to different effects in the presence and absence of feedback. In order to investigate the formation and prevention of alternans, the current

concept of electrical restitution needs to be extended to a more realistic and physiologically relevant pacing scheme, by incorporation of HRV in pacing.

## 2.5 Need and Significance of Feedback Elimination

Implantable pacemakers and cardioverter defibrillators are being therapeutically used in patients to restore normal cardiac function [25-27]. Cardioverter defibrillators use real time heart rate sensing to detect irregular rhythms and shock the heart to save the patient from lethal arrhythmias. Various control algorithms have been developed and implemented in pacemakers enabling detection of irregular cardiac rhythms and application of rate responsive stimulation for modulation of heart rate [25, 27]. Contemporary pacemakers are designed to override the abnormal sinus rhythm and stimulate the heart at a constant periodic rate in an attempt to modulate and stabilize the heart. However, an anti-arrhythmic pacemaker with a physiologically relevant pacing scheme that potentially prevents the formation of alternans and eventual VF is yet to be implemented.

There is great interest and an urgent clinical need in deciphering the mechanisms that lead to unstable electrical substrates in the heart and developing pacing techniques that prevent irregular rhythms. Over the past two decades, several groups have attempted the control of alternans through *in-silico*, *in-vitro* and *ex-vivo* experiments [6, 12, 21, 22, 28-34]. The late 1990s and early 2000s reported positive results in controlling alternans in single cell models and in-vitro preparations. They mainly utilized an adaptive negative feedback algorithm that adjusted the pacing cycle length based on the amplitude of alternans [6, 29, 30]. However, control of alternans in more spatiotemporally complex 2D settings proved unsuccessful. Eschebarria and Karma [31] adeptly highlighted the challenges in the

14

spatiotemporal control of cardiac alternans revealing that the control failed above a critical cable length. Similar findings were reported by Christini et.al [33] where control became attenuated spatially as the alternans amplitude increased. These studies highlighted two important shortcomings in the control of alternans. *First,* given the spatiotemporal complexity of the heart, a 2D feedback system is essential to evaluate the spatiotemporal onset of alternans. *Second,* a major flaw in the control algorithms was the use of constant pacing cycle lengths or periodic stimulation.

A new control algorithm that eliminated the dependence of DI on the preceding APD was implemented by Jordan and Christini [32] and shown to control alternans in a 1D Purkinje fiber *in-silico* study. Controlling the DI on a beat-by-beat basis ensures a dual purpose. *First,* constant DI ensures that the heart always gets enough time to relax at the end of an activation cycle. And *second*, it implies that the succeeding APD in every cycle is independent of any prior electrical irregularities. Control over the DI becomes even more critical in diseased hearts with diastolic dysfunction and impaired ventricular relaxation where periodic stimulation could further instigate electrical instabilities. Recently, the beneficial anti-arrhythmic effects of feedback elimination, by keeping the DI constant, in comparison to traditional periodic pacing were reported using single cell and 1D cable numerical simulations [12, 22]. Controlling and maintaining a *Constant DI* on a beat-by-beat basis, i.e.

$$DI_n = DI = constant \qquad\qquad (2)$$

eliminated feedback and the inherent dependence of the DI on the preceding APD, which was successful in suppressing alternans [12, 22]. However, closed loop experimental

validation of beat-to-beat control of alternans has exhibited limited success, especially in 2D cardiac tissue preparations [21, 31, 33, 34]. This is primarily since experimental implementation of *Constant DI* pacing is quite challenging and previous attempts involving the control of DI were limited to point sensing using microelectrodes, which failed to address the prevention of alternans in the heart. In order to precisely control the DI in the whole heart, on a beat-to-beat basis, there is a need to develop a sophisticated control algorithm that can sense an action potential in real-time based on comprehensive cardiac electrical information, and apply a stimulus after a predefined time interval at the end of the APD.

An important focus of my research was to develop a real-time beat-to-beat control system to successfully implement *Constant DI* pacing and demonstrate its efficacy in suppressing alternans in the whole heart. We successfully addressed the technical limitations mentioned previously and implemented a novel method to validate the anti-arrhythmic benefits of feedback elimination using *Constant DI*, in *ex-vivo* isolated whole rabbit hearts using high resolution 2D optical mapping. The proposed algorithm opens the doors for the modulation of cardiac electrical activity in real-time, during various diseased states and abnormal rhythms. Successful validation of the anti-arrhythmic benefits of this pacing technique and its adaptation into a clinically viable device can radically improve the quality of life of patients suffering from diastolic dysfunction, impaired ventricular relaxation and abnormal cardiac rhythms. Crossing traditional boundaries and integrating research from multiple disciplines, this research holds promise in translating theoretical findings into a clinically useful therapeutic device.

## 2.6 Optical Mapping for Study of Cardiac Arrhythmias

The field of cardiac electrophysiology has focused on gaining a better understanding of the electrophysiological properties of the healthy and diseased heart and the electromechanical coupling between cardiomyocytes and tissues to gain important insights into the mechanisms of life threatening cardiac arrhythmias, which can cause heart attacks or in extreme dangerous cases, sudden cardiac death. Optical mapping is a widely used technique in the preclinical research setting to study the electrical activity in the heart and cardiac cells in both healthy and diseased states. It's an imaging modality that utilizes fluorescent dyes to look at physiological parameters (i.e. changes in membrane potential) at both high temporal and spatial resolutions. In the past 20 years, optical mapping has enhanced our understanding of complex arrhythmias and the electrophysiological remodeling that occurs during disease states. Furthermore, it has also aided in the development and evaluation of several therapeutic strategies and pacing protocols for the treatment of cardiovascular diseases [35-37].

Optical mapping enables recording the electrical activity (action potentials) from isolated whole mammalian hearts. Excised animal hearts are kept alive and beating *ex-vivo* using external perfusion. Voltage-sensitive dyes are injected into the heart and excited with the use of a laser. Optical movies corresponding to the emitted fluorescence signal are then recorded from the epicardial surface of the heart by fast, high resolution CCD cameras. Traditionally, optical mapping has been an 'open loop' technique wherein optical videos recorded during experiments are post processed to extract APD and other

electrophysiological information. Fig.2.7 shows a schematic of a typical optical mapping setup.
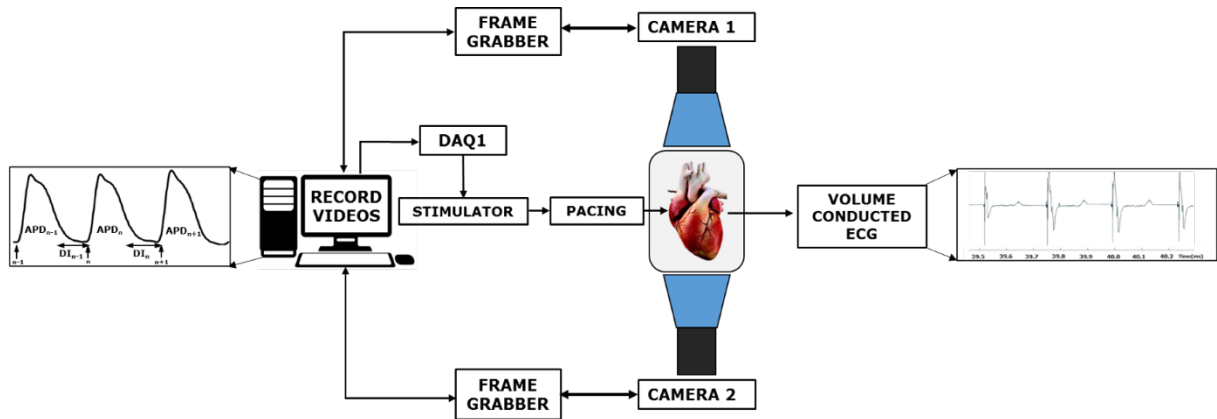


*Figure 2.7: Schematic of open loop optical mapping setup*

Implementing and integrating a real-time beat-to-beat cardiac control algorithm with the existing optical mapping setup formed a critical aspect of my research. This was achieved by developing a novel control algorithm to detect T-waves from real-time ECG data on a beat-by-beat basis, integrated with conventional optical mapping. Fig.2.8 shows a schematic of the setup interfacing the real-time ECG based beat-to-beat control algorithm with high resolution optical mapping.

Optical mapping has been widely used over the past decades to visualize, predict and control the onset of abnormal cardiac rhythms, such as alternans. It provides a unique opportunity to visualize and quantitatively assess the spread of electrical activity by recording action potentials simultaneously from multiple locations in both normal cardiac rhythms and arrhythmic episodes. The use of optical mapping to extract specific electrophysiological information and assess data is described separately for each study in the following chapters, based on the application.

18
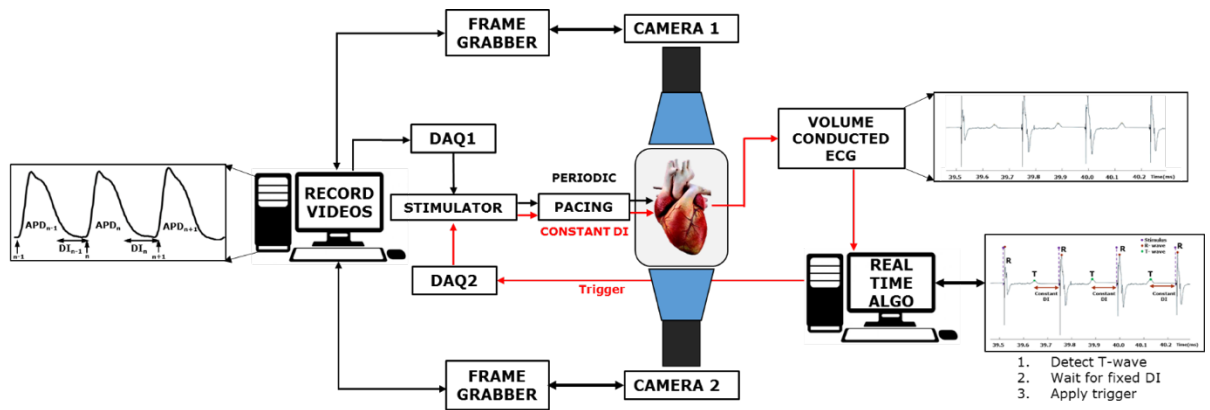
*Figure 2.8: Schematic of the optical mapping system for real-time closed loop control of alternans. Red arrows highlight the real-time ECG T-wave detection and Constant DI algorithm implementation. Black arrows indicate 2D optical imaging and implementation of Periodic pacing.*

# CHAPTER 3: SPATIAL DYNAMICS OF BIFURCATION TO ALTERNANS

(The work in this chapter was published in Kanchan Kulkarni, Ramjay Visweswaran, Xiaopeng Zhao, and Elena G. Tolkacheva, "Characterizing Spatial Dynamics of Bifurcation to Alternans in Isolated Whole Rabbit Hearts Based on Alternate Pacing," BioMed Research International, vol. 2015, Article ID 170768, 8 pages, 2015. doi:10.1155/2015/170768) [38]

Author Contributions:

Concept was developed by E.G.T. and X.Z. Pacing protocol was implemented by K.K. based on previous theoretical work published by X.Z. Optical mapping experiments were designed by K.K. and E.G.T. and implemented by K.K and R.V. Data was analyzed by K.K. and prepared for publication by K.K. and E.G.T.

**Abstract**

Sudden cardiac death instigated by ventricular fibrillation (VF) is the largest cause of natural death in the USA. Alternans, a beat- to-beat alternation in the action potential duration, has been implicated as being pro-arrhythmic. The onset of alternans is mediated via a bifurcation, which may occur through either a smooth or a border-collision mechanism. The objective of this study was to characterize the mechanism of bifurcation to alternans based on experiments in isolated whole rabbit hearts. High resolution optical mapping was performed and the electrical activity was recorded from the left ventricle (LV) epicardial surface of the heart. Each heart was paced using an "alternate pacing protocol," where the basic cycle length (BCL) was alternatively perturbed by $\pm\delta$. Local onset of alternans in the heart, BCLstart, was measured in the absence of perturbations ($\delta = 0$) and was defined as the BCL at which 10% of LV exhibited alternans. The influences of perturbation size were investigated at two BCLs: one prior to $BCL_{start}$ ($BCL_{prior} = BCL_{start} + 20$ ms) and one preceding $BCL_{prior}$ ($BCL_{far} = BCL_{start} + 40$ ms). Our results demonstrate significant spatial correlation of the region exhibiting alternans with smooth bifurcation characteristics, indicating that transition to alternans in isolated rabbit hearts occurs predominantly through smooth bifurcation.

**3.1 Introduction**

Ventricular fibrillation (VF), manifesting as chaotic unsynchronized electrical activity in the heart, is known to cause sudden cardiac death (SCD). SCD is one of the largest natural causes of death, killing more than 300,000 people annually in the United States [39, 40]. Alternans has been implicated as being pro-arrhythmic and a potential source

21

of cardiac instability [1-4]. Electrical restitution can cause the heart to bifurcate from a constant APD response at lower frequencies to an alternating long-short APD pattern (alternans) at higher frequencies [13-15]. Characterizing this bifurcation can provide useful insights into understanding the dynamics of the cardiac system. In particular, knowledge of the bifurcation type that governs the transition to alternans can potentially be used as a means to predict the formation of alternans prior to their onset [41], which may be useful in preventing arrhythmias.

Previous research has implicated both smooth and border-collision bifurcations when trying to characterize the transition to alternans in small cardiac tissue. Initially, Nolasco and Dahlen modeled transition to alternans as a smooth bifurcation [16]; however, later studies reported a border-collision type of bifurcation to alternans [42]. More recently, it was shown that a more complex bifurcation model involving the coexistence of both smooth and border-collision characteristics may exist in the heart. Based on experiments on adult bullfrog ventricular tissue samples, Berger et al. suggested the existence of a smooth-like behavior close to the bifurcation point and a border-collision type behavior further away from the bifurcation point [43]. Although the presence of different bifurcation characteristics in small tissue samples suggests very interesting dynamical behavior, their study was limited by the use of glass microelectrode recordings taken at single point locations. Therefore, the spatial distribution of the bifurcation characteristics and their correlation to alternans remains to be validated.

The main objective of this study was to experimentally investigate the spatial dynamics of bifurcations that governs the transition to alternans in isolated whole rabbit

hearts. For this purpose, we applied an *"alternate pacing protocol,"* originally introduced by Heldstab et al. [44] and further experimentally investigated by Berger et al. [43]. Theoretical studies by Zhao et al. [45, 46] show that smooth and border-collision bifurcations to alternans demonstrate qualitatively different trends in their response to this alternate pacing protocol. We aimed to use this protocol to characterize the type of bifurcation to alternans and study its spatial distribution across the left ventricular (LV) surface of the heart. We also aimed to investigate the spatial correlation between the regions of the heart exhibiting alternans and the different bifurcation characteristics.

## 3.2 Methods

### *3.2.1 Optical Mapping*

All experiments were performed in accordance with the guidelines of the Institutional Animal Care and Use Committee at the University of Minnesota. New Zealand White rabbits (Bakkom Rabbitry, 1.3–2.0kg, $n = 4$) were injected with heparin sulfate (550 U/100 g) and anesthetized with ketamine and xylazine (35 mg/kg and 5mg/kg, resp.), as described previously [47, 48]. After a thoracotomy was performed, the heart was quickly removed and immersed in cardioplegic solution (in mM: glucose 280, KCl 13.44, NaHCO3 12.6, and mannitol 34). The aorta was quickly cannulated and retrogradely perfused with warm (37 $\pm$ 1∘C) oxygenated Tyrode's solution (in mM: NaCl 130, $CaCl_2$ 1.8, KCl 4, $MgCl_2$ 1.0, $NaH_2PO_4$ 1.2, $NaHCO_3$ 24, glucose 5.5, and pH 7.4) under constant pressure. The heart was immersed in a chamber and superfused with the same Tyrode's solution. Blebbistatin (10 $\mu$M) was added to Tyrode's solution to reduce motion artifacts.

A bolus of 4 mL of the voltage-sensitive dye di-4-ANEPPS ($10\mu$M) was injected and excited with the use of a diode- pumped, continuous-excitation green laser (532nm, 1W; Shanghai Dream Lasers Technology, Shanghai, China). Optical movies corresponding to the fluorescence signal were recorded from the epicardial surface of the LV by fast (1000 frames per second) 14-bit resolution, 80 × 80-pixel resolution camera (Little Joe, RedShirt Imaging, SciMeasure) after a period of stabilization (~30 minutes).

### *3.2.2 Alternate Pacing Protocol*

External stimuli (5 ms duration, twice the threshold) were applied to the base of the LV surface of the isolated Langendorff-perfused rabbit hearts and the following alternate pacing protocol [43] was applied (see Fig.3.1).

(1) Forty stimuli at a constant BCL (denoted by $B_0$) value were applied to achieve steady state (SS).

(2) Forty alternating stimuli were applied at $BCL_n = B_0 + (-1) \delta$, where $\delta = 5$ ms is the perturbation amplitude.

(3) Steps (1) and (2) were repeated for $\delta$ values of 10, 15, and 20 ms, respectively.

The baseline BCL $B_0$ was progressively reduced from 300 ms down to 160 ms in steps of 20 ms. Optical movies were acquired to capture the responses to last ten stimuli during Steps (1) and (2) for each BCL. The alternate pacing protocol was repeated twice for each heart, so a total of 8 protocols were analyzed across all hearts.
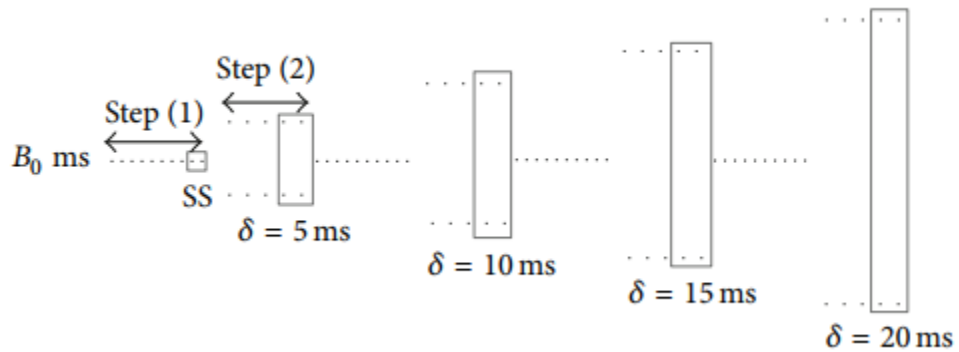
*Figure 3.1: Schematic of the alternate pacing protocol for a specific BCL $B_0$. Grey boxes indicate responses that have been captures during optical mapping experiments. Local onset of alternans was calculated bases in steady state (SS) responses at $\delta = 0$, while alternans induced by perturbations was calculated based on responses captured at increasing $\delta$ values.*

### 3.2.3 Data Analysis

At each baseline BCL $B_0$, APD was measured at 80% repolarization for each pixel. The APD responses for the last ten stimuli captured were divided in pairs and the amplitude of alternans was calculated as the absolute difference between even and odd APD responses: $\Delta APD = |APD_{even} - APD_{odd}|$. The average amplitude of alternans was calculated across all five pairs, and the temporal threshold for APD alternans was set at 5ms. Two-dimensional (2D) alternans maps corresponding to SS responses (see Fig.3.2) were generated for the LV surface for each baseline BCL and were used to identify the local spatial onset of alternans ($BCL_{start}$) in the heart as described previously [47]. Specifically, $BCL_{start}$ was identified as the SS $B_0$ at which at least 10% of the LV surface exhibited

25

alternans. The baseline BCL $B_0$ just prior to BCL$_{start}$ was denoted by BCL$_{prior}$, and the BCL preceding BCL$_{prior}$ was denoted by BCL$_{far}$. Furthermore, the alternans was identified as either spatially discordant or spatially concordant based on the presence or absence of alternans with opposite phases, respectively [49]. Alternans was considered as spatially discordant if at least 5% of the alternans exhibited had opposite phases. Table 3.1 shows the total number of either type of steady state alternans for BCL$_{start}$, as well as alternans induced by $\delta = 5$ ms perturbations for BCL$_{prior}$ and BCL$_{far}$.

| BCL | Total protocols (4 rabbits, 8 protocols total) | # of spatially concordant alternans | # of spatially discordant alternans |
|---|---|---|---|
| BCL$_{start}$ | 8 | 3 | 5 |
| BCL$_{prior}$ ($\delta = 5$ ms) | 8 | 6 | 2 |
| BCL$_{far}$ ($\delta = 5$ ms) | 8 | 6 | 2 |

*Table 3.1: Classification of spatial pattern of alternans as concordant or discordant alternans for BCL$_{start}$, BCL$_{prior}$ and BCL$_{far}$ for all experiments.*

At each pixel, an amplification Gain was calculated as described previously [14]:

$$\text{Gain} = \frac{|\Delta APD|}{2\delta}. \tag{1}$$

Theoretical investigations in [45] demonstrate that the Gain versus $\delta$ relation exhibits a decreasing trend as $\delta$ increases for smooth bifurcation, whereas the Gain versus $\delta$ relation exhibits an increasing trend as $\delta$ increases for border- collision bifurcation. At each pixel,

26

Gain was calculated for each $\delta$ at $BCL_{prior}$ and $BCL_{far}$, respectively. Then, the dependence of Gain on $\delta$ was fitted using a linear curve at $BCL_{prior}$ and $BCL_{far}$, respectively. The correlation coefficient $R$-square was then calculated to evaluate the quality of fitting. For $R$-square $> 0.4$, a decrease or increase in Gain with $\delta$ was identified as smooth or border-collision bifurcation, respectively. To account for experimental noise, a threshold of 0.07 (or smaller) between consecutive Gain values was considered acceptable while determining the trend. The bifurcation was considered as undetermined if the $R$-square $<$ 0.4 or if the consecutive Gain difference $> 0.07$. All data are presented as mean ± standard error. Statistical comparisons between the three bifurcation types were performed using ANOVA (Origin Software, Northampton, MA, USA). Values of $P < 0.05$ were considered statistically significant.

## 3.3 Results

### *3.3.1 Spatial Distribution of Bifurcation Characteristics*

First, we studied the local onset of SS alternans (Step (1) of alternate pacing protocol) and alternans that are induced by small perturbations $\delta$ (Step (2) of the alternate pacing protocol). Fig.3.2(a) shows a representative example of the 2D alternans maps generated for different baseline BCLs $B_0$ at SS. Here, blue and red regions indicate the presence of spatially discordant alternans (see color bar for alternans phases) while the white regions indicate the absence of alter- nans. In this example, the local onset of alternans, $BCL_{start}$ (red box), occurred at 160 ms since more than 10% of the LV was occupied by alternans at this BCL. Consequently, $BCL_{prior}$ and $BCL_{far}$ (green and blue boxes) were identified as 180 ms and 200 ms, respectively. Fig.3.2(b) shows 2D maps illustrating the development

27

of alternans induced by small perturbations $\delta$ that were applied at $BCL_{prior}$ and $BCL_{far}$. Note that alternans is spatially discordant for $BCL_{prior}$ and spatially concordant for $BCL_{far}$. At both $BCL_{prior}$ and $BCL_{far}$, we observed that the heart was more prone to the formation of alternans as the perturbation size $\delta$ was increased, which is indicated by the progressive increase in the red and blue color as $\delta$ increases.
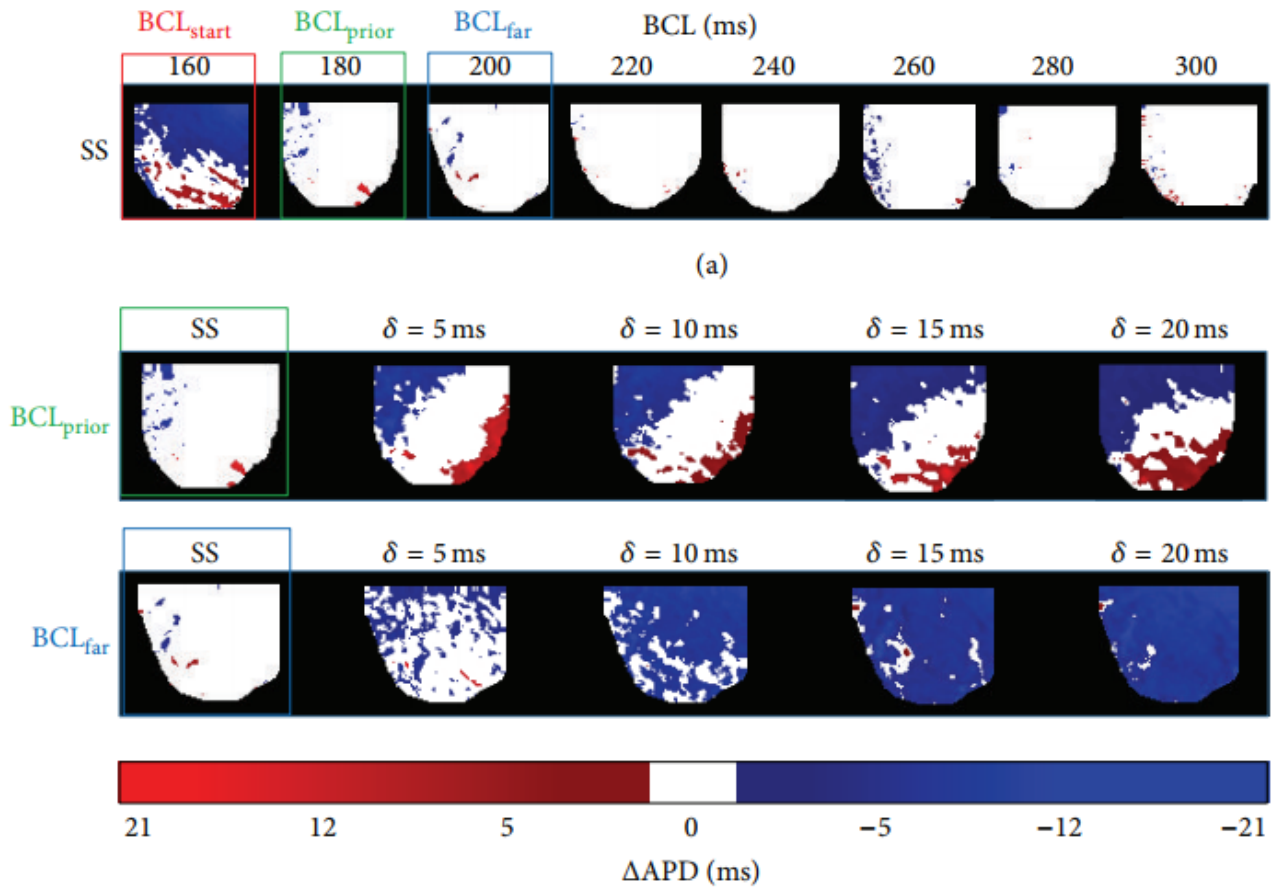


Figure 3.2: (a) Representative 2D alternans maps for SS BCLs showing the local onset of alternans at $BCL_{start}$ (red box). Two prior BCLs, $BCL_{prior}$ and $BCL_{far}$, are also shown (green and blue boxes). (b) 2D alternans maps induced by perturbations $\delta$ at $BCL_{prior}$ and $BCL_{far}$. Color bar represents the amplitude of alternans.

It has been previously demonstrated, using numerical simulations [45], that bifurcation to alternans can be identified by looking at the changes in the amplification Gain as a function of $\delta$. Therefore, for each $\delta$ we constructed 2D Gain maps to investigate the spatial distribution of the changes in Gain. Fig.3.3(a) shows a representative example of 2D Gain maps that were generated for BCL$_{prior}$ from Fig.3.2(b), showing the spatial distribution of Gain for various $\delta$.

Fig.3.3(b) illustrates three representative single-pixel examples from Fig.3.3(a) (#, $\Phi$, and $*$) indicating the presence of different trends in Gain as a function of $\delta$. It has been shown previously that a decrease in Gain with increase in $\delta$ indicates the presence of smooth bifurcation (see pixel # in Fig.3.3(b)), while an increase in Gain with an increase in $\delta$ characterizes border-collision bifurcation (see pixel $\Phi$ in Fig.3.3(b)) [43, 45]. We also found that at some pixels the type of bifurcation could not be determined (see pixel $*$ in Fig.3.3(b)).

Fig.3.3(c) shows a representative 2D bifurcation map demonstrating the spatial distribution of different bifurcations for panel (a). Here, the region in black corresponds to the area of the heart (60.7%) that went to alternans through smooth bifurcation, the region in blue indicates border- collision bifurcation (16.8%), and bifurcation type could not be determined for the region in red (22.5%). Therefore, our analysis suggests that the heart transitions to alternans predominantly through smooth bifurcation.

Finally, we quantified the percentage of LV area of the heart with smooth, border-collision and undetermined bifurcations. Fig.3.4 shows the average percentage of LV area for each type of bifurcation separately for BCL$_{prior}$ (Fig.3.4(a)) and BCL$_{far}$ (Fig.3.4(b))

calculated across all our experiments. As seen from Fig.3.4, at $BCL_{prior}$, for both spatially concordant and discordant alternans, the percentage of LV area of the heart that exhibited smooth bifurcation was significantly larger in comparison to the one with border-collision and undetermined bifurcations. At $BCL_{far}$, this result was valid for the case of spatially



(a)

(b)

(c)
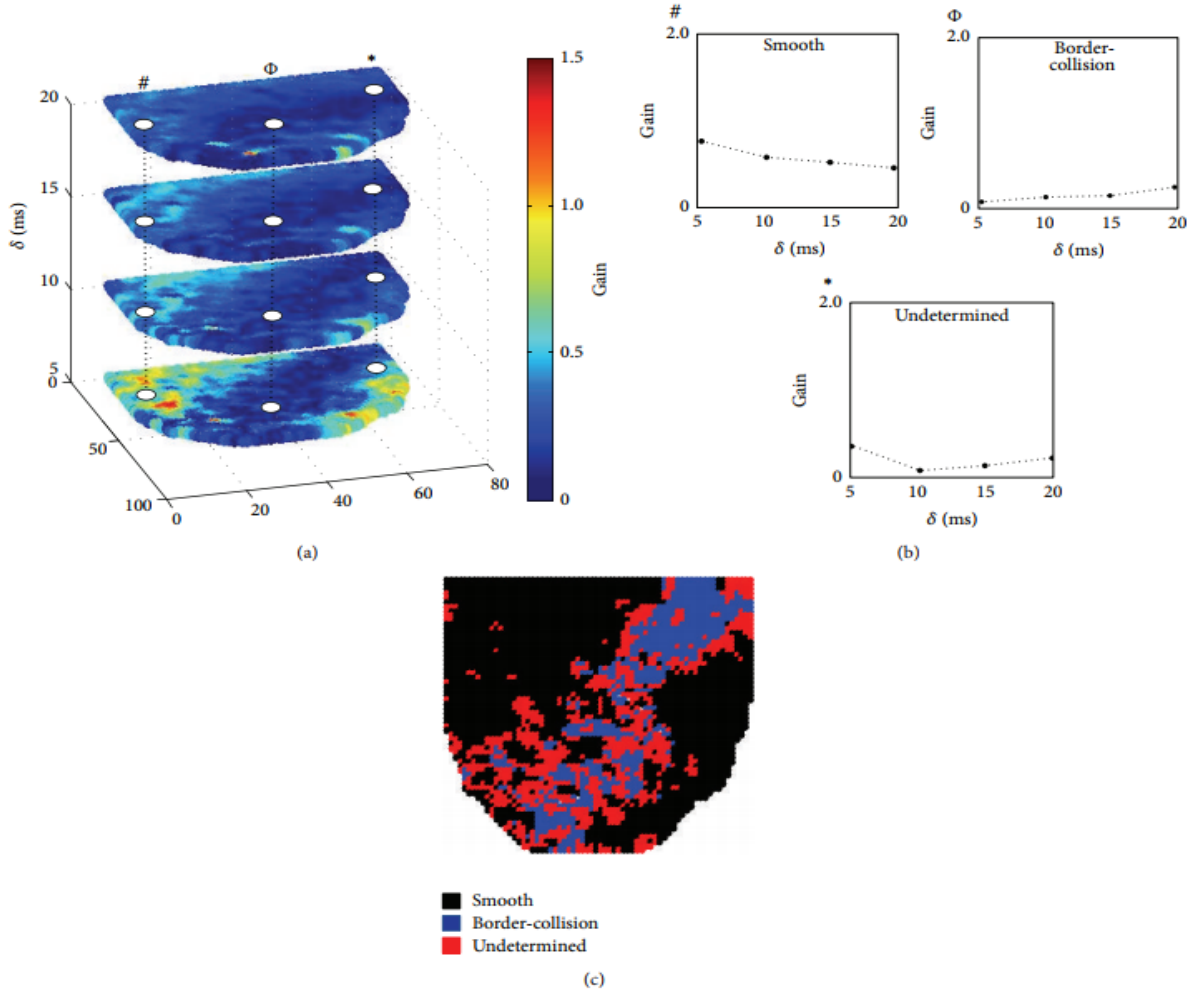
*Figure 3.3: (a) Representative 2D Gain maps as a function of $\delta$ calculated at $BCL_{prior}$ for example shown in Fig.3.2(b). (b) Single-pixel trends in Gain as a function of $\delta$ for the three representative pixels masked in panel (a). # represents smooth and $\phi$ represents border-collision bifurcation. The type of bifurcation in pixel * cannot be identified. (c) 2D bifurcation map showing the spatial distribution of different bifurcations for panel (a).*

concordant alternans but not for the spatially discordant alternans. Our results suggest that, just prior to the onset of alternans, we predominantly observe smooth bifurcation characteristics in the heart, irrespective of the spatial pattern of alternans.
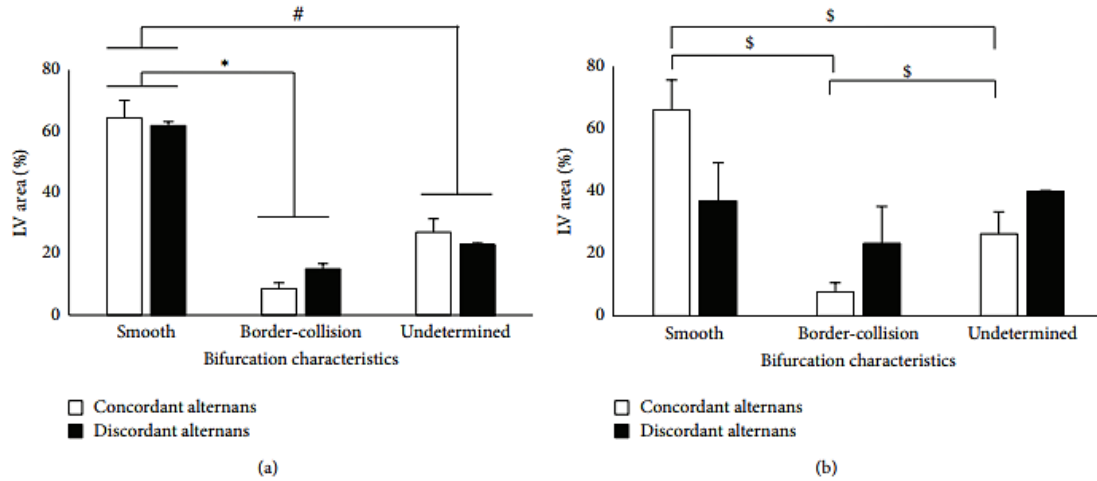


*Figure 3.4: (a) Mean bifurcation characteristics in % of LV surface in all experiments, calculated for spatially concordant and discordant alternans at (a) $BCL_{prior}$ and (b) $BCL_{far}$. \* indicates significance of $p<0.05$ between smooth and border-collision bifurcations. # indicates significance of $p<0.05$ between smooth and undetermined bifurcations. \$ indicates significance of $p<0.05$ between bifurcation types for concordant alternans.*

### 3.3.2 Spatial Correlation of Local Onset of Alternans with Bifurcation Characteristics

We also investigated the spatial correlation of the regions exhibiting alternans with the different bifurcation characteristics. First, we studied the spatial correlation between the regions of SS alternans and the bifurcation characteristics. Figs.3.5(a) and 3.5(b) show representative examples of 2D bifurcation map generated at $BCL_{prior}$ (see Fig.3.3(c)) and the SS alternans map generated at $BCL_{start}$ (see Fig.3.2(a)), respectively.

31
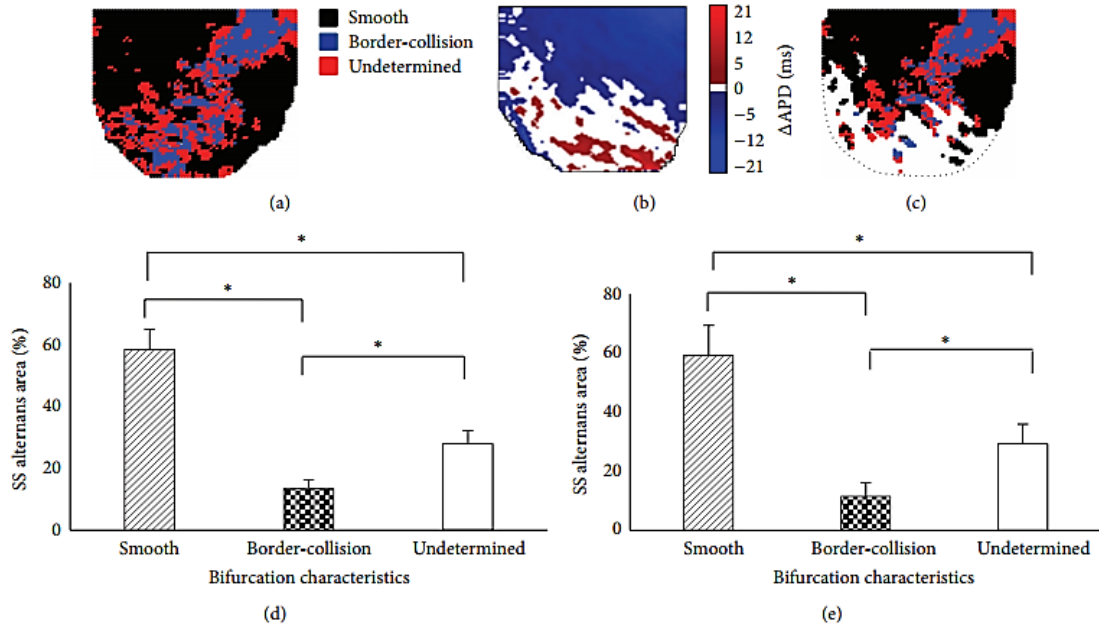
*Figure 3.5: (a) Spatial correlation of the local onset of SS alternans with bifurcation characteristics. (a) 2D bifurcation map calculated at $BCL_{prior}$ (see Fig.3.3c) (b) 2D SS alternans map calculated at $BCL_{start}$ (see Fig.3.2a). (c) Correlation between bifurcation and SS alternans maps. Average % of smooth, border-collision and undetermined bifurcations from all experiments are shown for (d) $BCL_{prior}$ and (e) $BCL_{far}$. \* indicates $p<0.05$*

The spatial superposition of these two maps is shown in Fig.3.5(c). Therefore, in Fig.3.5(c) the bifurcation characteristics (calculated at $BCL_{prior}$) are only shown for spatial regions that exhibited alternans at the next BCL (i.e., $BCL_{start}$). The white regions in Figs.3.5(b) and 3.5(c) were excluded from the analysis, since no alternans was present there at $BCL_{start}$. Figs.3.5(d) and 3.5(e) show the average percentage of LV area that developed SS alternans with the bifurcation characteristics calculated across all our experiments at $BCL_{prior}$ and $BCL_{far}$, respectively. Since the spatial pattern of alternans developed at $BCL_{start}$ did not always coincide with the spatial pattern of alternans induced by perturbation, it was

32

difficult to categorize the bifurcation characteristics in relation to spatially concordant or discordant alternans. However, as seen from the figure, the overall regions of SS alternans that coincided with smooth bifurcation characteristics were significantly higher than those coinciding with border-collision bifurcation, both at $BCL_{prior}$ and $BCL_{far}$. The data suggests that the regions of the LV that eventually develop alternans at SS show predominantly smooth bifurcation characteristics prior to the onset of alternans.
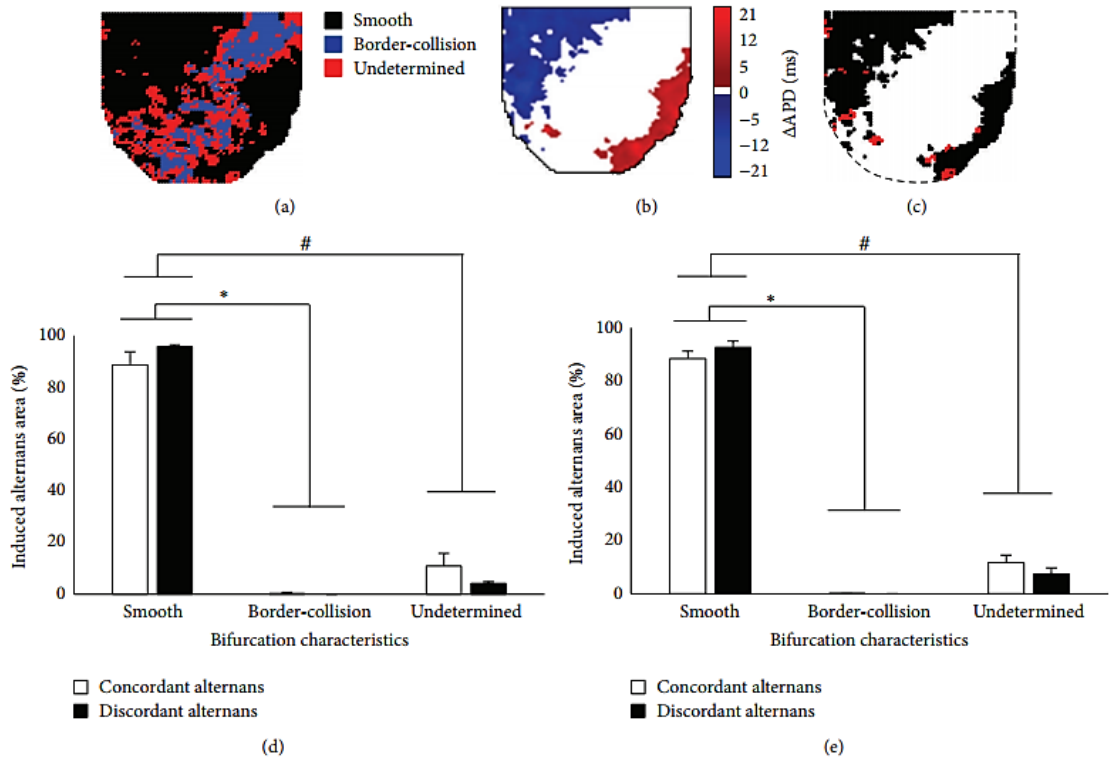


*Figure 3.6: (a) Spatial correlation of alternans induced by perturbation (at δ = 5ms) with bifurcation characteristics. (a) 2D bifurcation map calculated at $BCL_{prior}$ (see Fig.3.3c) (b) 2D alternans map at δ = 5ms calculated at $BCL_{prior}$ (see Fig.3.2b). (c) Correlation between these two maps. Average % of smooth, border-collision and undetermined bifurcations from all experiments are shown for (d) $BCL_{prior}$ and (e) $BCL_{far.}$*

33

Similar analysis was performed to investigate the spatial correlation between bifurcation characteristics and alternans induced by alternate pacing. Figs.3.6(a) and 3.6(b) show a representative example of 2D bifurcation map (see Fig.3.3(c)) and 2D alternans map at $\delta = 5$ ms (see Fig.3.2(b)), respectively. Note that both maps were calculated at $BCL_{prior}$. Fig.3.6(c) shows the spatial correlation between these two maps. Figs.3.6(d) and 3.6(e) show the average data across all experiments for $BCL_{prior}$ and $BCL_{far}$, for both spatially concordant and discordant alternans. As seen from the figure, the region of induced alternans coincided predominantly with smooth bifurcation characteristics, both at $BCL_{prior}$ and $BCL_{far}$, irrespective of the type of alternans. Note that the percentage of border-collision bifurcation is negligible. The data suggests that alternans that is induced by small perturbations is formed predominantly through smooth bifurcation.

Comparison of data across Figs.3.5 and 3.6 suggests a higher spatial correlation between smooth bifurcation characteristics and alternans induced by perturbation as opposed to SS alternans. The induced alternans showed lower border-collision and undetermined characteristics than SS alternans at both $BCL_{prior}$ and $BCL_{far}$.

## 3.4 Conclusion and Discussion

We observed that the transition from constant APD response to alternans in isolated whole rabbit hearts occurred primarily through a smooth bifurcation. There was significant spatial correlation of the region exhibiting alternans with smooth bifurcation characteristics. The correlation of smooth bifurcation with alternans induced by perturbation was significantly higher than with SS alternans. As we moved away from the onset of alternans, the percentage of the heart exhibiting smooth bifurcation characteristics

decreased as the region with undetermined bifurcation characteristics increased. The region of the heart exhibiting border-collision bifurcation characteristics was significantly smaller than both the smooth bifurcation and the undetermined bifurcation regions.

Characterizing the type of bifurcation to alternans holds promise as a possible method for the prediction of alternans prior to its onset and may shed light for the prevention of arrhythmias. In this study, we experimentally investigated the spatial dynamics of bifurcation that governs the transition to alternans in isolated whole rabbit hearts. We identified the local onset of alternans, characterized the bifurcation type prior to its onset, and studied the spatial distribution of bifurcation characteristics across the LV surface of the heart. In addition, we also investigated the spatial correlation of the regions of the LV exhibiting alternans with the type of bifurcation. To the authors' best knowledge, this is the first study to investigate the bifurcation type of alternans based on spatial dynamics and quantify the spatial correlation of alternans with the type of bifurcation exhibited.

Our main results are as follows. First, the bifurcation to alternans in the heart occurs predominantly through smooth bifurcation. Second, the region of the heart eventually exhibiting alternans shows a significantly higher spatial correlation to the region exhibiting smooth bifurcation characteristics.

Previous studies attempted to characterize the bifurcation to alternans based on theoretical models of the atrioventricular nodes [42] or microelectrode recordings from ventricular tissue samples [43]. Here, we aimed to investigate the spatial distribution of the bifurcation characteristics by performing high resolution optical mapping experiments on

35

isolated whole rabbit hearts. Although initially described as a period doubling smooth bifurcation, later studies of alternans showed the existence of border-collision bifurcation characteristics and a more complex behavior that governed the transition to alternans. Our results indicated a spatial predominance to smooth bifurcation when transitioning from constant APD response to alternans in the LV region of the heart. Although the presence of border-collision bifurcation was seen, the region of the LV exhibiting smooth bifurcation was significantly higher.

We also investigated the spatial correlation of the regions of the LV exhibiting alternans with the type of bifurcation in the case of both spatially concordant and spatially discordant alternans. As was seen from the results, there was significantly higher spatial correlation between alternans induced by perturbation with smooth bifurcation characteristics. For the purpose of this study, we only considered alternans induced by a perturbation of 5ms when investigating the spatial correlation between the induced alternans and the type of bifurcation. Since, as shown in the results, increasing the perturbation resulted in an increase in the area of the LV exhibiting alternans, a perturbation of 5 ms was a good representation of the onset of induced alternans. An interesting finding was that the regions of the LV that exhibited alternans at SS did not exactly coincide with the regions of the LV in which alternans was induced by perturbation. The phenomenon of spatial concordance or discordance of alternans also differed between SS and induced alternans. This can be attributed to the possibility that the alternate pacing protocol leads to altered dynamical activity of the heart compared to SS pacing. However, in both cases irrespective of the spatial pattern of alternans, just prior to the onset we see a significantly

36

higher spatial correlation of alternans with smooth bifurcation characteristics as compared with either the border-collision bifurcation or the undetermined bifurcation characteristics.

Our results indicated that the region of the LV exhibiting border-collision bifurcation was significantly low while a definite portion of the LV exhibited undetermined characteristics. This indicates the possibility of the presence of other bifurcation characteristics in the heart with more complex behavior. However, in comparison to smooth bifurcation, the region with undetermined characteristics was still significantly smaller just prior to the onset of alternans, which supports the result that the transition to alternans predominantly occurs through a smooth bifurcation.

# CHAPTER 4: INCORPORATING STOCHASTICITY IN PERIODIC PACING

Author Contributions:

Concept was developed by E.G.T. and K.K. Pacing protocol was implemented by K.K. Optical mapping experiments were designed and implemented by K.K and S.W.L. Data was analyzed by K.K. and S.W.L. and prepared for publication by all authors.

**Abstract**

Clinically, healthy hearts have been associated with a high ventricular HRV while diseased hearts have been known to exhibit low ventricular HRV. Hence, low HRV is suggested to be a marker of cardiac ventricular arrhythmias. Over the past few years, there has been considerable amount of interest in incorporating HRV in pacing to emulate healthy heart conditions and re-stabilize the electrical activity in diseased hearts. Recently, we used single cell numerical simulations to demonstrate that HRV incorporated into periodic pacing promotes alternans formation and thus, can be pro-arrhythmic. Here, we performed high-resolution optical mapping experiments on Langendorff perfused, healthy whole mice hearts to validate our numerical findings. Our results indeed demonstrate that HRV promoted the onset of cardiac alternans, which is believed to be a precursor of fatal cardiac rhythms. Hence, our present study suggests that incorporating HRV into periodic pacing while addressing several clinical needs may not be safe. There is a pressing need to better understand paced cardiac dynamics and develop anti-arrhythmic pacing techniques that would prevent cardiac arrhythmias.

## 4.1 Introduction

HRV is a physiologically inherent variation in time interval between two heart beats [23, 51, 52]. This variability is modulated by many physiological factors, including the influence of circadian rhythms, temperature regulations, changes in cardiac sympathetic and parasympathetic nerve activity, respiratory rhythms, etc. It is clinically well established that in a normal sinus rhythm, a high standard deviation in the HR signal correlates with

39

healthy cardiac tissue. In contrast, low HRV has been consistently reported to correlate with increased propensity of lethal cardiac arrhythmias [8-11].

Previous studies have investigated the relationship between HRV and the formation of cardiac alternans. There has been considerable curiosity to investigate the effect of incorporating HRV in pacing in order to emulate healthy heart behavior in diseased hearts. However, previous *in-silico* studies elucidating the effect of HRV in periodic pacing have shown mixed results [12, 53-56]. Dvir et al. have reported that stochastic pacing increases electrical stability and the appearance of APD alternans [53-55]. Contrary to their results, McIntyre et al. reported that increased HRV promoted the formation of cardiac alternans during periodic pacing [12].

Here, in a preliminary study, we aimed to experimentally demonstrate the effect of incorporating HRV in periodic pacing, on the formation of alternans in *ex-vivo* isolated mice hearts. Investigating the onset of alternans would provide an indication of the likelihood of the heart to transition into abnormal rhythms.

## 4.2 Methods

### 4.2.1 Optical Mapping

All experiments conformed to the Guide for the Care and Use of Laboratory Animals (NIH publication No. 85-23, revised 1996) and the University of Minnesota guidelines regulating the care and use of animals. Wild type (WT, n=2) and a mixed strain (FVB129 and C57B6) and genotype (CamKII Cre-::GIRK2FLox) background transgenic (TG, n=3) mice of either sex were used.

Mice were euthanized and hearts were quickly extracted through thoracotomy. Immediately upon removal, the hearts were immersed in cold cardioplegic solution (in mM: glucose 280, KCl 13.44, NaHCO3 12.6, and mannitol 34). The aorta was then quickly cannulated and perfused (retrograde) with warm (37±1°C) oxygenated Tyrode's solution (in mM: NaCl 130, CaCl2 1.8, KCl 4, MgCl2 1.0, NaH2PO4 1.2, NaHCO3 24, glucose 5.5, and pH 7.4). The hearts were immersed in a chamber and superfused with the same Tyrode's solution.

After 30 minutes of stabilization, voltage-sensitive dye (di- 4-ANEPPS, 5μg/mL; Molecular Probes, USA) was added to the perfusate. Two 532 nm diode continuous green lasers (SDL-532-1000 T, Shanghai Dream Lasers Tech, Shanghai, China) were used to illuminate the left ventricular (LV) surfaces of the heart. Fluorescence signals from more than 80% of total ventricular surface were captured with two 14-bit charge-coupled device (CCD) cameras (Little Joe, RedShirt Imaging, SciMeasure), that ran synchronously at 1000 frames per second with 80 x 80 pixel resolutions. Blebbistatin (10 - 15 μM) was added to the Tyrode's solution to stop heart contractions and reduce motion artifacts.

*4.2.2 Pacing Protocols*

The periodic pacing protocol is described by the following equation:

$$APD_n + DI_n = BCL_0 \tag{1}$$

where $APD_n$ is the APD generated by the $n^{th}$ stimulus, $DI_n$ is the $n^{th}$ diastolic interval (DI), and the baseline basic cycle length, $BCL_0$, is the time interval between two consecutive stimuli. When HRV is absent (0% HRV), all BCLs are the same; and HRV can be modeled by modifying the $BCL = BCL_{HRV}$ as the following:

$$BCL_{HRV} = BCL_0 + \delta(HRV) \qquad (2)$$

where $\delta(HRV)$ is a random number with a mean of zero and a standard deviation $HRV*BCL_0$, and HRV is defined as:

$$HRV = \frac{SD_{RR}}{AVG_{RR}} * 100\% \qquad (3)$$

where $SD_{RR}$ and $AVG_{RR}$ are the standard deviation and average of the RR intervals, i.e. distance between RR peaks on the mice ECG, respectively. HRV was set as 6% and 12%, based on HR and HRV information obtained during sinus rhythm from *ex-vivo* Langendorff perfused mice hearts (see Results).

Experimentally, external stimuli (5 ms) duration, twice the activation threshold) were applied to the base of the LV using a periodic pacing protocol. The pacing protocol consisted of applying 100 stimuli at each BCL. The WT mice were paced from 140 ms down to 60 ms in steps of 20 ms, while the TG mice were paced from 130 ms down to 60 ms in steps of 10 ms. Optical mapping movies corresponding to the last 10 stimuli were recorded at the end of each BCL in order to record steady state responses from the LV epicardial surfaces of the heart. Optical movies were recorded for 0% HRV, 6% HRV, and 12% HRV from each heart. The WT mice hearts did not respond to pacing at lower BCLs even at 0% HRV and hence, those BCLs were not included in the data analysis.

### 4.2.3 Data Analysis

Recorded optical mapping movies were processed offline using custom software based on PV-wave (Visual Numerics, Inc.). The background fluorescence was subtracted from each frame, and spatial (3 x 3 pixels) and temporal (5 pixels) convolution filters were used. The optical APD were measured for each pixel at 80% repolarization ($APD_{80}$), and

two-dimensional (2D) APD maps were constructed to reveal distributions of APDs on the LV epicardial surface (Fig.4.3). Mean $APD_{80}$ values were obtained at different BCLs by averaging APDs from all pixels.

Alternans was calculated as a difference in mean APDs between two consecutive beats (B1 and B2):

$$\Delta APD = |APD_{B1} - APD_{B2}| \geq 5 \text{ ms} \tag{4}$$

All APD variations smaller than the temporal threshold of alternans (5 ms) were defined as 1:1 responses. 2D $\Delta APD$ maps were constructed to reveal the distribution of alternans for the LV epicardial surfaces of the heart (Fig.4.3). The presence of alternans was denoted in red, and the presence of 1:1 behavior (absence of alternans) was denoted in black. The temporal onset of alternans, $BCL^{onset}$, was defined as the BCL at which the temporal threshold ($\geq 5ms$) of alternans is met first. Statistical comparisons between mice exhibiting alternans at 0%, 6%, and 12% HRV were performed using Fisher's exact test. Values of p $< 0.05$ were considered statistically significant.

## 4.3 Results

| Parameter | TG1 | TG2 | TG3 |
|---|---|---|---|
| $AVG_{RR}$ (ms) | 140.44 | 152.23 | 101.92 |
| $SD_{RR}$ (ms) | 13.46 | 18.92 | 12.53 |
| HR (bpm) | 427 | 394 | 589 |
| HRV (%) | 9.58 | 12.43 | 12.30 |

*Table 4.1: HRV during sinus rhythm. Average ($AVG_{RR}$) and standard deviation ($SD_{RR}$) of RR interval, with HR and HRV calculated from captured ECG during sinus rhythm for three mice.*

We first characterized the HRV of extracted Langendorff perfused whole mice hearts to approximate the range of HRV to be utilized during periodic pacing. Table 4.1 summarizes the HR and HRV information gathered from three mice. Based on the acquired data, two values of HRV were chosen: 6% and 12%.
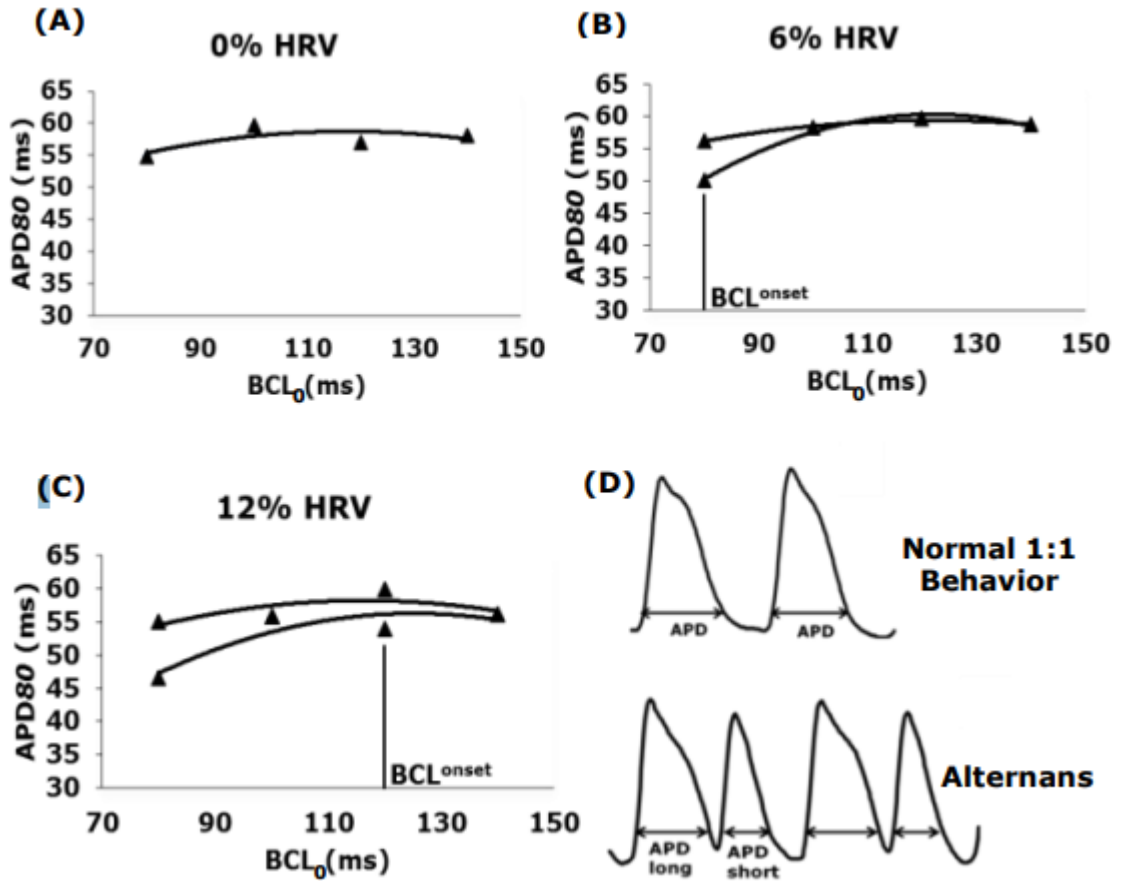


*Figure 4.1: Bifurcation diagrams showing change in APD with BCL for (A) 0%, (B) 6^ and (C) 12% HRV. BCL^onset indicates onset of alternans. (D) Illustrative examples of action potential traces showing 1:1 behaviour vs alternans.*

Fig.4.1 shows representative bifurcation diagrams depicting the change in $APD_{80}$ with decreasing $BCL_0$, for 0%, 6% and 12% HRV. As seen from Fig.4.1, HRV promoted the onset of alternans since $BCL^{onset}$ was preponed with increasing values of HRV. Fig.4.2

quantifies the number of mice that exhibited alternans for different values of HRV. Note that we combined both WT and TG mice together. Fig.4.2 demonstrates that the number of mice exhibiting alternans increased with an increase in HRV. Based on Fisher's exact test, a significantly higher number of mice exhibited alternans at 12% HRV, as compared to periodic pacing with 0% HRV.
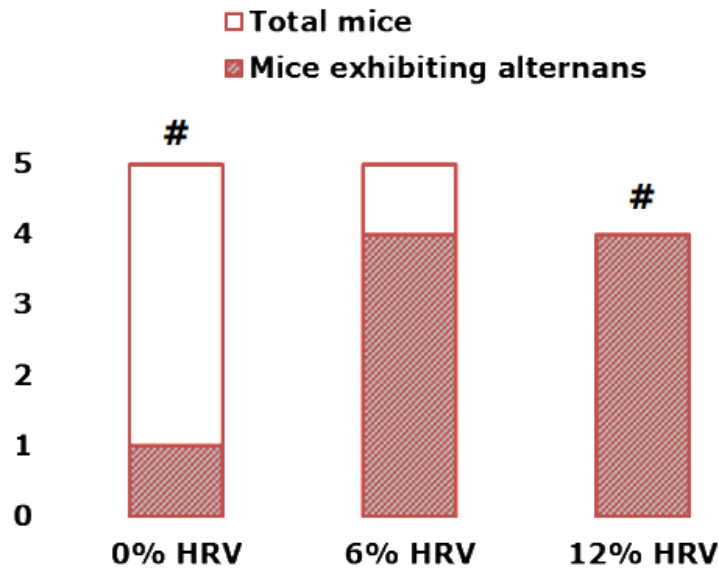


*Figure 4.2 Quantification of mice that developed alternans. # indicates statistical significance of p<0.05 between 0% and 12% HRV.*

Representative 2D APD maps for two consecutive beats, B1 and B2, along with corresponding alternans maps are shown in Fig.4.3 for different values of HRV. The $BCL^{onset}$ is highlighted with yellow squares. Fig.4.3 indicates that the temporal onset of alternans occurs earlier as HRV is increased. The individual values of $BCL^{onset}$ at different % of HRV are shown in Fig.4.4. Note that as HRV is increased, the hearts exhibited alternans earlier, thus becoming more susceptible to arrhythmias. Only one TG mouse (TG2) exhibited alternans at 0% HRV.
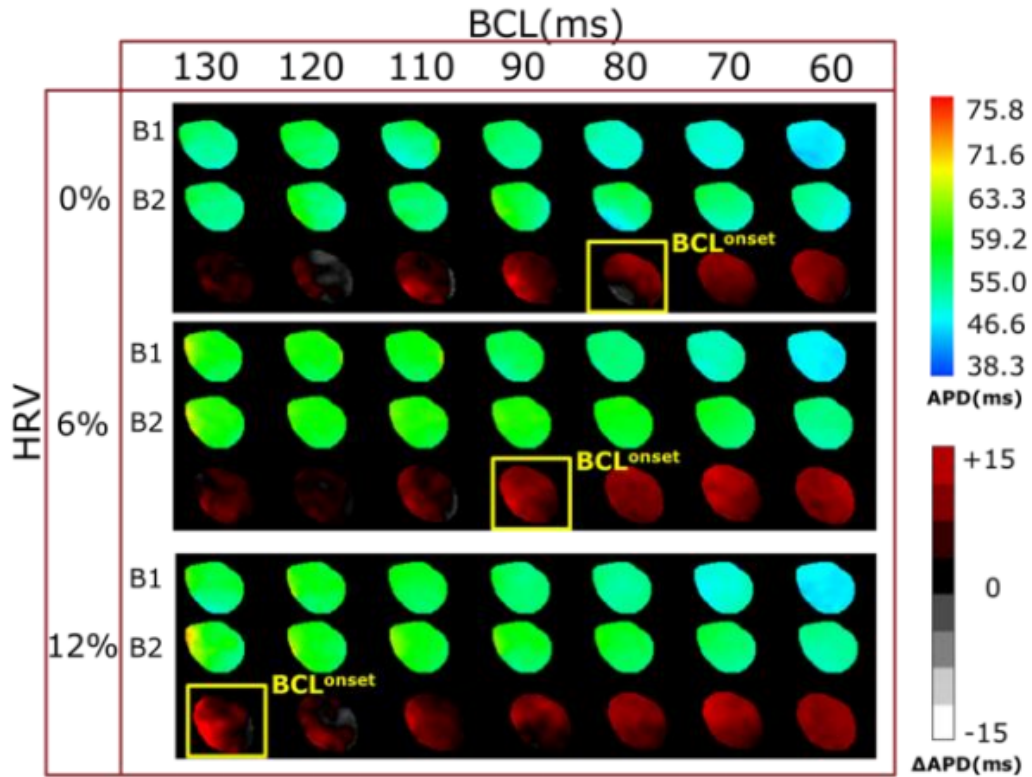
*Figure 4.3 2D APD maps showing spatial distribution of APD for two consecutive beats B1 and B2 along with alternans maps for decreasing BCL.*

## 4.5 Conclusion and Discussion

The objective of this study was to elucidate the effect of introducing HRV into periodic pacing, on the onset of cardiac alternans. We have two main results from our experiments: (1) Incorporation of HRV in periodic pacing promoted the onset of alternans, and (2) The onset of alternans preponed with increase in HRV. Therefore, our data suggest that HRV is pro-arrhythmic when combined with periodic pacing.
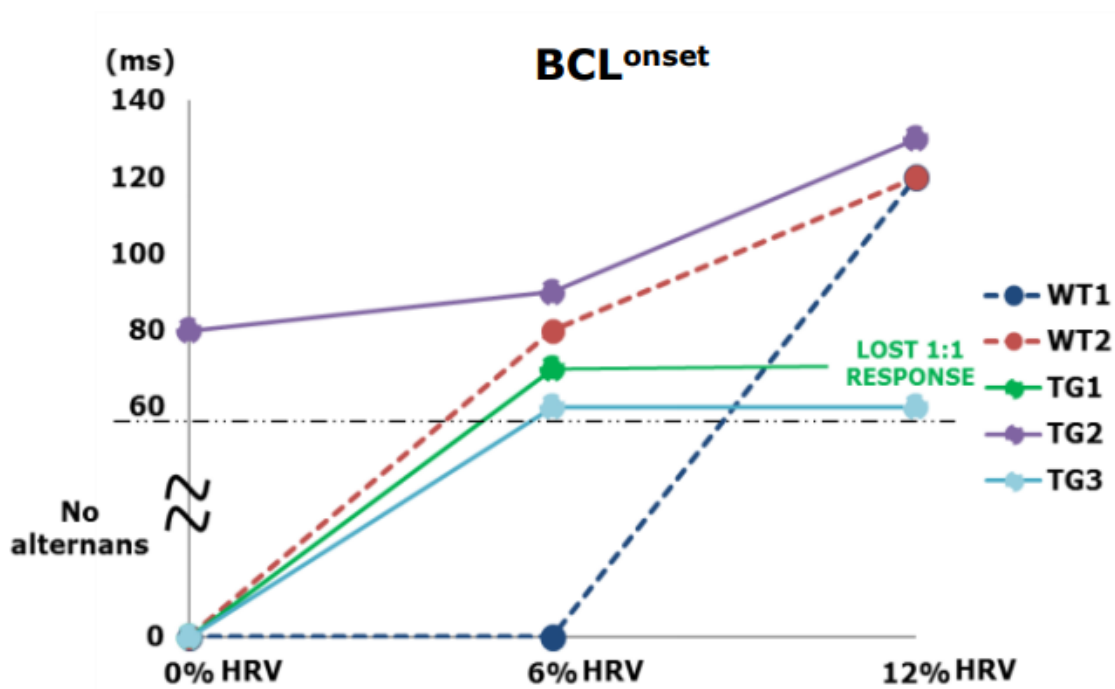
*Figure 4.4 Change in BCL$^{onset}$ with increase in HRV for each mouse*

Here, we study alternans as an indicator to investigate the proclivity of the heart to transition into unstable electrical rhythms. Although the mice model typically does not exhibit alternans under normal physiologic conditions due to the short value of APD, here we had a dual purpose of using this model. First, as we expect to see no alternans in WT mice at 0% HRV, it was interesting to investigate if increase in HRV instigated the onset of alternans. Our results support this finding, as indeed increase in HRV induced alternans in WT mice. Furthermore, Fig.4.1C highlights an interesting phenomenon. We see the temporal onset of alternans at BCL = 120 ms, while alternans do not seem to appear at BCL = 100 ms. Temporal alternans reappear at the subsequent lower BCLs. This could be due to the formation of spatially discordant alternans which are not captured in average temporal activity, thus emphasizing the spatiotemporal complexity of alternans.

Second, we also looked at transgenic mice which, due to altered ionic conditions, had the possibility of exhibiting alternans at 0% HRV. In this case, we saw that the onset of alternans was further preponed with an increase in HRV. Hence, irrespective of the underlying ionic compositions, our data suggests that incorporation of HRV in periodic pacing can have pro-arrhythmic effects.

Here, we investigated the effect of incorporating HRV in periodic pacing, wherein there is a fixed relation between APD and DI (Eq.1). Our results suggest that HRV further instigates instability in cardiac rhythm during periodic pacing, leading to the proposition that feedback elimination rather than feedback modulation might be essential in preventing cardiac alternans. A more detailed spatio-temporal assessment of the effects of feedback on the onset of alternans is presented in the next chapter.

One of the limitations of this study was that it only considered the temporal onset of alternans. We applied 100 stimuli at each BCL to reach steady state. Hence, we hypothesize that consecutive beats would be an adequate measure of average APD. However, alternans is known to be a spatial phenomenon that develops gradually across the whole heart [57]. In this preliminary study, we aimed to only investigate the temporal onset of alternans. Further investigative studies would be required to compare the spatial dynamics.

In conclusion, we experimentally investigated the effect of incorporating HRV in periodic pacing by performing high-resolution optical mapping experiments on isolated whole mice hearts. Our data suggests that irrespective of underlying ionic compositions, increased HRV shows pro-arrhythmic effects during periodic pacing. HRV in periodic pacing promotes the formation of cardiac alternans and the onset of alternans is preponed

with increase in HRV. Hence, our present study suggests that simply incorporating HRV in pacing may not be safe clinically. There is a pressing need to better understand paced cardiac dynamics and develop anti-arrhythmic pacing techniques that would prevent cardiac arrhythmias.

# CHAPTER 5: FEEDBACK ELIMINATION USING CONSTANT DIASTOLIC INTERVAL PACING

Author Contributions:

Concept was developed by E.G.T. Algorithm was implemented by R.K. and K.K. Experimental setup was designed by K.K. and experiments were performed by K.K., S.W.L. and R.K. Data was analyzed by K.K. and prepared for publication by K.K. and E.G.T.

**Abstract**

Cardiac alternans, a beat-to-beat alternation in action potential duration (APD), is a precursor to fatal arrhythmias. During periodic pacing, changes in diastolic interval (DI) depend on subsequent changes in APD, thus enhancing cardiac instabilities through 'feedback' mechanism. Recently, an anti-arrhythmic *Constant DI* pacing protocol was proposed and shown to be effective in suppressing alternans in 0D and 1D *in-silico* studies. However, experimental validation of *Constant DI* in the heart has been unsuccessful due to the spatio-temporal complexity of 2D cardiac tissue and the technical challenges in its real-time implementation. Here, we developed a novel closed loop system to detect T-waves from real-time ECG data, enabling successful implementation of *Constant DI*, and performed high-resolution optical mapping experiments on isolated whole rabbit hearts to validate its anti-arrhythmic effects. The results were compared with: (1) *Periodic* pacing (feedback inherent) and (2) pacing with heart rate variability (*HRV)* (feedback modulation) introduced by using either *Gaussian* or *Physiological* patterns. We observed that *Constant DI* significantly suppressed alternans in the heart, while maintaining APD spatial dispersion and flattening the slope of the APD restitution curve, compared to traditional *Periodic* pacing. In addition, introduction of *HRV* in pacing failed to prevent cardiac alternans, and was arrhythmogenic.

**5.1 Introduction**

Fatal arrhythmias and ventricular fibrillation (VF) which lead to sudden cardiac death are believed to be preceded by alternans. APD alternans often manifest as T-wave alternans, an alternation in the shape or duration of the T-wave, in an electrocardiogram (ECG). Previous studies have established a plausible link between alternans and ventricular arrhythmias, suggesting that elimination of alternans could lead to the prevention of VF and eventual arrhythmias in the heart [3, 5-7]. Over the past two decades, several groups have attempted the control of alternans through *in-silico, in-vitro* and *ex-vivo* experiments [6, 12, 21, 22, 28-34]. Although early studies reported positive results in single cell models and *in-vitro* preparations [29, 30], control of alternans in more spatiotemporally complex two-dimensional (2D) settings proved unsuccessful [21, 31].

This can be attribute to a major flaw in the control algorithms, i.e. the use of periodic stimulation:

$$\text{APD}_n + \text{DI}_n = \text{BCL}_n = \text{BCL} = \textit{constant} \qquad (1)$$

During periodic pacing (Eq.1), there is a partial dependence of the DI on the preceding APD ($\text{DI}_n = \text{BCL} - \text{APD}_n$), i.e. *feedback*, that can lead to subsequent destabilization of normal cardiac rhythms [15, 25]. We recently reported the drawbacks of periodic pacing using single cell and 1D cable numerical simulations [12, 22], in comparison to the beneficial anti-arrhythmic effects of feedback elimination by keeping the DI constant, i.e.

$$\text{DI}_n = \text{DI} = \text{constant} \qquad (2)$$

Controlling and maintaining a *Constant DI* on a beat-by-beat basis, eliminated feedback between DI and the preceding APD and was successful in suppressing alternans [12, 22].

However, closed loop experimental validation of beat-to-beat control of alternans has exhibited limited success, especially in 2D cardiac tissue preparations [21, 31, 33, 34]. This is primarily due to the technical challenges in precisely controlling the DI on a beat-to-beat basis in real-time.

The main goal of the current study was to develop a real-time beat-to-beat control system to successfully implement *Constant DI* pacing and demonstrate its efficacy in suppressing alternans in the whole heart. We successfully addressed the technical limitations mentioned previously and implemented a novel method to validate the anti-arrhythmic benefits of feedback elimination using *Constant DI*, in *ex-vivo* isolated whole rabbit hearts. Specifically, we implemented a closed loop algorithm to detect pseudo T-waves from real-time ECG data on a beat-by-beat basis, measure real-time APD and apply stimuli after a predefined *Constant DI*. To our knowledge, this is the first study to use whole heart 2D optical mapping for high resolution spatio-temporal assessment of feedback between DI and APD. In addition, we compared the electrophysiological and anti-arrhythmic effects of *Constant DI* pacing with different pacing protocols. Namely, the following protocols were used: (1) *Periodic* (feedback inherent), (2) *HRV* pacing (feedback modulation), introduced by using both (2.1) *Gaussian* and (2.2) *Physiological* variability patterns, and (3) *Constant DI* (feedback eliminated).

**5.2 Methods**

*5.2.1. Optical Mapping*

All experiments were performed in accordance with the guidelines of the Institutional Animal Care and Use Committee at the University of Minnesota. Optical mapping

procedures were performed as previously described [38, 57]. Briefly, New Zealand White rabbits (Bakkom Rabbitry, 1.3 – 2.0 kg, $n$=4) were injected with heparin sulfate (550 U/100 g) and anesthetized with ketamine and xylazine (35 mg/kg and 5 mg/kg, resp.). The heart was quickly excised after a thoracotomy and immersed in cold cardioplegic solution (in mM: glucose 280, KCl 13.44, NaHCO3 12.6, and mannitol 34). The aorta was quickly cannulated and retrogradely perfused with warm (37 ± 1 ◦ C) oxygenated Tyrode's solution (in mM: NaCl 130, $CaCl_2$ 1.8, KCl 4, $MgCl_2$ 1.0, $NaH_2PO_4$ 1.2, $NaHCO_3$ 24, glucose 5.5, and pH 7.4) under constant pressure. The heart was immersed in a chamber and superfused with the same Tyrode's solution. Motion uncoupler Blebbistatin (10 $\mu$M) was added to Tyrode's solution when needed to reduce motion artifacts.

A bolus of 4 mL of the voltage-sensitive dye di-4-ANEPPS (10 $\mu$M) was injected and excited with the use of a diode pumped, continuous-excitation green laser (532 nm, 1 W; Shanghai Dream Lasers Technology, Shanghai, China). Optical movies corresponding to the fluorescence signal were recorded from the epicardial surfaces of the left and right ventricles (LV and RV) by fast (1000 frames per second) 14-bit resolution, 80 × 80-pixel resolution cameras (Little Joe, RedShirt Imaging, SciMeasure) after a period of stabilization (~30 minutes). Simultaneously, continuous 3-electrode volume conducted ECG was recorded throughout the experiments.

*5.2.2. Real-time Closed Loop Control Algorithm*

Fig.5.1A shows a schematic of the setup interfacing the real-time ECG-based *Constant DI* control algorithm with high-resolution optical mapping. We utilized RT intervals on the ECG to approximate an APD, while TR interval was maintained constant to implement

*Constant DI*. However, as the correspondence between RT, TR intervals and APD, DIs respectively has been well established [12], fundamentally our method implements feedback
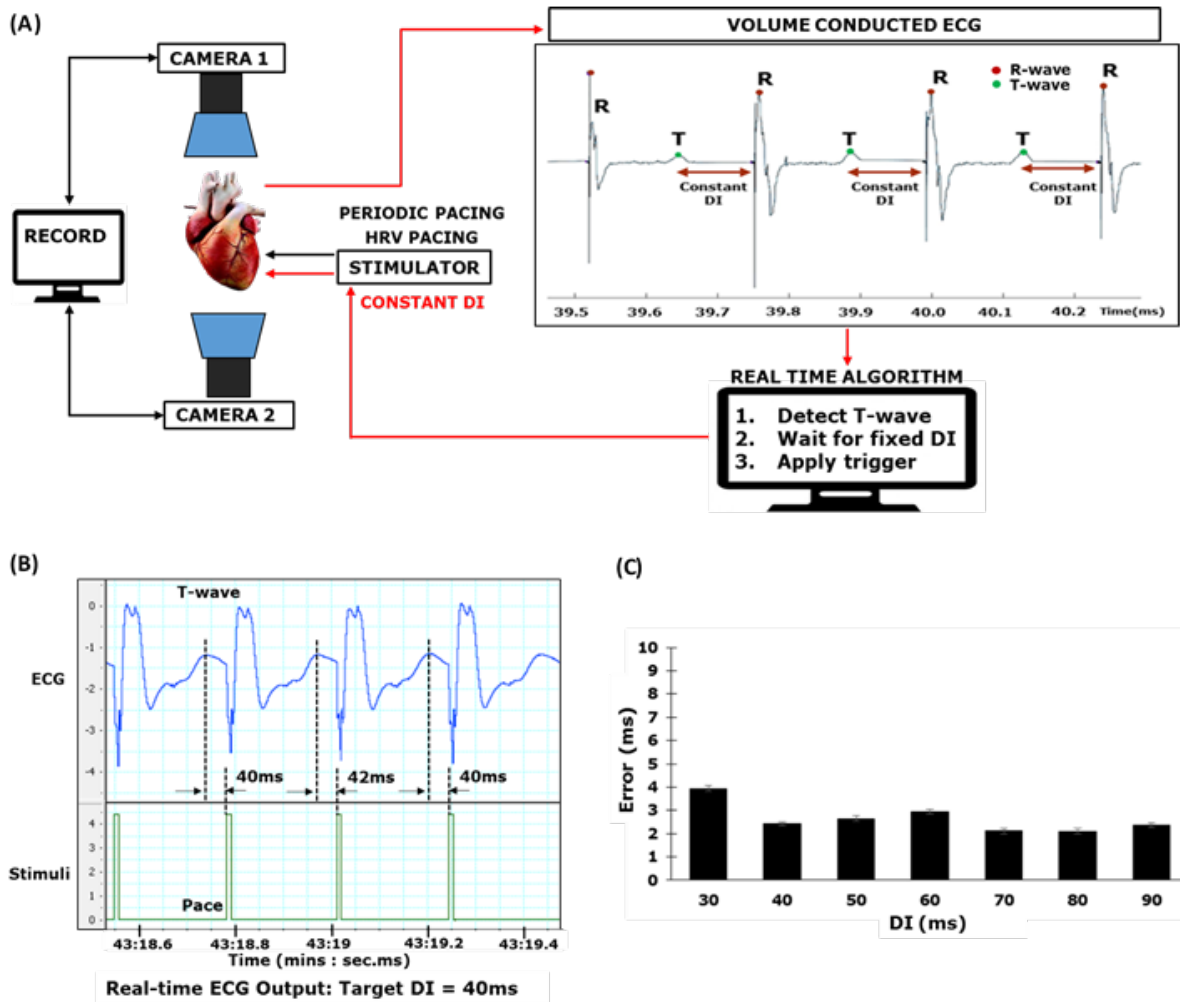


*Figure 5.1 (A) Schematic of the optical mapping system. Red arrows highlight the real-time ECG T-wave detection and Constant DI algorithm implementation. Black arrows indicate 2D optical imaging and implementation of Periodic and HRV pacing. (B) Validation of Constant DI pacing using real-time ECG recording for representative target DI of 40 ms. Black arrows mark achieved Constant DI. (C) Error at each DI, calculated as difference between achieved and expected DI, for one representative pacing run.*

elimination by controlling the repolarization interval. Arrows in black indicate the original optical mapping set up that was used for the *Periodic* and *HRV* pacing implementation. Arrows in red indicate the closed loop system that enables real-time T-wave detection from pseudo-ECG and implementation of *Constant DI* pacing. *Constant DI* pacing was implemented using a proprietary algorithm developed in LabVIEW that detected the ECG T-wave peak and applied a pacing stimulus after a predefined fixed duration equivalent to the required DI.

*5.2.3. Pacing Protocols*

The following pacing protocols were implemented:

(1) *Periodic* pacing protocol. Since *Periodic* pacing (Eq.1) enforces the BCL to be constant during each beat, it creates an inherent dependency of the DI on the preceding APD, i.e. feedback. Hence, in this study, we refer to *Periodic* pacing protocol as *'feedback inherent'* protocol.

(2) *HRV* pacing protocol. Under normal physiological conditions, intrinsic HRV, a variation in time interval between two consecutive heartbeats, ensures deviation of the heart from periodic pacing [23, 52]. To simulate known healthy human HRV and to in turn modulate the feedback between DI and APD, we incorporated stochasticity in pacing by varying the BCLs. Two different *HRV* pacing protocols were used to generate *'feedback modulation'*:

(2.1) *Gaussian* pacing. Here, we incorporated HRV in pacing by using a strictly Gaussian distribution of beat-to-beat intervals. *Gaussian* pacing was implemented as follows:

$$BCL_n = BCL_0 \pm \delta(HRV) \qquad (3)$$

where $\delta(HRV)$ is a random number with a mean of zero and standard deviation of $BCL_0*HRV$, and,

$$HRV = \frac{STD_{RR}}{AVG_{RR}} * 100\ \% \qquad (4)$$

where $STD_{RR}$ and $AVG_{RR}$ standard deviation and average of the RR intervals i.e. the distance between the RR peaks in the ECG. To mimic known human HRV values [12, 58] we used a Gaussian distribution with HRV set at 5%.

(2.2) _Physiological_ pacing. Here, to mimic a physiological HRV pattern, we utilized the variation in RR intervals from a previously acquired anesthetized _in-vivo_ rat ECG recording. The original HRV of 1.12% was scaled up to 5% to simulate a quasi-physiologically relevant human HRV value, and the scaled RR 'pattern' was superimposed onto BCL values to implement _Physiological_ pacing for each BCL from 200 ms down to 120 ms in steps of 10 ms.

(3) _Constant DI_ pacing protocol. To evaluate the proposed anti-arrhythmic effects of '_feedback elimination_', we implemented _Constant DI_ pacing as shown in Eq.2

External stimuli at twice the activation threshold, were applied at the base of the LV for each rabbit, during each pacing protocol. 100 stimuli were applied at each BCL for _Periodic_ and _HRV_ pacing, and the BCL was progressively decreased from 200 ms down to 120 ms in steps of 10 ms. Similarly during _Constant DI_, 100 stimuli were applied at each DI and the DI was progressively decreased from 100 ms down to 30 ms in steps of 10 ms.

A total of n = 26 (9, 6, 5, 6) pacing runs were analyzed for the LV, while n = 20 (6, 5, 5, 4) runs were analyzed for the RV, for the _Periodic, Gaussian, Physiological_ and

57

*Constant DI* pacing protocols respectively. Runs of each pacing protocol were acquired in each rabbit in a random manner, to eliminate any effect of pacing order on the results. Optical movies corresponding to the last ten stimuli were recorded for each BCL (DI) for all pacing protocols.

*5.2.4. Data Analysis*

1. APD Alternans: Optical movies were recorded from the epicardial surfaces of both the LV and RV. Mean APD at 80% repolarization ($<APD_{80}>$) was calculated for RV and LV for the even ($APD_{EVEN}$) and odd ($APD_{ODD}$) beats separately. 2D mean $APD_{EVEN}$ and $APD_{ODD}$ maps were generated for each BCL and DI. Temporal threshold for alternans was set at $|APD_{EVEN} - APD_{ODD}| \leq 4$ ms and 2D alternans maps were generated as a difference of mean $APD_{EVEN}$ and $APD_{ODD}$ maps. For spatial onset of alternans, the BCL (or DI) at which at least 20% of the area of the RV or LV was occupied by alternans was defined as the $BCL_{onset}$ (or $DI_{onset}$). The presence of spatial alternans was then quantified for all the pacing runs.

2. APD Heterogeneity: To assess the dispersion of $APD_{80}$ repolarization across the LV and RV surfaces, we calculated $APD_{80}$ heterogeneity index $\mu$ as follows:

$$\mu = (APD^{95} - APD^{5}) / APD^{50} \qquad (5)$$

wherein, $APD^{95}$ and $APD^{5}$ represent the 95th and 5th percentiles of the $APD_{80}$ distribution, respectively, and $APD^{50}$ is the median $APD_{80}$ distribution. For each BCL and DI, heterogeneity $\mu$ was calculated based on 2D APD maps generated for an average $APD_{80}$ of 3-5 beats.

3. Comparison between BCL and DI: In order to compare data between the different pacing protocols, corresponding DI for each BCL was calculated for each *Periodic* and *HRV* pacing run as follows:

$$DI = BCL - <APD_{80}> \qquad (6)$$

wherein, for $|APD_{EVEN} - APD_{ODD}| \leq 4$ ms, the larger of the two APD values was used as $<APD_{80}>$, while for BCLs where $|APD_{EVEN} - APD_{ODD}| > 4$ ms, $<APD_{80}> = <(APD_{EVEN}, APD_{ODD})>$. Finally, mean DI values corresponding to each BCL were calculated for the *Periodic* and *HRV* pacing protocols by combining DI values for individual runs.

4. Slopes of APD Restitution Curve ($S_{max}$): To evaluate the effect of the different pacing protocols on the slope of APD restitution curve and in turn the propensity to arrhythmias, we calculated the minimum DI ($DI_{min}$) for each pacing run (DI corresponding to the last BCL for each run). APD restitution curves were generated as a function of change in $<APD_{80}>$ with DI and fit with a $2^{nd}$ degree polynomial. The maximum slope of restitution, $S_{max}$, was calculated for each run by evaluating the derivative of the polynomial fit at $DI_{min}$. Finally the individual mean $S_{max}$ values, corresponding to change in 2D $<APD_{80}>$ with DI, for each pacing run were combined to generate average $S_{max}$ values for each pacing protocol.

*5.2.5. Statistics*

All data are presented as mean ± standard error. Statistical comparisons between the pacing protocols were performed using 1-way ANOVA (Origin Software, Northampton, MA, USA). Fisher's exact test was used to perform statistical comparison of the number of runs

that exhibited arrhythmias across the different pacing protocols. Values of $P < 0.05$ were considered statistically significant.

## 5.3 Results

### 1. Real-time T-wave measurements

We first validated accurate T-wave detection by the real-time algorithm and execution of *Constant DI* pacing. The time instances of each T-wave peak detected and pacing stimulus applied was outputted by the algorithm for each run. Fig.5.1B shows representative real-time ECG data collected during a *Constant DI* run. Two checks performed to demonstrate the successful implementation of *Constant DI* pacing. First, the difference between expected and achieved DI, i.e. algorithm error, was calculated and was $< 8$ ms across all experimental runs. Fig.5.1C displays the algorithm error quantified for all beats at each DI, for one representative *Constant DI* run. Second, for each DI, the ECG data acquired was also analyzed post experiment and the T-wave peak detected by the algorithm was compared to the visible T-wave peak on the ECG to ensure accurate detection (Fig.5.1B). Any run that incorrectly detected a T-wave or missed the expected DI by more than 10 ms was excluded from further analysis.

### 2. Presence and onset of alternans

We quantified the number of pacing runs that exhibited alternans in the heart for each pacing protocol and the corresponding $BCL_{onset}$. As seen in Fig.5.2A, *Constant DI* pacing significantly reduced the instances of cardiac alternans in the heart (only 1 run demonstrated the presence of alternans for DI = 40ms in the RV), compared to the other three pacing protocols. *Periodic* and *HRV* pacing always induced alternans along with

instances of VF during *Gaussian* and *Physiological* pacing. Furthermore, comparing $BCL_{onset}$ between the *Periodic* and *HRV* pacing techniques (Fig.5.2B), we observed that onset of alternans is promoted with an increase in stochasticity in pacing i.e. *Physiological* pacing showed the largest $BCL_{onset}$ (194 ± 2.67 ms), while *Periodic* pacing showed the smallest (137 ± 4.52 ms, p<0.05).
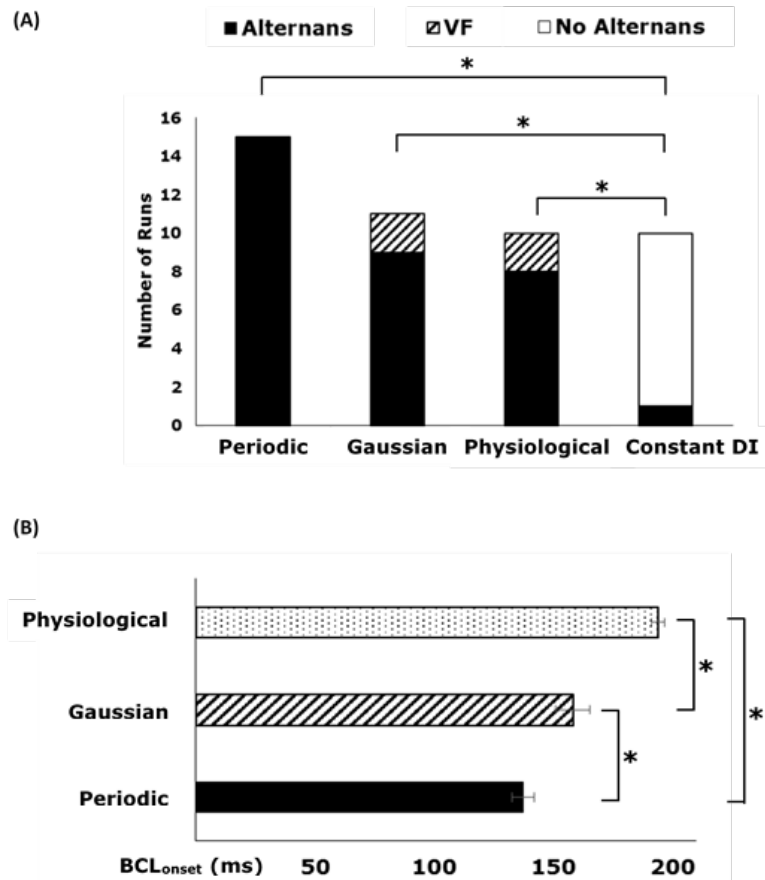


*Figure 5.2 (A) Quantification of the number of runs that exhibited alternans for each pacing technique, for both the LV and RV combined. Threshold for spatial onset of alternans = 20% area of LV or RV, temporal threshold = 4ms. (B) Comparison of BCLonset between Periodic, Gaussian and Physiological pacing. * denotes statistical significance of p < 0.05*

3. *Spatio-temporal evolution of alternans*

Next, we quantified the spatial evolution of alternans for the different pacing protocols as a percentage of RV or LV, for decreasing values of DI. Since *Physiological* pacing
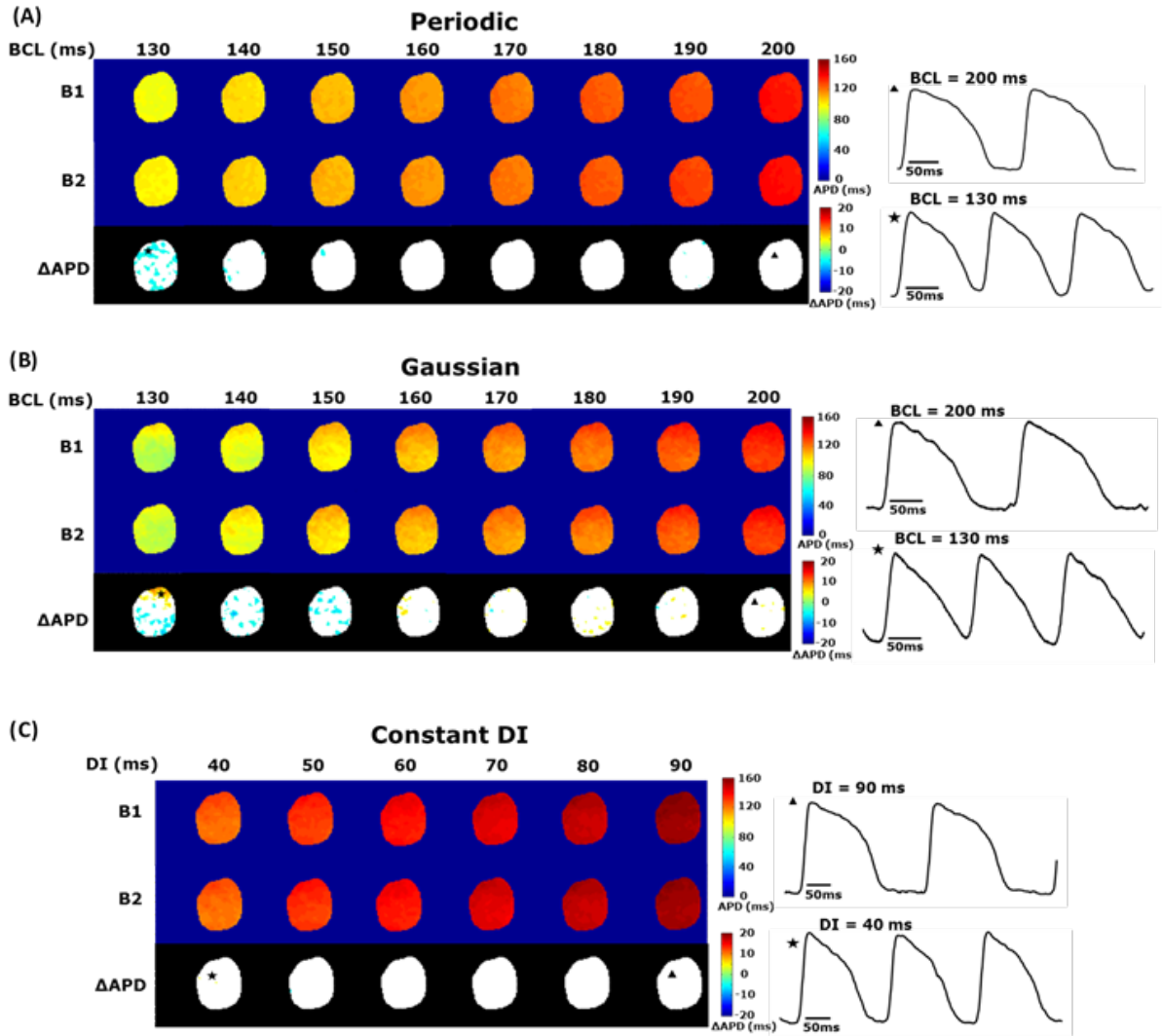


*Figure 5.3 Representative 2D APD maps for APD$_{EVEN}$ (B1), APD$_{ODD}$ (B2) and ΔAPD (alternans), for (A) Periodic, (B) Gaussian and (C) Constant DI pacing, from the LV. Action potential traces depicting alternans (\*) at lower BCL and no alternans (Δ) at higher BCL are shown for Periodic and Gaussian pacing. Note that no alternans were observed for Constant DI pacing and representative action potential traces at two distinct DIs are denoted by \* and Δ.*

significantly preponed $BCL_{onset}$ compared to both *Gaussian* and *Periodic* pacing, we only show data comparing *Periodic*, *Gaussian* and *Constant DI* from here on. Fig.5.3 shows representative 2D $APD_{EVEN}$ and $APD_{ODD}$ maps along with 2D alternans maps for decreasing BCLs and DIs, for *Periodic*, *Gaussian* and *Constant DI* pacing. For both *Periodic* and *Gaussian* pacing, we observed an increase in the area of the heart occupied by alternans as we decreased the BCL (shown in terms of calculated corresponding DIs),
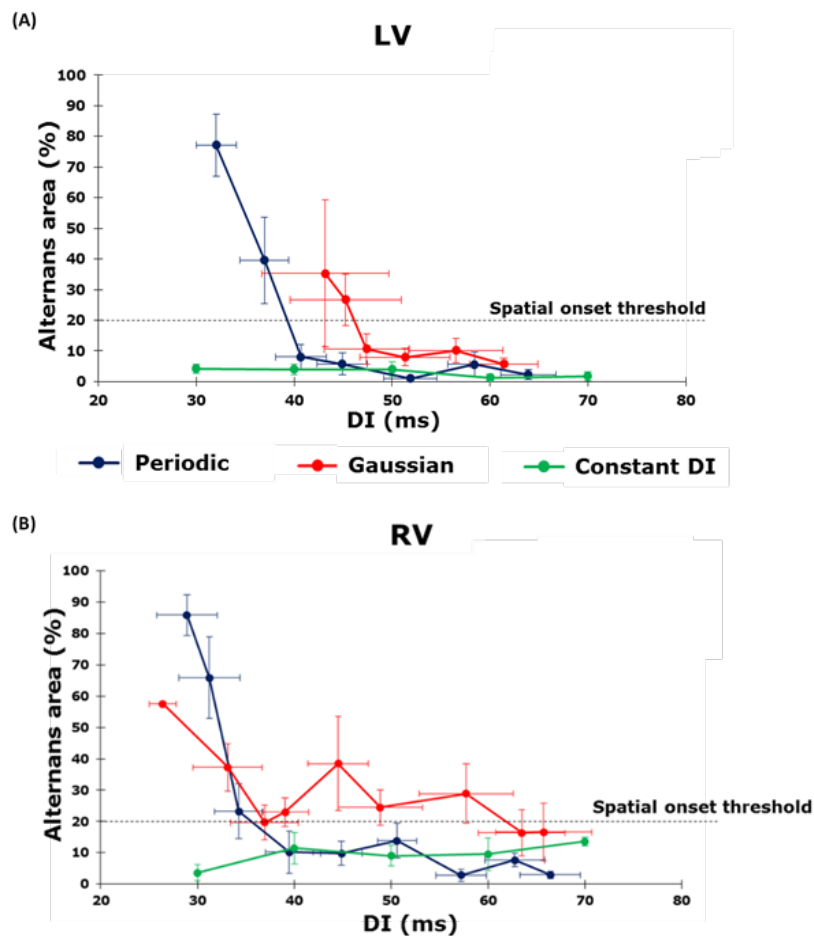


*Figure 5.4 Demonstrating the spatial evolution of alternans across the (A) LV and (B) RV with decreasing DIs, for Periodic (blue), Gaussian (red) and Constant DI (green) pacing techniques. Dotted black line indicates spatial threshold of 20% used to define BCL$_{onset}$.*

63

as demonstrated in Fig.5.4. Note that *Constant DI* pacing prevented the spatio-temporal evolution of alternans in both LV and RV.
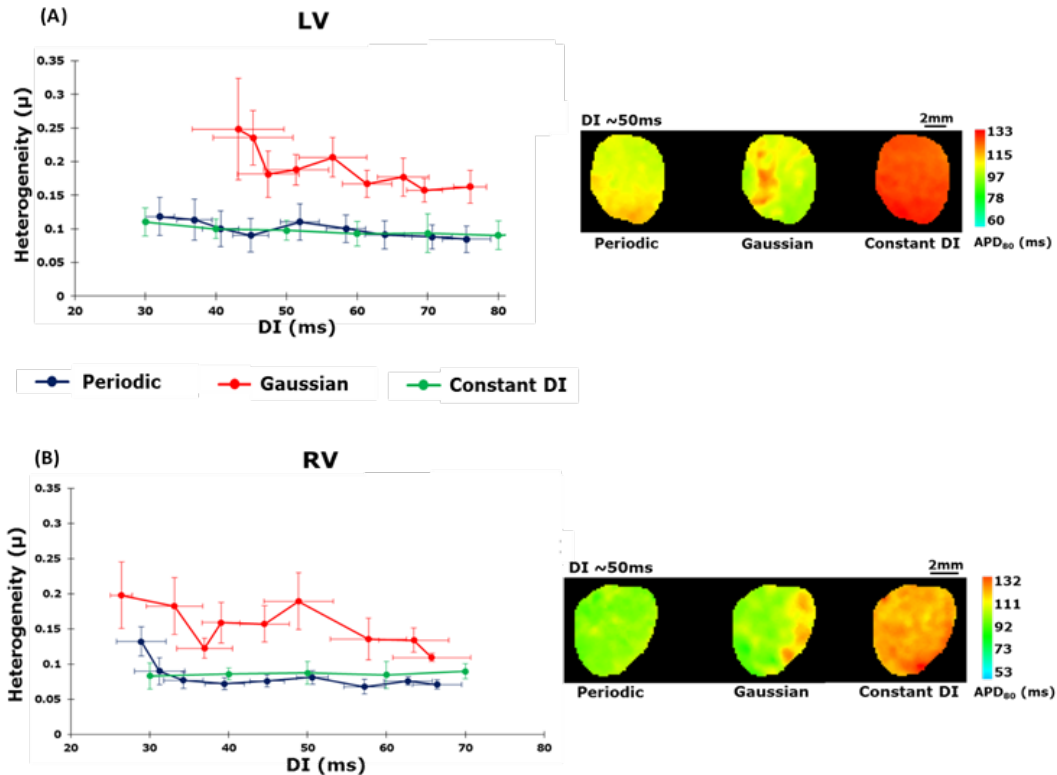


*Figure 5.5 Change in heterogeneity μ with decreasing DIs for Periodic (blue), Gaussian (red) and Constant DI (green) pacing, for both (A) LV and (B) RV. Representative 2D APD maps alongside for each pacing technique, demonstrating the distribution of $APD_{80}$ across the ventricles for a calculated DI of ~ 50ms.*

4.   APD Heterogeneity μ

Fig.5.5 demonstrates the change in APD heterogeneity μ with a decrease in DIs for the three pacing protocols, along with representative 2D APD maps. We observed increased μ, suggesting a greater dispersion of APD repolarization, in the case of *Gaussian* pacing, compared to *Periodic* and *Constant DI* pacing, for both the LV and RV. The 2D APD maps shown for a DI of ~ 50ms demonstrated the increased heterogeneity induced by *Gaussian*

pacing. Comparatively, both *Periodic* and *Constant DI* showed relatively homogenous APD distributions for both the LV and RV.

>   5.  *APD Restitution Curve*

Fig.5.6 shows $APD_{80}$ as a function of different DIs for *Periodic*, *Gaussian* and *Constant DI* protocols. As seen from the figure, at higher DIs we observed slightly larger $APD_{80}$ during *Constant DI* pacing. In case of the LV for instance, at DI = 60ms, $APD_{80}$= 127.30 ± 5.5ms  (equivalent BCL = ~190ms). In comparison, for BCL = 190ms, $APD_{80}$= 119.39 ± 2.8ms for *Periodic* pacing and $APD_{80}$= 120.48 ± 2.5ms for *Gaussian* pacing, which was not significantly different. However, *Constant DI* pacing significantly lowered $S_{max}$ in comparison to other pacing protocols, in both the LV and RV. It is important to note that both *Periodic* and *Gaussian* pacing had $S_{max}$ >1 for both LV and RV, while $S_{max}$ <1 during *Constant DI* pacing, demonstrating its anti-arrhythmic effect. In addition, the calculated $DI_{min}$ for the *Gaussian* pacing was significantly larger compared to both *Periodic* and *Constant DI* pacing for the LV (Fig.5.6 bottom panel).

**5.4 Discussion**

>   Here, we extended our previous *in-silico* findings of the anti-arrhythmic benefits of *Constant DI* [12, 22] pacing to the whole heart level and implemented a novel real-time closed loop system for beat-by-beat cardiac control. Using our system, we investigated the effect of feedback on the propensity to cardiac alternans, using three different pacing protocols: *Periodic* (feedback inherent), *HRV* (feedback modulation) and *Constant DI* (feedback elimination). Our major findings are as follows: First, we successfully implemented an algorithm for real-time detection of T-waves and validated its efficacy in controlling the
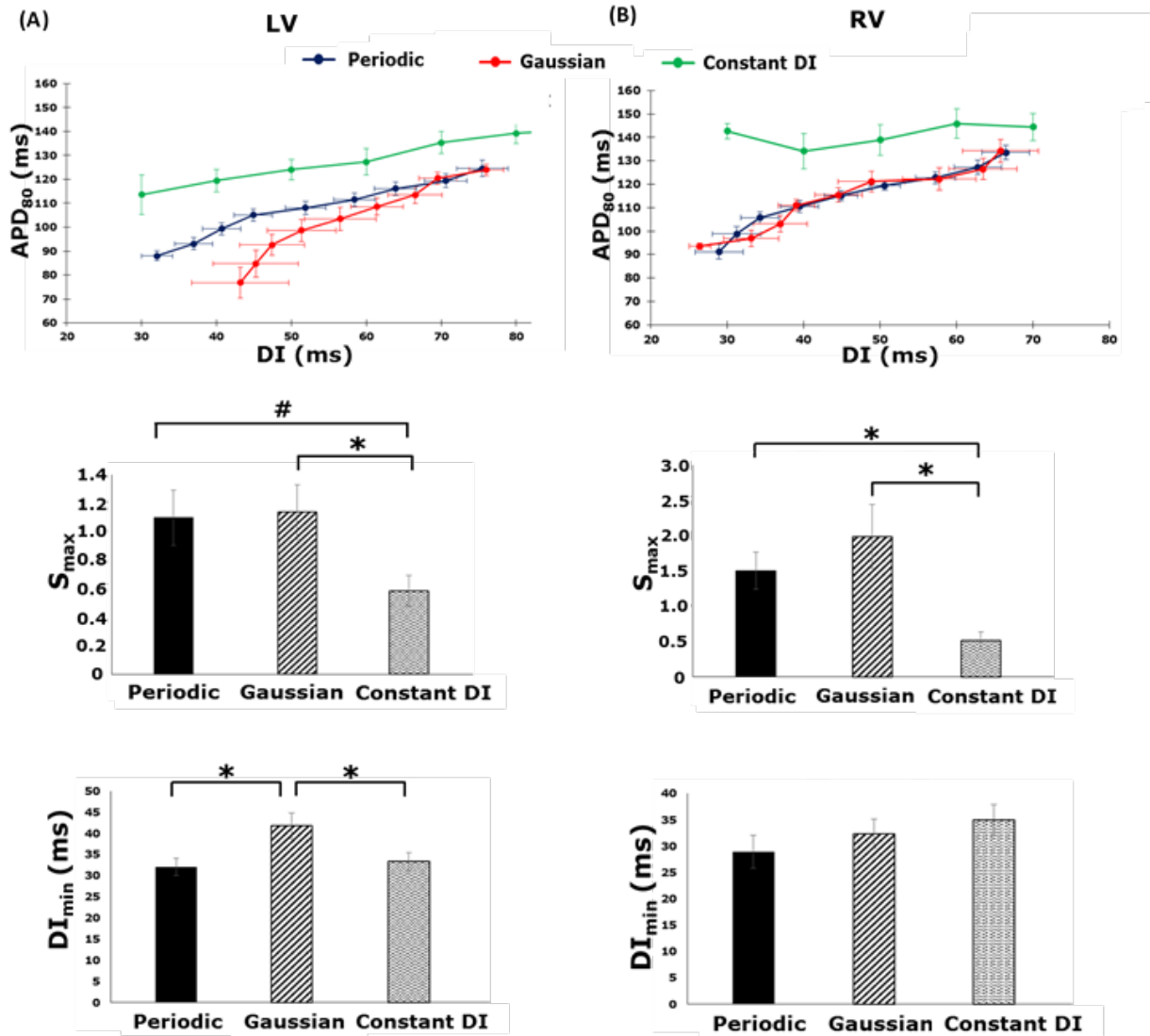
*Figure 5.6 Data shown for (A) LV (left panel) and (B) RV (right panel). Top: Restitution curves demonstrating change in mean APD$_{80}$ with decreasing DIs for Periodic (blue), Gaussian (red) and Constant DI (green) pacing. Mid: Mean restitution slopes S$_{max}$ calculated at DI$_{min}$. Bottom: Mean DI$_{min}$ across all runs. * denotes statistical significance of p < 0.05 and # denotes statistical significance of p < 0.07.*

DI on a beat-to-beat basis in the heart. Second, *Constant DI* pacing prevented the occurrence of alternans in the heart, thus providing a clear anti-arrhythmic effect. *Constant*

*DI* pacing was associated with an increase in APD and decrease in $S_{max}$, while not affecting spatial heterogeneity of APD, μ, in comparison to *Periodic* pacing.

On the other hand, feedback modulation using *HRV* pacing, which was modeled with either *Gaussian* or *in-vivo Physiological* patterns, promoted the formation of alternans and VF in the heart, thus enhancing arrhythmogenecity. *HRV* pacing was associated with both increased $S_{max}$ and μ, and earlier occurrence of alternans (larger $BCL_{onset}$), in comparison to *Periodic* pacing, thus providing clear pro-arrhythmic effects.

Our results support our hypothesis that the presence of feedback, or dependence of the DI on the preceding APD, can lead to electrical instability and cardiac arrhythmias, especially at higher pacing rates. This was demonstrated by the onset of spatio-temporal cardiac alternans during all *Periodic* pacing runs. Feedback modulation or *HRV* further perturbed the stability of the system and promoted arrhythmogenesis. To incorporate *HRV* in pacing, we used two methods. *Gaussian* distribution with 5% HRV was used to introduce perturbations in BCL, based on previously shown human HRV values and distributions [15, 19]. Furthermore, to investigate a truly 'random' yet physiological perturbation, we also implemented quasi-*Physiological* pacing by utilizing RR interval patterns from previously recorded *in-vivo* rat ECG traces. However, our results demonstrated an increase in arrhythmogenecity during *HRV* pacing, with *Physiological* pacing showing earlier onset of alternans than *Gaussian* pacing. This can be attributed to the fact that incorporating HRV in pacing only modulates feedback and does not eliminate the dependence of the DI on prior perturbations. *Constant DI* pacing however, ensures that

the DI during each beat is independent of any prior instabilities or perturbations in the APD and hence, is more electrically stable.

*HRV* pacing also showed an increase in APD heterogeneity compared to both *Periodic* and *Constant DI* pacing. Since the beat-to-beat intervals are varied randomly when incorporating HRV in pacing, it is possible that APD repolarization is heterogeneously affected. While certain regions might fully repolarize, other regions might be forced to reactivate before complete repolarization, which eventually could lead to heterogeneity in APD distribution across the surface of the heart. This could lead to abnormal activations such as early after depolarizations (EADs) and delayed after depolarizations (DADs), which are known to be arrhythmogenic. This is supported by our data wherein we see earlier onset of alternans, instances of VF and an earlier loss of pacing response (conduction block) during *HRV* pacing, demonstrated by a significantly larger $DI_{min}$ in case of the LV.

*Constant DI* pacing also demonstrated a flattening in the slope of restitution. Numerous studies have suggested the anti-arrhythmic effects of flattening the restitution slope [7, 29, 59]. Expectedly, our data showed significantly steeper restitution curves during *Periodic* and *HRV* pacing, wherein we see an onset of alternans. Since *Constant DI* pacing aims to maintain a fixed DI during each heartbeat, we see an almost linear decrease in APD as we shorten our target DI, again demonstrating the beneficial effects of feedback elimination. Overall, our data shows promising anti-arrhythmic effects of feedback elimination and beat-to-beat DI control. Furthermore, all of our findings were consistent

between the LV and RV and we did not observe any significant differences in terms of the anti-arrhythmic benefits of *Constant DI* pacing, between the two ventricles.

Note that there are two main limitations of the study. First, we utilized volume conducted 3-electrode ECG that was easy to integrate with existing 2D *ex-vivo* optical mapping system, to implement *Constant DI* pacing. Hence, our study is limited by the temporal resolution achieved by volume conducted ECG and observing a distinct T-wave. Given the rabbit model and *ex-vivo* setup, at very high pacing rates, the T-wave cannot be discerned, making it difficult to precisely detect the DI. However, feedback elimination can still be achieved by detecting a pseudo T-wave (post R-peak) and incorporating a time offset in the target DI. Hence, the minimum DI successfully implemented was 30 ms for our study. Second, we used healthy rabbit hearts for our study and hence, the size of the hearts limits the spatial validation of the pacing techniques. Further pre-clinical validation would be required to explore the benefits of *Constant DI* pacing in a large animal model, as well as under diseased conditions. However, since rabbits are known to have electrical and ionic characteristics similar to humans, we do not expect a change in model to significantly alter the concepts established in this study.

In conclusion, we developed a novel real-time closed loop system to successfully validate the efficacy of *Constant DI* pacing in suppressing alternans using isolated whole hearts, hence demonstrating its potential in the prevention and control of cardiac arrhythmias. While the presence of feedback between the DI and APD, as demonstrated by use of *Periodic* pacing, induced cardiac alternans at higher pacing rates, incorporating *HRV* in pacing further enhanced the electrical instabilities and promoted the onset of alternans.

69

In addition, irrespective of the model used to incorporate *HRV* in pacing i.e. *Gaussian* or *Physiological* pattern, incorporating stochasticity in pacing showed pro-arrhythmic effects. Hence, our data suggests that feedback elimination using *Constant DI* might be essential in the prevention of restitution dependent cardiac alternans.

## 5.5 Acknowledgements

# CHAPTER 6: EFFECTS OF MODULATING THE $M_2R$-Girk4-RGS6 PATHWAY

(The work in this chapter is under preparation for submission as Kanchan Kulkarni, Xueyi Xie, Ezequiel Marron Fernandez de Velasco, Allison Anderson, Kirill Martemyanov, Kevin Wickman and Elena G. Tolkacheva, "Investigating the electrophysiological effects of modulating the M2R-Girk4-RGS6 dependent parasympathetic pathway in isolated whole murine hearts")

Author Contributions:

Concept was developed by K.W., X.X., K.K. and E.G.T. Experiments were implemented by K.K., X.X., E.M.F. and A.A. Data was analyzed by K.K. and prepared for publication by K.K., A.A., K.W. and E.G.T.

**Abstract**

*Introduction:* A number of cardiac diseases have been linked to an imbalance in cardiac autonomic regulation and recently, there is rising interest in understanding the effect of parasympathetic modulation on cardiac dynamics. The main objective of our study is to investigate the role of the $M_2$R-GIRK4-RGS6 parasympathetic pathway in ventricular electrophysiology, using isolated whole heart optical mapping of loss-of and gain-of parasympathetic function murine models.

*Methods and Results:* We performed *in-vivo* ECG measurements and *ex-vivo* optical mapping experiments on wild-type (WT), Girk4 knockout (*Girk4$^{-/-}$*) and RGS6 knockout (*Rgs6$^{-/-}$*) mice. The effect of muscarinic agonist carbachol (CCh), which mimics parasympathetic activation, was studied in all three genotypes. Our data suggests that an imbalance in parasympathetic function affects both cardiac structural and electrophysiological properties. We observed a prolongation in $APD_{80}$ at baseline in both *Girk4$^{-/-}$* and *Rgs6$^{-/-}$*. The *Rgs6$^{-/-}$* mice showed an enlargement in heart size and severe bradycardia post CCh injection. The CCh led to an increase in $APD_{80}$ in WT, had a reduced effect in *Girk4$^{-/-}$*, and an enhanced effect in *Rgs6$^{-/-}$* mice. There was no significant effect of either Girk4 or RGS6 knock out on conduction velocity and APD heterogeneity.

*Conclusions:* The muscarinic receptor mediated GIRK channel plays an important role in modulating ventricular electrophysiology. While *Rgs6$^{-/-}$* enhanced parasympathetic function, *Girk4$^{-/-}$* led to a loss-of parasympathetic function. *Rgs6$^{-/-}$* made the heart more prone to arrhythmias, prolonged ventricular $APD_{80}$ and enlarged heart size. *Girk4$^{-/-}$* showed increased baseline HR and was more resistant to parasympathetic stimulation.

## 6.1 Introduction

A number of cardiac diseases such as hypertension and chronic heart failure have been linked to an imbalance in cardiac autonomic regulation wherein there is an increased sympathetic overdrive and a withdrawal of parasympathetic activity [60-63]. Contrary to initial belief that cardiac parasympathetic nerves are mainly localized to the atria, in particular the sino-atrial (SA) and atrio-ventricular (AV) nodes, in the past decade studies have suggested a greater role of parasympathetic innervation in ventricular physiology [64-67]. Recently, significant interest has been placed in investigating the efficacy of vagus nerve stimulation (VNS) as a therapy for metabolic and cardiovascular diseases. Multiple studies have reported beneficial effects of VNS in restoring autonomic imbalance by parasympathetic activation of the heart [68-71]. One hypothesis is that stimulation of the vagal nerve fibers innervating the ventricles can lead to positive remodeling of the heart and be used in the treatment of cardiovascular diseases such as hypertension and myocardial ischemia. However, despite the rising interest in parasympathetic modulation of the heart, the underlying mechanisms and ionic effects of activation of the ventricular vagal fibers remain unknown.

It has been established that the parasympathetic modulation of the heart is mediated by the muscarinic M2 receptors, which activate the G-protein coupled inwardly rectifying potassium ($K^+$) channels (GIRK) [72, 73]. The $M_2R$ receptors in cardiac myocytes activate G-proteins upon binding to acetylcholine (ACh). Subsequently, the activated G-protein can bind to GIRK causing an increased $K^+$ efflux ($I_{kACh}$). Hence, the release of ACh by activation of the vagus nerve causes an increased $I_{kACh}$ via the GIRK channels that are

composed of the GIRK1 and GIRK4 subunits. This results in membrane hyperpolarization, reduced action potential (AP) firing and correspondingly, a reduced heart rate (HR). Regulator of G-protein signaling (RGS) proteins negatively regulate G protein signaling thereby having an inhibitory effect on the GIRK channels, promoting their deactivation and increasing repolarization time [74-76]. Out of multiple RGS proteins, RGS6 has been specifically implicated in regulation of GIRK function and shown to play an essential role in cardiac parasympathetic activation [74-76]. However, given the common dogma that parasympathetic innervation and control of the heart is restricted to the SA and AV nodes, most studies have investigated the influence of the $M_2$R-GIRK-RGS6 pathway in atria. With rising evidence for parasympathetic innervation of the ventricles [64-67], there has been interest in characterizing the role this parasympathetic pathway plays in ventricular electrophysiology. A more recent study demonstrated the presence of the GIRK4 channels in cardiac ventricles across different species, suggesting an important contribution of the GIRK channels in parasympathetic control of the ventricles [72-74].

The main objective of our study is to investigate the role of the $M_2$R-GIRK4-RGS6 parasympathetic pathway in ventricular electrophysiology through loss-of and gain-of parasympathetic function mice models. We first evaluate structural remodeling effects of ablating GIRK4 (loss-of parasympathetic function) and RGS6 (gain-of parasympathetic function) by quantifying heart weight variances based on age, gender and genotype. Furthermore, we aim to determine the influence of GIRK4 and RGS6 modulation of parasympathetic function on ventricular electrophysiology, independent of any structural remodeling, using *in-vivo* ECG measurements and *ex-vivo* optical mapping.

## 6.2 Materials and Methods

All experiments were performed in accordance with the guidelines of the Institutional Animal Care and Use Committee at the University of Minnesota. Genetically modified $Girk4^{-/-}$ and $Rgs6^{-/-}$ mice models were created as previously described [76, 77]. Mice were divided into three groups (see Table 6.1): wild type (WT) mice as control; Girk4 knockout mice ($Girk4^{-/-}$) with ablated $I_{kACh}$ Girk4 subunit; and RGS6 knockout mice ($RGS6^{-/-}$) without the RGS6 protein. We first characterized any cardiac structural remodeling effects of ablating either GIRK4 or RGS6 in two age groups, 65 - 95 days and > 130 days postnatal (P). We then performed *in-vivo* and *ex-vivo* cardiac electrophysiological measurements in P65-95 mice to assess electrical characteristics independent of any structural effects.

### 1. Heart size measurements

We characterized the heart weight (H.W.) based on age and gender for all three mice genotypes. For each mouse, a quick thoracotomy was performed, the heart was excised and perfused with phosphate buffered saline (PBS) to flush out all the blood before the H.W. was measured. The tibia was harvested and its length (T.L.) was measured. The H.W. normalized by T.L. which remains constant after mouse maturity, was used to quantify heart sizes.

### 2. In-vivo ECG measurements

Mice were anesthetized with ketamine and xylazine (35 and 5 mg/kg, respectively) and ECG recordings were performed using IX-ECG recorder interfaced with Labscribe software. After 20 minutes of stabilization period, 10 minutes of baseline ECG was

recorded. Then, 300 nM of carbachol (CCh) was administered via a tail vein injection. The final concentration of CCh was estimated using approximated blood volume based on body weight of each mouse measured at the beginning of the experiment. After a 5 minute waiting period for the CCh to reach equilibrium, 10 minutes of ECG was recorded post CCh injection. The 10 minute baseline and post-CCh intervals of ECG recordings were used to calculate heart rate (HR), HR variability (HRV) and identify the arrhythmic episodes. Any noise artifacts were removed through data filtering and only clean segments of ECG data were used. A maximum HR threshold was set to 1000 bpm for baseline and mean baseline HR + 25 bpm for evaluating effect of CCh, in order to eliminate artefacts and erroneous spikes in HR. HRV was calculated as a ratio of standard deviation of HR to mean HR. Number of mice that exhibited arrhythmic episodes post injection of CCh were also quantified. An arrhythmic episode was defined as an occurrence of either bradycardia (at least 25 bpm < mean post CCh HR) or tachycardia (at least 25 bpm > post CCh HR) that lasted for over a 2 second duration.

### *3. Ex-vivo optical mapping experiments*

Isolated *ex-vivo* whole heart optical mapping experiments were performed as previously described [38, 50, 57]. To exclude any structural remodeling effects that may be induced by mouse age and sex differences, P65-95 mice of either sex were used for *Rgs6*^{-/-}, whereas predominantly male mice were used for WT and *Girk4*^{-/-} (see Table 6.1 and Fig. 6.1). Briefly, mice were first heparinized to avoid blood clots during heart excision. Ketamine and xylazine (100 mg/kg and 10 mg/kg, respectively) was administered to anesthetize the animal following which hearts were quickly excised and immersed in cold cardioplegic

solution (in mM: glucose 280, KCl 13.44, NaHCO$_3$ 12.6, and mannitol 34). The aorta was isolated under microscope for cannulation and the hearts were retrogradely perfused with warm (37±1°C) Tyrode's solution (in mM: NaCl 130, CaCl$_2$ 1.8, KCl 4, MgCl$_2$ 1.0, NaH$_2$PO$_4$ 1.2, NaHCO$_3$ 24, glucose 5.5, and pH 7.4) using Langendorff perfusion setup. After 15 minutes of stabilization, a bolus of the voltage sensitive dye, di-4-ANEPPS, 5 µg/mL was injected into the hearts. Two green lasers (532 nm, Shanghai Dream Lasers Tech., Shanghai, China) were used to excite the hearts and the fluorescence signal emitted was recorded from the left ventricular (LV) surface by a fast high resolution (14-bit, 80x80 pixels, 1000 frames/s) CCD camera (Little Joe, RedShirt Imaging, SciMeasure). Mechanical uncoupler Blebbistatin (10 µM) was added to the perfusate to reduce motion artifacts when required. Background fluorescence was eliminated during analysis by using spatial (3 x 3 pixels) and temporal convolution filters.

The hearts were paced at progressively decreasing basic cycle lengths (BCL), starting from 150 ms down to 60 ms in steps of 10 ms. At each BCL, 40 stimuli were applied to reach steady state, and optical movies corresponding to the last 10 stimuli were recorded and later analyzed. After capturing baseline recordings, hearts were injected with a bolus of CCh, either 300 nM (n = 5, 4 and 4 for WT, $Rgs6^{-/-}$ and $Girk4^{-/-}$ respectively) or 3 µM (n = 3 and 3 for WT and $Girk4^{-/-}$ respectively). After 10 minutes of stabilization, similar pacing protocol was repeated and optical movies were captured.

*4. Ex-vivo parameter measurements*

Optical movies were analyzed to characterize the electrophysiological properties of the LV. The action potential duration (APD) was calculated at 80% (APD$_{80}$) repolarization.

For each mouse, average of 5 action potentials was used to calculate mean $APD_{80}$ at each pixel. Two dimensional (2D) APD maps were then constructed as described previously [50, 57] to demonstrate the spatial distribution of APD. For each heart and at each BCL, average APD value for the entire LV surface was then calculated from individual pixel values. To investigate the dispersion of repolarization in LV, $APD_{80}$ heterogeneity was calculated based on the heterogeneity index μ as,

$$\mu_X = (X^{95} - X^5) / X^{50}$$

where X is $APD_{80}$, $X^{95}$ and $X^5$ represent the 95th and 5th percentiles of the $APD_{80}$ distribution, and $X^{50}$ is the median of the $APD_{80}$ distribution. Conduction velocity (CV) was calculated as described previously [57]. Specifically, the distributions of activation times measured at $(dV/dt)_{max}$ for the spatial regions of 3 x 3 pixels were fitted with the plane, and gradients of activation times were calculated for the each plane. The magnitude of the local CV was calculated for each pixel. APD restitution curves were generated by plotting mean $APD_{80}$ as a function of mean diastolic interval $(DI = BCL - APD_{80})$. The maximum slope of APD restitution, $S_{max}$, was calculated by fitting with 2nd degree polynomial and evaluating its derivative at the lowest DI value for each run. Mean $S_{max}$ was then calculated for each genotype both at baseline and post administration of CCh.

## 5. Statistics:

All data are presented as mean ± standard error. Statistical comparisons between the three genotypes were performed using 1-way ANOVA (Origin Software, Northampton, MA, USA). Since there was no statistical difference between the baseline $APD_{80}$ values for the 300 nM and 3 μM CCh groups, a single combined baseline was used. Comparison of

dosage dependent CCh and baseline data was then performed using 1-way ANOVA. Fisher's exact test was used to perform statistical comparison of the number of mice that exhibited arrhythmias across the three mice groups. Values of $P < 0.05$ were considered statistically significant.

## 6.3 Results

### *1. Structural remodeling of loss-of and gain-of parasympathetic function:*

We first investigated the structural differences between the three mouse genotypes considering both sex and age (see Fig.6.1). In P65-95 *Girk4$^{-/-}$* mice (Fig.6.1A), loss of parasympathetic function led to a significant decrease in the heart size, compared to both WT and *Rgs6$^{-/-}$* hearts (p < 0.05). In contrast, there was only a moderate increase in heart size of P65-95 *Rgs6$^{-/-}$* mice. However, this heart size increase in P>130 *Rgs6$^{-/-}$* mice became significant (p < 0.05, Fig.6.1C). To further elucidate if the heart size differences between the genotypes were sex dependent, we compared heart sizes between males and females for each group. As seen in Fig.6.1B, there was a significant difference in the P65-95 male and female heart sizes within each knockout mice genotype, which was absent in WT mice. The overall reduction in young *Girk4$^{-/-}$* mice heart size seemed predominantly due to smaller female *Girk4$^{-/-}$* mouse hearts (Fig.6.1B). Female WT hearts were significantly larger in size compared to *Girk4$^{-/-}$* females. The difference in P>130 WT and *Rgs6$^{-/-}$* mice hearts also seemed to be predominantly due to larger female *Rgs6$^{-/-}$* hearts than female WT mice hearts (Fig.6.1D). Overall, the results suggest that ablation of RGS6 protein led to an enlargement in heart size which enhanced with aging, while *Girk4$^{-/-}$* led to a reduction in heart size. The heart size differences between the knock out mice and WT were mainly due

to differences in female hearts. Hence, for our ex-vivo optical mapping experiments, to eliminate any structural remodeling effects, we used young mice, with a mix of males and females for *Rgs6$^{-/-}$* and predominantly male WT and *Girk4$^{-/-}$* mice.
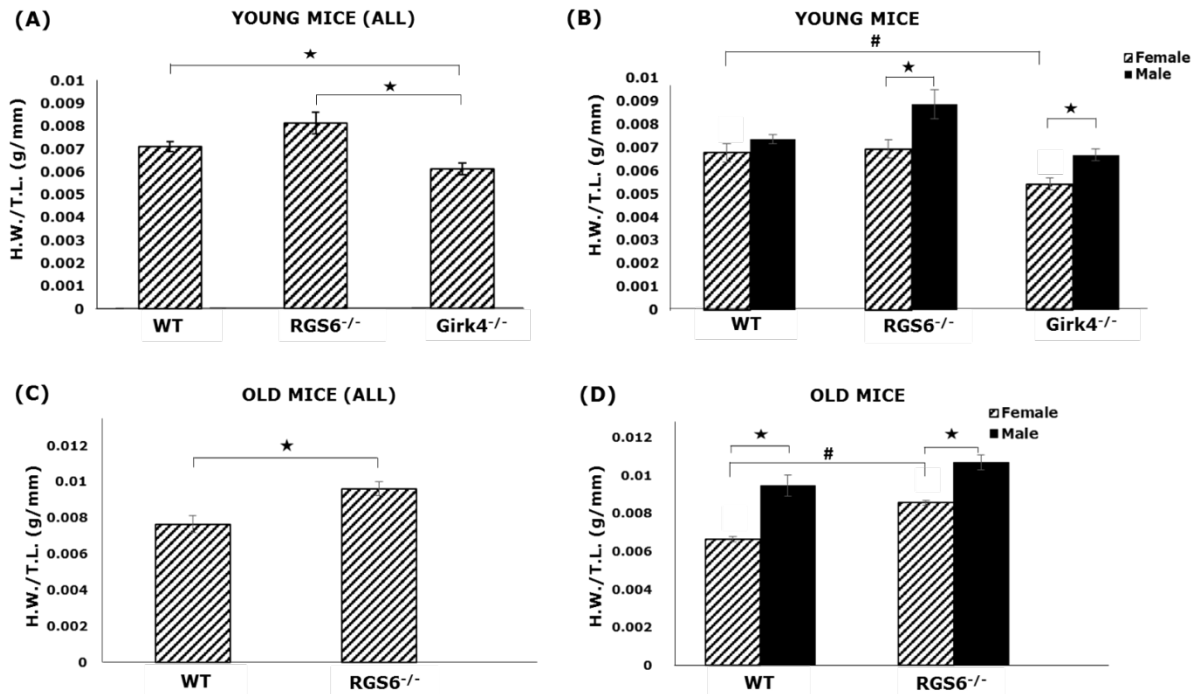


*Figure 6.1 Characterization of heart sizes: (A) Comparison of heart sizes (H.W. / T.L.) in young WT, RGS6$^{-/-}$ and Girk4$^{-/-}$ mice. '\*' denotes statistical significance of p < 0.05 between Girk4$^{-/-}$ and both WT and RGS6$^{-/-}$. (B) Gender dependent comparison of WT, RGS6$^{-/-}$ and Girk4$^{-/-}$ mice. '#' denotes statistical significance of p < 0.05 between WT and Girk4$^{-/-}$ female mice, '\*' denotes statistical significance of p < 0.05 between male and female mice for the same genotype. (C) Comparison of heart sizes in old WT and RGS6$^{-/-}$ mice. '\*' denotes statistical significance of p < 0.05. (D) Gender dependent comparison of heart sizes in old WT and RGS6$^{-/-}$ mice. '#' denotes statistical significance of p < 0.05 between female mice, '\*' denotes statistical significance of p < 0.05 between male and female mice for the same genotype.*

*2. In-vivo effect of parasympathetic modulation.*

Fig.6.2A, B presents HR and HRV data for WT, Girk4 and RGS6 mice at baseline and after parasympathetic stimulation with 300 nM CCh. Fig.6.2A demonstrates that at baseline, $Rgs6^{-/-}$ showed a significantly lower HR compared to both WT and $Girk4^{-/-}$ mice, but HRV showed no significant difference between the three genotypes. Parasympathetic stimulation by injection of 300 nM CCh led to a significant drop in HR for both the WT and $Rgs6^{-/-}$ mice compared to their respective baselines, while there was no significant change in HR for the $Girk4^{-/-}$ mice. In addition, CCh significantly increased HRV in WT and $Rgs6^{-/-}$ mice, which correlated with an increased number of mice exhibiting arrhythmias in these two groups (Fig.6.2B, C). Fig.6.2D shows representative examples of bradycardia and tachycardia episodes in WT and $Rgs6^{-/-}$.

*3. Ex-vivo optical mapping assessment of loss and gain of parasympathetic function:*

*1. Effect on action potential duration.* We investigated the changes in baseline $APD_{80}$ as a result of ablating either Girk4 or RGS6 compared to WT mice. Fig.6.3A displays the change in LV $APD_{80}$ with decrease in BCL for the three genotypes at baseline. As seen in the figure, mice lacking Girk4 show a prolongation in baseline $APD_{80}$, in comparison to WT mice. $Rgs6^{-/-}$ mice had prolonged $APD_{80}$ at higher BCLs. Representative 2D $APD_{80}$ maps along with action potential traces for the three genotypes during baseline and post injection with CCh, at a BCL of 120 ms are shown in Fig.6.3B. The action potential traces demonstrate a larger $APD_{80}$ at baseline for both $Girk4^{-/-}$ and $Rgs6^{-/-}$ CCh stimulation significantly increased $APD_{80}$, and the effect was dose dependent, as shown in Figs.6.3C-E. Since 3 μM CCh led to a loss of HR response in $Rgs6^{-/-}$ mice, only 300 nM

81

CCh dosage was used in these mice, which led to a significant elongation in $APD_{80}$. *Girk4*$^{-/-}$ mice show a shunted effect of parasympathetic stimulation compared to WT mice, exhibiting a significant prolongation in $APD_{80}$ only at a high CCh dosage of 3 μM.
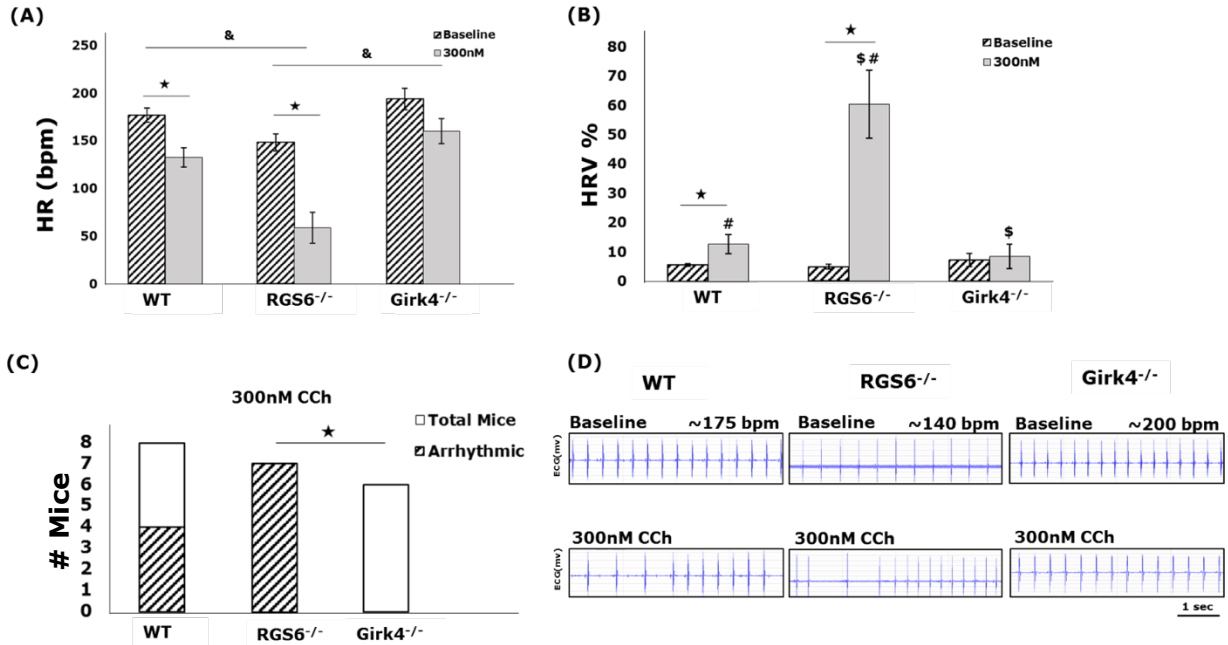


*Figure 6.2 In-vivo ECG measurements: Comparison of (A) HR and (B) HRV, between WT, Girk4*$^{-/-}$ *and Rgs6*$^{-/-}$ *mice at baseline and post injection of 300 nM CCh. '*' denotes statistical significance of $p < 0.05$ between baseline and 300 nM CCh within the same genotype. '&' denotes statistical significance of $p < 0.05$ for both baseline and 300 nM CCh across genotypes. '#' denotes statistical significance of $p < 0.05$ between WT and Rgs6*$^{-/-}$ *mice at 300 nM CCh; '$' denotes statistical significance of $p < 0.05$ between Girk4*$^{-/-}$ *and Rgs6*$^{-/-}$ *mice at 300 nM CCh. (C) Quantification of the total number of mice that exhibited arrhythmias post injection of 300 nM CCh. '*' denotes statistical significance of $p < 0.05$ between Girk4*$^{-/-}$ *and Rgs6*$^{-/-}$*. (D) Representative examples of ECG data highlighting episodes of arrhythmia in WT and Rgs6*$^{-/-}$ *post injection of CCh, and no arrhythmia in Girk4*$^{-/-}$ *mice.*

*2. Slopes of restitution $S_{max}$.* Administration of CCh increased the slopes of restitution in all the three genotypes as demonstrated by Fig.6.4. For WT and *Girk4^{-/-}*, we observed a dose dependent effect of parasympathetic stimulation, with 3 μM CCh leading to significantly larger $S_{max}$. *Rgs6^{-/-}* had the most apparent effect of parasympathetic overdrive and showed steepening of restitution slopes with 300 nM CCh stimulation.



*Figure 6.3 Ex-vivo optical mapping data: Effect on APD$_{80}$ (A) Change in average APD$_{80}$ with decreasing BCLs for each genotype at baseline. '#' denotes statistical significance of $p < 0.05$ between WT and Girk4^{-/-}. '$' denotes statistical significance of $p < 0.05$ between WT and Rgs6^{-/-}. (B) Representative 2D APD$_{80}$ maps for all 3 genotypes, at a BCL of 120ms both at baseline and post CCh injection. Representative action potential traces shown at baseline (top panel, pixels marked by \*) and demonstrating effect of CCh (bottom panel, pixels marked by Δ). (C-E) Effect of CCh on APD$_{80}$ for WT, Girk4^{-/-} and Rgs6^{-/-} respectively. '\*' denotes statistical significance of $p < 0.05$ between baseline and 300 nM CCh; '&' denotes statistical significance of $p < 0.05$ between baseline and 3 uM CCh.*

*3.Effect on conduction velocity and APD$_{80}$ heterogeneity.* Fig.6.5A shows the change in LV CV with decreasing BCL for the three genotypes at baseline. There was no difference in the CV values across the genotypes at baseline. No significant effect of parasympathetic stimulation using CCh was observed in any of the genotypes (Figs.6.5C-E). Fig.6.5B shows representative activation maps demonstrating smooth propagation of action potentials for all the three groups both at baseline and post CCh.
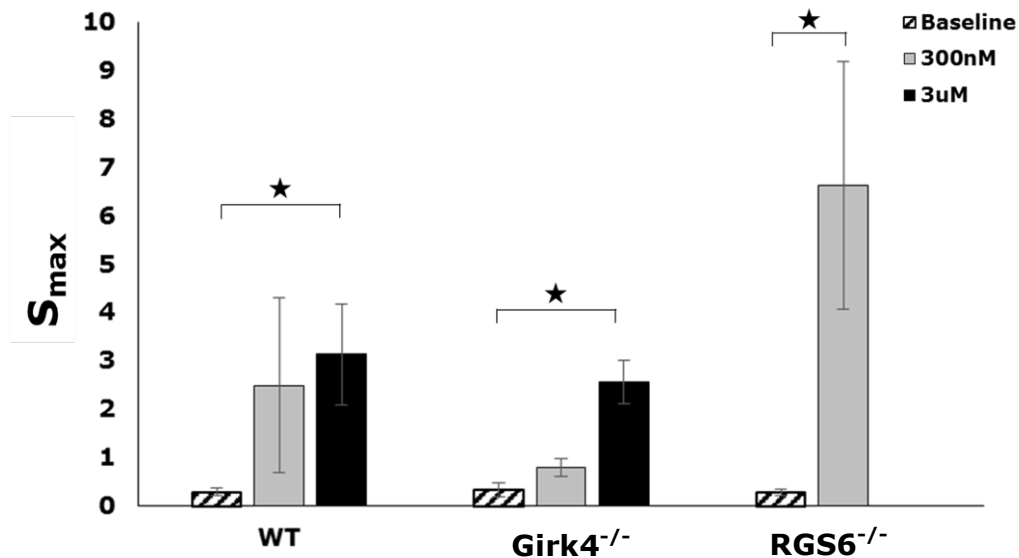


*Figure 6.4 Comparison of the effect of CCh on the slopes of restitution S$_{max}$, in WT, Girk4$^{-/-}$ and Rgs6$^{-/-}$ mice. '*' denotes statistical significance of p < 0.05 between post CCh and baseline for the same genotype.*

The change in LV APD$_{80}$ heterogeneity for the three mice groups with decreasing BCL at baseline is shown in Fig.6.6A. No significant differences in heterogeneity was observed between the three mice groups, both at baseline and post injection of CCh (Figs.6.5B-D).
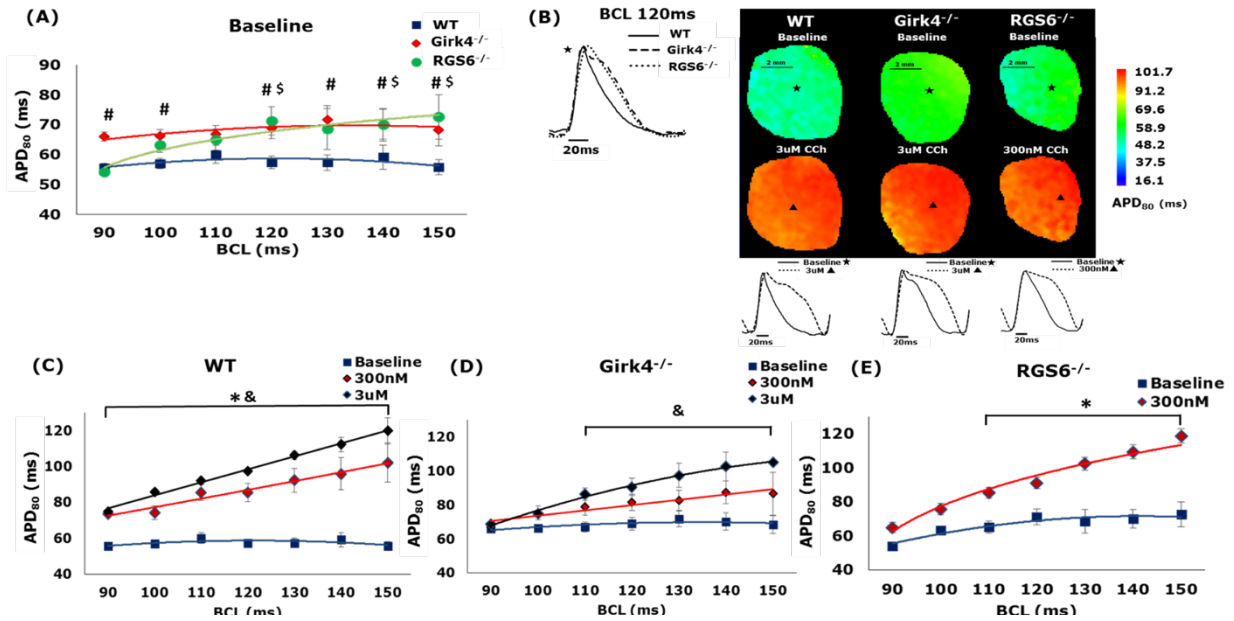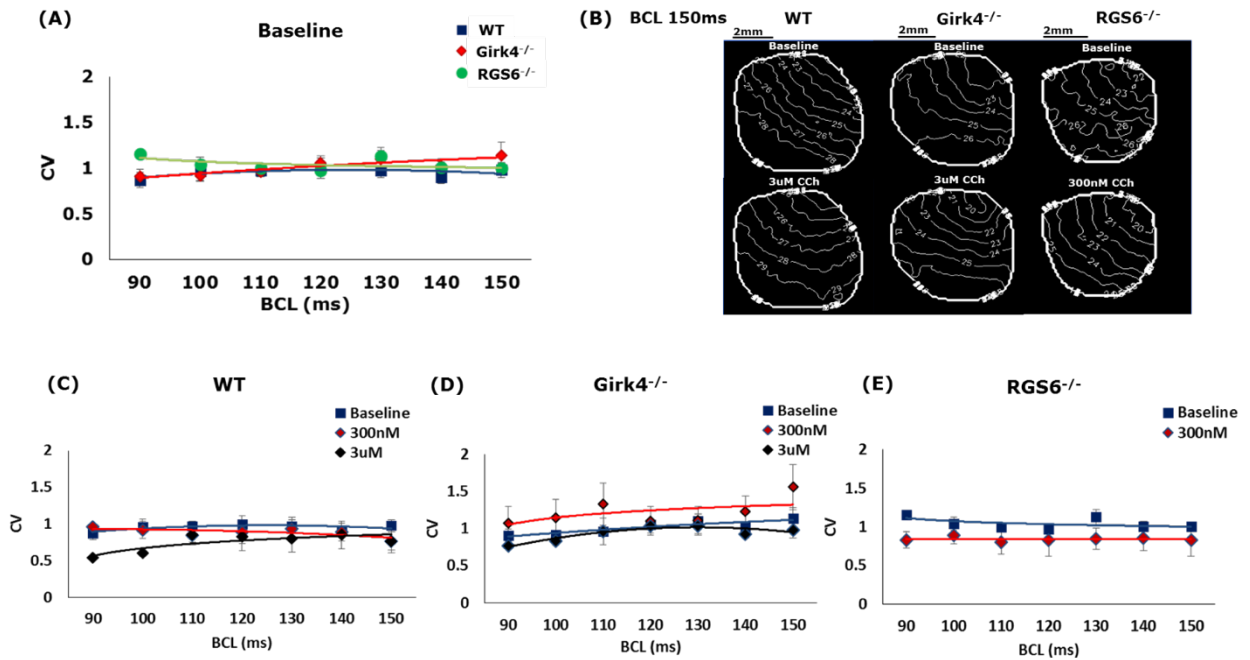
*Figure 6.5 Ex-vivo optical mapping data: Effect of CV (A) Change in average CV with decreasing BCLs for each genotype at baseline. (B) Representative 2D activation maps for all 3 genotypes, at a BCL of 150ms both at baseline and post CCh injection. (C-E) Effect of CCh on CV for WT, Girk4^{-/-} and Rgs6^{-/-} respectively.*

## 6.4 Discussion

It is well established that the autonomic nervous system (ANS) plays an important role in regulating cardiac electrical activity. Both branches of the ANS, namely the sympathetic and parasympathetic systems, directly innervate the heart and influence cardiac electrophysiology. While a stimulation of the sympathetic system increases cardiac contractility, HR and conductivity, stimulation of the parasympathetic system has an opposite effect. Under diseased conditions such as hypertension and chronic heart failure, we see an imbalance in autonomic activity [60-63]. However, the effects of modulating the

ANS on cardiac electrical activity remain confounding due to a lack of understanding of the existence and function these pathways play in cardiac electrophysiology. Here, we aimed to investigate the effect of modulating the known $M_2R$ mediated GIRK parasympathetic pathway on ventricular electrical activity. Using specific knock out models for GIRK4 and RGS6, we confirm the definite role of this pathway in modulating murine ventricular physiology. We also show that an imbalance in parasympathetic function (using loss-of and gain-of function models) affect both cardiac structural and electrophysiological properties.
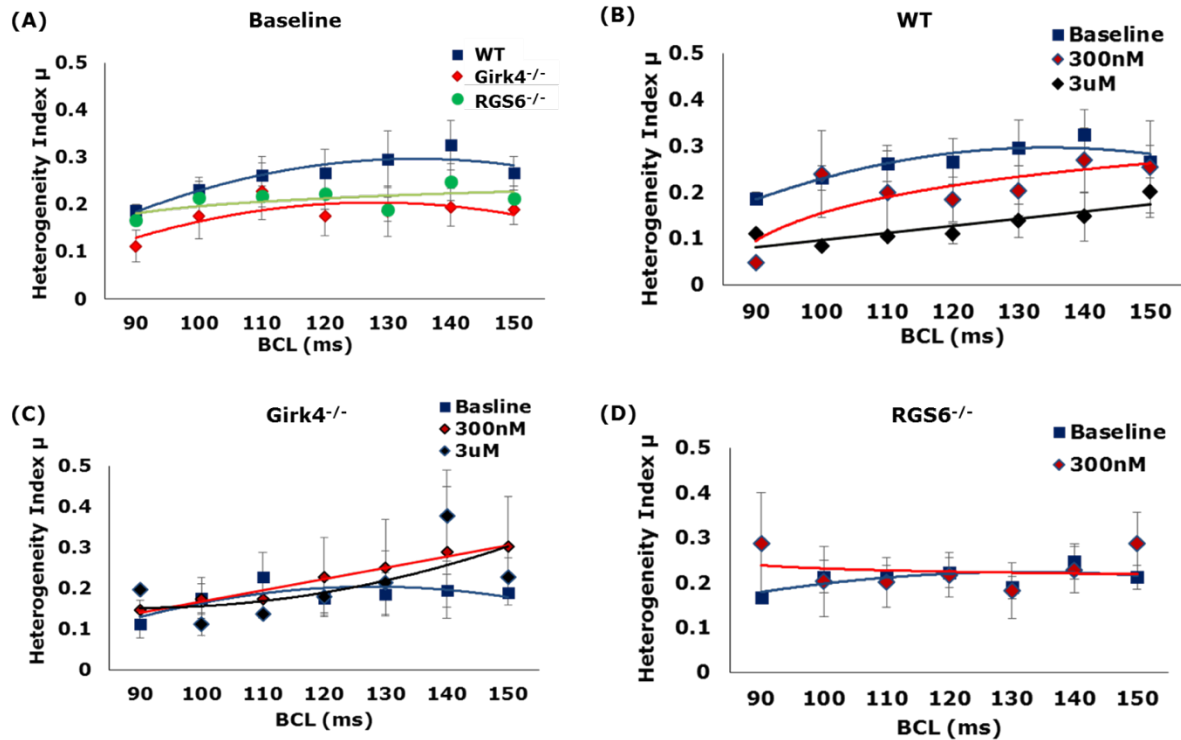


Figure 6.6 Ex-vivo optical mapping data: Effect on heterogeneity (A) Change in average heterogeneity index μ with decreasing BCLs for each genotype at baseline. (B-D) Effect of CCh on heterogeneity index μ for WT, Girk4$^{-/-}$ and Rgs6$^{-/-}$ respectively.

Our major findings are as follows: (1) Ablation of GIRK4 and RGS6 can lead to structural remodeling in the heart. (2) Parasympathetic stimulation of *Girk4*$^{-/-}$ and *Rgs6*$^{-/-}$

mice leads to a dose dependent prolongation in $APD_{80}$ and steepening of APD restitution.

(3) The $M_2R$- GIRK4-RGS6 pathway plays an important role in modulating ventricular electrophysiology and overall cardiac dynamics.

*In-vivo ECG and Structural Effects:*

Our *in-vivo* ECG data displayed a significant difference in baseline HRs across the three groups (Fig.6.2). As expected in $Girk4^{-/-}$ mice, ablation of the GIRK4 led to a loss-of parasympathetic function, leading to a slightly higher baseline HR compared to WT. On the other hand, ablation of RGS6 led to a gain-of parasympathetic function model, demonstrated by a significant decrease in baseline HR. $Rgs6^{-/-}$ mice also had the most pronounced effect of parasympathetic stimulation using CCh. Since RGS6 plays an inhibitory role of reducing $I_{kACh}$, ablation of RGS6 led to an increase in parasympathetic activation and drop in baseline HR. Further stimulation with CCh led to a parasympathetic overdrive and severe bradycardia in these hearts. The electrical instability created by parasympathetic overdrive is also depicted in the large HRV post CCh injection and the onset of arrhythmias in $Rgs6^{-/-}$ hearts. WT hearts showed a modest drop in HR as an effect of parasympathetic stimulation by CCh, while in $Girk4^{-/-}$ mice we saw a shunted effect of parasympathetic activation with no significant drop in HR. This can be attributed to a reduced $I_{kACh}$ in $Girk4^{-/-}$ mice, leading to a withdrawal of parasympathetic function.

Interestingly, we a saw a difference in heart sizes between the three genotypes. $Rgs6^{-/-}$ mice had significantly enlarged hearts, while $Girk4^{-/-}$ mice had a reduction in heart size compared to WT (Fig.6.1). This suggests that a chronic imbalance in parasympathetic function, specifically an overdrive of parasympathetic activity could lead to structural

remodeling of the heart. While there is prior evidence of the role of RGS6 in protecting against cardiac ischemic injury and aiding tumor suppression [78-80], a more detailed study would be needed to corroborate our current findings. However, our preliminary data show evidence of a gender and age dependent effect of parasympathetic overdrive on cardiac size.

*Ex-vivo Results:*

To characterize the role of the $M_2R$-GIRK4-RGS6 pathway in ventricular electrophysiology, we analyzed $APD_{80}$, CV and the heterogeneity index $\mu$. We observed a prolongation in $APD_{80}$ at baseline in *Girk4$^{-/-}$* and *Rgs6$^{-/-}$* mice. Since GIRK4 is a critical subunit contributing to $I_{kACh}$, the observed effect of its ablation on ventricular repolarization can be attributed to a loss of this current in these mice. *Rgs6$^{-/-}$* mice showed a prolongation in $APD_{80}$ only at certain higher BCLs with a sharp drop in $APD_{80}$ at lower BCLs, highlighted by the larger $S_{max}$. This supports prior evidence of the arrhythmogenic effects of RGS6 ablation [74, 81]. Although previous studies have investigated the effect of RGS6 ablation on atrial APD [74-76], their role and impact on ventricular electrophysiology is relatively unknown. This is the first study to investigate the effect of RGS6 ablation on electrical restitution and characterize its effect on ventricular APD at different pacing rates. Our results strongly indicate that RGS6 does play an important role in ventricular repolarization via direct modulation of $I_{kACh}$.

Parasympathetic stimulation using CCh showed a significant increase in $APD_{80}$ in WT mice. CCh has been shown to decrease APD in healthy hearts and isolated atrial myocytes previously [82-85] mediated by an activation of $I_{kACh}$. However, there has been

contradictory evidence provided showing an increase in APD with vagal stimulation [86-88]. Furthermore, since CCh is a non-selective cholinergic agonist, it can lead to activation of both nicotinic and muscarinic receptors. As nicotinic receptors are known to mediate cholinergic neurotransmission, CCh could stimulate both sympathetic and parasympathetic post-ganglionic neuronal activity. Indeed, it has been shown that the anti-fibrillatory effects of vagal stimulation occur via post-ganglionic efferent nerve fibers independent of muscarinic receptor activation [88, 89]. Hence, the increase in ventricular repolarization seen in WT mice could be attributed to the combined effect of both nicotinic and muscarinic receptors activation. We see a reduced effect on $APD_{80}$ in the loss-of parasympathetic function model ($Girk4^{-/-}$) while an enhanced effect in the gain-of parasympathetic function model ($Rgs6^{-/-}$). However, in all three genotypes, CCh increased the slopes of restitution, with the biggest effect observed in $Rgs6^{-/-}$. An increased restitution slope is hypothesized to be pro-arrhythmic with prior studies claiming that onset of arrhythmias can occur when the magnitude of restitution slope exceeds one [7, 13]. $Rgs6^{-/-}$ had the maximum slope of restitution post injection of CCh. This supports the in-vivo data wherein parasympathetic overdrive caused an increase in arrhythmic episodes in $Rgs6^{-/-}$ mice.

Due to the complex interplay between the sympathetic and parasympathetic receptors in conjunction with possible electrical remodeling in the knock out mice, it is difficult to attribute the effect of CCh stimulation on the whole heart ventricular repolarization to a specific current or protein. However, it is apparent that both GIRK4 and RGS6 play a role in modulating ventricular repolarization. There was no significant effect of either Girk4 or RGS6 knock out on conduction velocity or heterogeneity (Figs.6.4 and

6.5). Since conduction velocity is predominantly affected by sodium channel activity, a lack of significant effect of $I_{kACh}$ on ventricular conduction was not surprising.

In summary, our data provides evidence supporting the role of parasympathetic innervation on murine ventricular physiology. We establish that the $M_2R$-GIRK4-RGS6 pathway plays an important role in modulating ventricular repolarization. While $Rgs6^{-/-}$ enhances parasympathetic function, $Girk4^{-/-}$ leads to a loss-of parasympathetic function model. These loss-of ($Girk4^{-/-}$) and gain-of ($Rgs6^{-/-}$) parasympathetic function models could help better understand the effects of autonomic imbalance and parasympathetic modulation on cardiac function and ventricular electrophysiology. In addition, by developing atrial and ventricular specific knock out models, we can investigate the specific contributions of $I_{kACh}$ in regulating APD and identify possible atrial components indirectly affecting ventricular signaling. Furthermore, by using nicotinic blockers and suppressing sympathetic activation, we can isolate the effect of parasympathetic stimulation on APD. However, given the complex interplay between the sympathetic and parasympathetic systems, it is essential to understand the global electrophysiological responses in the whole heart as a result of possible autonomic imbalance. Hence, in this study we aimed to characterize cardiac electrical function in both a loss-of and gain-of parasympathetic function model. Overdrive of parasympathetic system ($Rgs6^{-/-}$) made the heart more prone to arrhythmias, severe bradycardia, excessive HRV, prolongation of ventricular $APD_{80}$ and possible enlargement of heart. Diminished parasympathetic system ($Girk4^{-/-}$) was more resistant to parasympathetic activation, showed increased baseline HR and needed an increased dosage of parasympathetic stimulant to equal WT characteristics. These findings could be a basis

for further studies exploring the role of autonomic innervation on ventricular electrophysiology.

## 6.5 Acknowledgments

| Measurement | WT (n) | RGS6$^{-/-}$ (n) | Girk4$^{-/-}$ (n) | Age (days) | Gender |
|---|---|---|---|---|---|
| | 6 | 8 | 7 | 65-95 | Male |
| | 5 | 5 | 6 | 65-95 | Female |
| Heart Size | 4 | 6 | - | >130 | Male |
| | 7 | 6 | - | >130 | Female |
| In-vivo ECG | 5 | 4 | 4 | 65-95 | Male |
| | 3 | 4 | 2 | 65-95 | Female |
| Optical Mapping | 7 | 2 | 8 | 65-95 | Male |
| | 1 | 3 | - | 65-95 | Female |
| Total (n) | 38 | 38 | 27 | | |

*Table 6.1. Summary of mice used for experiments*

# CHAPTER 7: DISCUSSION AND FUTURE WORK

This research targeted multiple aspects in the study of predicting and preventing the onset of cardiac alternans. It required application of engineering principles from non-linear dynamics and feedback control systems along with fundamentals of cardiac electrophysiology, to develop novel techniques for suppressing alternans. The main accomplishments of this research are:

1) Development of a novel real-time closed loop algorithm for beat-to-beat cardiac control based on ECG detection,

2) Successful implementation of feedback elimination using Constant DI pacing and validation of its beneficial anti-arrhythmic effects using ex-vivo isolated whole hearts,

3) Highlighting the importance of feedback elimination as opposed to feedback modulation using stochastic pacing,

4) Implementing a pacing technique to induce alternans and conclusively characterizing the transition from steady state to alternans as smooth bifurcation, and

5) Characterizing the effects of modulating the parasympathetic pathways on cardiac dynamics and ventricular electrophysiology.

The concepts established in this research have the potential for clinical translation and with further preclinical validation could be a source for improving the current treatment strategies for cardiac arrhythmias.

## 7.1    Clinical Translation of Constant DI

Here, we performed a comprehensive study of different pacing techniques, based on the foundation that feedback between DI and APD is inherently pro-arrhythmic. We used the onset of alternans as an indication of the stability of the heart by investigating its proclivity to transition into abnormal rhythms. Expectedly, we established the resistivity of constant DI pacing to the formation of alternans in the heart, thus suggesting the anti-arrhythmic benefits of feedback elimination.

These promising results could be the first step in the preclinical adaptation of constant DI pacing in a prototype pacemaker. The next step in translating this research into a clinically relevant therapeutic device, would be to perform experiments in a swine model to test the efficacy of constant DI pacing *in-vivo*. A swine model lays the foundation for smoother adaptability into potential future human studies. Positive reviews from clinicians during interactions at conferences where this research was presented, suggest optimistic opportunities for clinical collaborations in pursuing this end goal.

Pacemaker technology has rapidly advanced in the last two decades with better rate-responsive algorithms incorporating timing cycles that can track both the atrial and ventricular activity. Various control algorithms have been developed and implemented in pacemakers enabling detection of irregular cardiac rhythms and application of rate responsive stimulation for modulation of heart rate. To validate effects of feedback elimination *in-vivo*, a contemporary pacemaker can be potentially re-programmed to implement the constant DI pacing protocol. Specifically, the pacemaker can be customized to detect the RT and TR intervals which correspond to the APD and DI, in real time. After

every detected T wave, a time interval equivalent to the predefined constant DI value could be activated, at the end of which a pacing stimulus could be applied.

This is the first attempt at extending the concept of feedback modulation and formation of alternans and developing a clinically relevant therapeutic solution for the prevention and control of cardiac arrhythmias. This research aimed at developing a physiologically relevant and potentially anti-arrhythmic pacing mechanism. It challenged the contemporary periodic pacing methodology based on a solid proven mathematical foundation and published numerical simulation data. The real-time control algorithm developed for the experimental validation of constant DI pacing is a novel implementation of closed loop control of isolated whole hearts. It opens the doors for the modulation of cardiac electrical activity in real-time during various diseased states and abnormal rhythms. Furthermore, it utilizes the spatiotemporally flexible, high resolution technique of optical mapping for the assessment of different pacing techniques and their electrophysiological effects on whole hearts. Most importantly, the successful adaptation of constant DI pacing into a clinically viable device could improve the quality of life of patients suffering from abnormal cardiac rhythms.

## 7.2    Real-time Closed Loop Optical Mapping

To eliminate feedback and control the DI on a beat-by-beat basis, we currently utilize the electrical signal from real-time ECG data. As described in Chapter 5, we detect T-waves on the ECG and control the TR intervals in real-time while optical mapping is performed in conjunction to record 2D videos during the experiment. The optical videos are then post processed to assess the spatio-temporal efficacy of the pacing technique in

suppressing alternans. However, another potentially useful technique for cardiac control would be to utilize 2D feedback information based on the optical signal emitted, in order to provide the flexibility of targeting specific substrates across the whole heart. Hence, an algorithm to detect an action potential in real-time from the fluorescence signal emitted during optical mapping, and to enable control over the succeeding DI, could help utilize the high resolution features of the optical signal, combined with the spatial flexibility of 2D imaging.

There are a number of technical challenges in incorporating closed loop control using optical signals. (1) Fluctuations in fluorescence intensity make it difficult to track an action potential in real time. The baseline can vary based on experimental conditions and needs to be identified in real time during each run. (2) Considering the large size of the two-dimensional images, communication between the camera and computer memory can act as a bottleneck in high-speed signal acquisition. Most cameras use a frame grabber that captures images sequentially and transmits to the host computer. This introduces a latency in the signal processing. (3) Operating systems like Microsoft Windows or Linux, are not hard real time operating systems and have inherent processing latencies. For successful determination of APD and control over DI, the system delay needs to be maintained under 30ms. (4) Motion artefacts can be present during optical mapping experiments which make it essential to have spatial and temporal filtering to extract useful information from the feedback signal. Performing spatiotemporal filtering on discrete data samples in real time with minimal added latency forms an interesting challenge. Here, as a first step, I implemented a control algorithm and validated it using previously acquired optical videos

[90]. Two distinct aspects of the algorithm were tested, namely real-time APD capture and signal processing for real-time APD detection and DI control.

Fig.7.1A shows the schematic of the optical mapping setup and the algorithm for real-time detection of APD and stimulation. The setup consisted of a fast 14-bit, 80 × 80-pixel resolution camera (Little Joe, RedShift Imaging, SciMeasure) connected to a personal computer (PC, with windows XP OS, CPU 2.5 GHz, 3GB RAM) using a camera link digital camera interface (EDT PCI DV C-Link/SC). The real-time data was processed using a LABVIEW based custom written program. To account for experimental noise and motion artifacts, spatial filtering was performed. The average optical data from a specified region of interest (3x3 matrix of pixels) was processed on a frame by frame basis and the start and end of an action potential was detected in real-time. At the end of each detected action
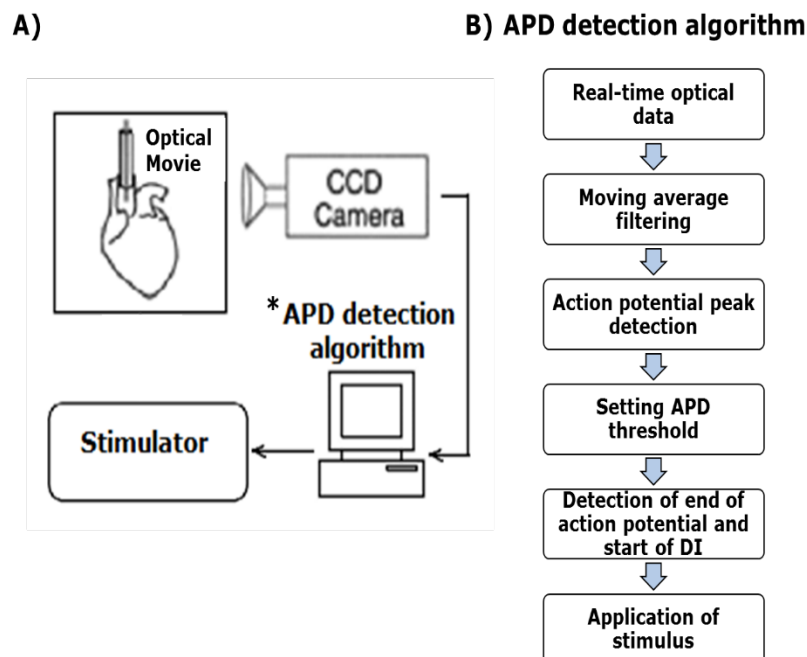


Figure 7.1. A) Schematic of the optical mapping system for real time APD measurement; B) Flowchart summarizing the APD detection algorithm

potential, a stimulus was applied using a stimulator (World Precision Instruments, A385, Stimulus Isolator).

The APD detection algorithm (Fig.7.1B) consisted of acquiring the optical images in real time from the CCD cameras and performing initial moving average filtering in order to remove noise from the raw data. The moving average queued a predefined number of input data samples and calculated the average value. With each new data sample, the top of the queue was emptied and the average was recalculated based on the updated data sequence. The queue length for calculating the moving average could be adjusted based on the variable noise artifacts in input data observed under experimental conditions. The action potential peaks were then detected from the filtered data. The repolarization threshold was calculated in real-time for each action potential based on the peak amplitude.
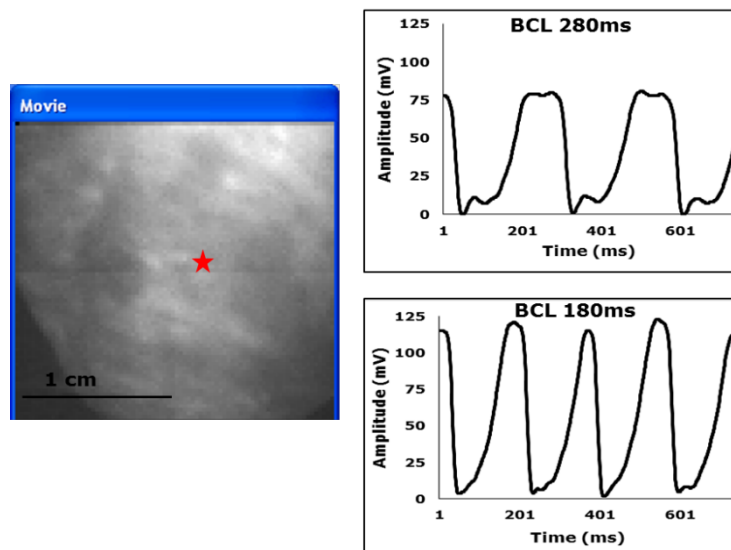


*Figure 7.2 Left: An image of the LV surface from the recorded optical mapping movie; Right: Action potential traces from a single pixel denoted by \*, from the LV of a rabbit heart paced at a BCL of 280ms and 180ms*

APD$_{80}$ (APD calculated at 80% repolarization) was used to detect the end of each action potential, post which a stimulus was applied.

In order to test the real-time APD detection algorithm, optical movies recorded from the LV surface of the rabbit heart at two different BCLs were first analyzed. Fig.7.2 shows the action potential traces from a single pixel of the rabbit heart for a BCL of 280ms and 180ms. The pixel was chosen arbitrarily for validation purposes and showed similar results for different locations of the heart. Note that the action potential traces are inverted, which is a property of the dye used for recording the voltage activity. The APD$_{80}$ from the single pixel location was calculated, denoted by * in Fig.7.2 for both the BCLs. The APD$_{80}$ was 176.213ms and 128.96ms for a BCL of 280ms and 180ms respectively. The modified optical mapping setup shown in Fig.7.1A was then used to test the capture of action potentials in real time. Previously recorded optical mapping movies of the rabbit heart (see Fig.7.2) were replayed in real-time and the algorithm to capture the action potentials was tested. Fig.7.3 shows the action potential traces captured using the real-time software.



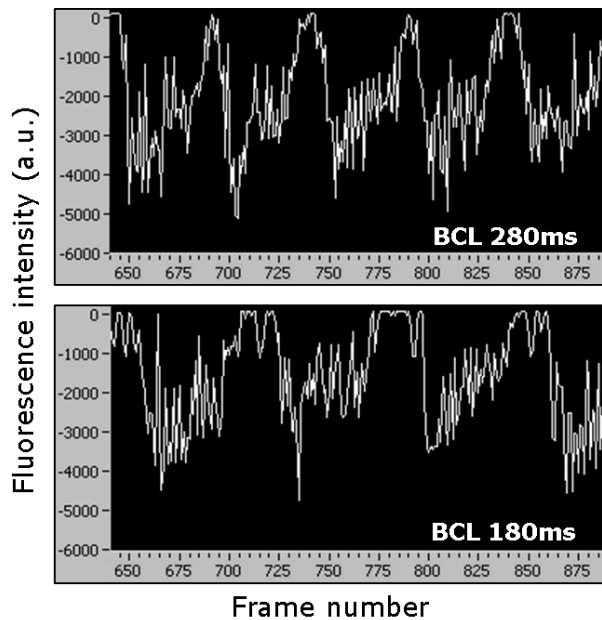*Figure 7.3 Traces of action potential at BCL 280ms and 180ms using real-time APD detection software*

As seen from Fig.7.3, the real-time software captured the train of action potentials generated at both the BCLs in the paced rabbit heart. There was a close correspondence to the optical movies recorded earlier (Fig.7.2). As seen from Figs.7.2 and 7.3, the shape and duration of the action potentials recorded was similar and varied in accordance with the BCL. Note that the x axis in Fig.7.3 is not time but the frame number. The real time data
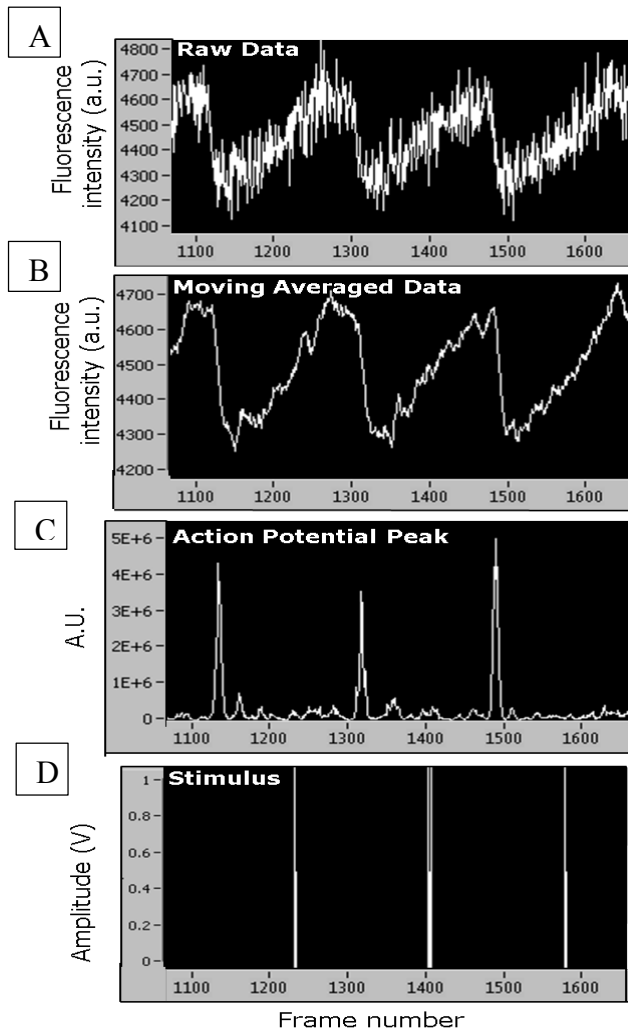


*Figure 7.4 Real-time detection of action potential and application of stimulation*

was captured, processed and displayed on a frame-by-frame basis. Therefore, for a sampling rate of 1 kHz, we could potentially capture 1 frame/ms. However, due to the inherent system delays introduced by the camera frame grabber and the signal processing algorithm, the actual frame rate was lower than the maximum. This was still within the rate required to capture the start and detect the end of successive action potentials as seen from Fig.7.3. The real time data (Fig.7.3) however, was much noisier than the original data (Fig.7.2) since no filtering or other processing was performed. The pixel

location used to detect the action potential could be changed during experiments, thus providing the flexibility to get feedback based on different regions of the heart.

Next, the APD detection and stimulation algorithm (see Fig.7.1B) was tested. Fig.7.4 shows the step by step results of the APD detection and stimulation algorithm that was tested on a simulated raw data sampled frame-by-frame to emulate the actual experimental conditions. The simulated raw data is shown in Fig.4A, which consists of a train of action potentials read by the APD detection algorithm as a sequence of data samples, similar to the real-time experimental data. Note that the raw data shown in Fig.7.4A is similar to the action potential traces captured in real-time (Fig.7.3). Panel B shows the application of the moving average filter on the raw data. It calculates the average based on a queue of ten data points at each instant. In order to calculate the peak of an action potential from the filtered data, the maximum change in voltage or upstroke of action potential was detected (panel C). The repolarization threshold was calculated based on the detected peak and was used to identify the end of the action potential and thus, to determine APD. In panel D, the application of a stimulus at the end of the detected APD is shown. Fig.7.4, thus shows that the APD detection algorithm can process instantaneous real-time raw data and identify an APD. Although the stimulus here is applied at the end of each detected APD, the algorithm can be used to control the DI and apply stimulation after a predefined constant DI. These results, thus present a novel real-time APD detection technique for the control of cardiac restitution and implementation of the constant DI pacing technique.

Alternans has been shown to be a local phenomenon that gradually develops spatially across the whole heart. The method described above, provides flexibility in terms of the number of action potentials sensed and their locations on the heart for feedback control information. This holds a distinct advantage compared to previous methods for the control of APD that were based on single electrode sensing and smaller tissue sizes.

This study was designed as a preliminary step to verify the feasibility of a novel optical mapping based real time feedback control system to capture and detect action potentials. A qualitative analysis of the proposed algorithm was performed. However, further quantitative studies are essential to characterize the efficacy and utility of the system. Also, the system used was a soft real time system limited by the inherent latencies of the camera frame grabber and Windows XP based PC. Further improvements in the performance and speed can be achieved using a hard real time system.

# REFERENCES

1. Fox JJ, JL McHarg, and RF Jr. Gilmour. Ionic mechanism of electrical alternans. Am. J. Physiol. Heart Circ. Physiol. vol. 282, no. 2, pp. H516– H530, 2002

2. Gilmour RF Jr. Electrical restitution and ventricular fibrillation: negotiating a slippery slope. J of Cardiovasc. Electrophysiol. 13:1150–1151, 2002

3. Karma A. Electrical alternans and spiral wave breakup in cardiac tissue. Chaos. vol. 4, no. 3, pp. 461–472, 1994

4. Watanabe M, NF Otani and RF Jr. Gilmour. Biphasic restitution of action potential duration and complex dynamics in ventricular myocardium. Circ. Res. vol. 76, no. 5, pp. 915–921, 1995

5. Escobar AL and HH Valdivia. Cardiac Alternans and Ventricular Fibrillation. Circulation Research. 2014;114:1369-1371, 2014

6. Rappel WJ, F Fenton, and A Karma. Spatiotemporal control of wave instabilities in cardiac tissue. Phys. Rev. Lett. Vol 83, 456, 1999

7. Tolkacheva EG, MM Romeo, M Guerraty and DJ Gauthier. Condition for alternans and its control in a two-dimensional mapping model of paced cardiac dynamics. Phys Rev E Stat Nonlin Soft Matter Phys. 69(3 Pt 1):031904, 2004

8. Kleiger RE, JP Miller, JT Bigger and AJ Moss. Decreased heart rate variability and its association with increased mortality after acute myocardial infarction. American Journal of Cardiology. 59:256, 1987

9. La Rovere MT, GD Pinna, R Maestri, A Mortara, S Capomolla, O Febo, R Ferrari, M Franchini, M Gnemmi, C Opasich, PG Riccardi, E Traversi and F Cobelli. Short-Term

Heart Rate Variability Strongly Predicts Sudden Cardiac Death in Chronic Heart Failure Patients. Circulation. 107:565, 2003

10. Huikuri HV and PK Stein. Heart rate variability in risk stratification of cardiac patients. Prog Cardiovasc Dis. 56(2):153-9, 2013

11. Xhyheri B, O Manfrini, M Mazzolini, C Pizzi and R Bugiardini. Heart rate variability today. Prog Cardiovasc Dis. 55(3):321-31, 2012

12. McIntyre SD, V Kakade, Y Mori and EG Tolkacheva. Heart rate variability and alternans formation in the heart: The role of feedback in cardiac dynamics. J. of Theo.l Biol. 7;350:90-7., 2014

13. Tolkacheva EG, DG Schaeffer, DJ Gauthier and W Krassowska. Condition for alternans and stability of the 1:1 response pattern in a "memory" model of paced cardiac dynamics. Phys. Rev. E. 67, 031904, 2003

14. Kalb SS, EG Tolkacheva, DJ Gauthier and E Krassowska. Restitution in mapping models with arbitrary amount of memory. Chaos. 15, 23701, 2005

15. Kalb SS, HM Dobrovolny, EG Tolkacheva, SF Idriss, W Krassowska and DJ Gauthier. The restitution portrait: a new method for investigating rate-dependent restitution. J. Cardiovasc. Electrophys. 15, 698, 2004

16. Nolasco JB and RW Dahlen. A graphic method for the study of alternation in cardiac action potentials. J. Appl. Physiol., 25, p.191, 1968

17. Koller ML, ML Riccio and RF Jr. Gilmour. Dynamic restitution of action potential duration during electrical alternans and ventricular fibrillation. Am. J. Physiol. 275, p. H1635, 1998

18. Linyuan J and A Patwardhan. Hysteresis in DI independent mechanisms in threshold for transition between 1:1 and 2:2 rhythms in pigs. Engineering in Medicine and Biology Society (EMBC), Annual International Conference of the IEEE, 2012

19. Patwardhan A and S Moghe. Novel feedback based stimulation protocol shows hysteresis in cardiac action potential duration restitution. Biomed Sci Instrum, 37:505-510, 2001

20. Wu R and A Patwardhan. Restitution of action potential duration during sequential changes in diastolic intervals shows multimodal behavior. Circulation. 94:634-641, 2004

21. Wu R and A Patwardhan A. Mechanism of repolarization alternans has restitution of action potential duration dependent and independent components. Journal of cardiovascular electrophysiology 17.1 (2006): 87-93, 2006

22. Zlochiver S, C Johnson and EG Tolkacheva. Constant DI pacing suppresses cardiac alternans formation in numerical cable models. Accepted for publication, Chaos. 2017

23. Malik M. Heart rate variability. Ann. Noninvasive Electrocardiol. 1: 151–181, 1996

24. Goldberger AL, LV Amaral, L Glass, JM Hausdorff, PC Ivanov, RG Mark, JE Mietus, GB Moody, CK Peng and HE Stanley. PhysioBank, PhysioToolkit, and PhysioNet: Components of a New Research Resource for Complex Physiologic Signals. Circulation. vol. 101, p. e215–e220, 2000

25. Nasir A, R Batra and R Jayasingle. A Clinical Review of Implantable Cardioverter Defibrillators and Bi-Ventricular Pacemakers at One Institute. Australasian Medical Journal. 1-1-23-27, 2010

26. Viskin S, M Glikson, R Fish, A Glick, Y Copperman and L A Saxon. Rate Smoothing with Cardiac Pacing for Preventing Torsade de Pointes. Am J of Cardiol. Vol. 86, 111K–115K, 2000

27. Wood MA and KA Ellenbgen. Cardiac Pacemakers From the Patient's Perspective. Circulation. 105, p2136-2138, 2002

28. Christini DJ and JJ Collins. Using chaos control and tracking to suppress a pathological nonchaotic rhythm in a cardiac model. 53(1):R49-R52, 1996

29. Hall K, DJ Christini, M Tremblay, JJ Collins, L Glass and J Billette. Dynamic Control of Cardiac Alternans. Physical Review Letters. 78, 4518, 1997

30. Hall GM and DJ Gauthier. Experimental Control of Cardiac Muscle Alternans. Physical Review Letters. 88(19):198102, 2002

31. Echebarria B and A Karma. Spatiotemporal control of cardiac alternans. Chaos. 12(3):923-930, 2002

32. Jordan PN and DJ Christini. Adaptive Diastolic Interval Control of Cardiac Action Potential Duration Alternans. J. of Cardiovasc. Electrophysiol. 15(10):1177-85, 2004

33. Christini DJ, ML Riccio, CA Culianu, JJ Fox, A Karma A. and RF Jr. Gilmour. Control of Electrical Alternans in Canine Cardiac Purkinje Fibers. Physical Review Letters. 96(10):104101, 2006

34. Kanu UB, S Iravanian, RF Gilmour and DJ Christini. Control of action potential duration alternans in canine cardiac ventricular tissue. IEEE Trans Biomed Eng., 894-904, 2011

35. Garfinkel, A, YH Kim, O Voroshilovsky, Z Qu, J R Kil, M H Lee, H S Karagueuzian, J N Weiss, and P S Chen. Preventing Ventricular Fibrillation by Flattening Cardiac Restitution. Proceedings of the National Academy of Sciences of the United States of America 97 (11). National Academy of Sciences: 6061–66, 2000

36. Nanthakumar K, J Jalife, S Massé, E Downar, M Pop, J Asta, H Ross, V Rao, S Mironov, E Sevaptsidis, J Rogers, G Wright and R Dhopeshwarkar. Optical Mapping of Langendorff-Perfused Human Hearts: Establishing a Model for the Study of Ventricular Fibrillation in Humans. American Journal of Physiology - Heart and Circulatory Physiology 293 (1), 2007

37. Xie X, R Visweswaran, PA Guzman, RM Smith, JW Osborn and EG Tolkacheva. The Effect of Cardiac Sympathetic Denervation through Bilateral Stellate Ganglionectomy on Electrical Properties of the Heart. American Journal of Physiology. Heart and Circulatory Physiology. 301 (1): H192-9, 2011

38. Kulkarni K, R Visweswaran, X Zhao and EG Tolkacheva. Characterizing spatial dynamics of bifurcation to alternans in isolated whole rabbit hearts based on alternate pacing. Biomed Res Int. 2015:170768, 2015

39. George AL Jr. Molecular and genetic basis of sudden cardiac death. The Journal of Clinical Investigation. vol. 123, no. 1, pp. 75–83, 2013.

40. Zipes DP and HJJ Wellens. Sudden cardiac death. Circulation. vol. 98, no. 21, pp. 2334–2351, 1998.

41. Petrie A and X Zhao. Estimating eigenvalues of dynamical systems from time series with applications to predicting cardiac alternans. Proceedings of The Royal Society of

London, Series A: Mathematical, Physical and Engineering Sciences, vol. 468, no. 2147, pp. 3649–3666, 2012.

42. SunJ , F Amellal, L Glass and J Billette. Alternans and period doubling bifurcations in atrioventricular nodal conduction. Journal of Theoretical Biology, vol. 173, no. 1, pp. 79–91, 1995.

43. Berger CM, X Zhao, DG Schaeffer, HM Dobrovolny, W Krassowska and DJ Gauthier. Period-doubling bifurcation to alternans in paced cardiac tissue: crossover from smooth to border-collision characteristics. Phys. Rev. Lett. vol. 99,#5, Article ID 058101, 2007.

44. Heldstab J, H Thomas, T Geisel and G Radons. Linear and nonlinear response of discrete dynamical systems. I. Periodic attractors. Zeitschrift fur Physik B Condensed Matter. vol. 50, no. 2, pp. 141–150, 1983.

45. Zhao X and DG Schaeffer. Alternate pacing of border collision period-doubling bifurcations. Nonlinear Dynamics. vol. 50, no. 3, pp. 733–742, 2007.

46. Zhao X, DG Schaeffer, CM Berger, DJ Gauthier and W Krassowska. Cardiac alternans arising from an unfolded border-collision bifurcation. Journal of Computational and Nonlinear Dynamics. vol. 3, no. 4, Article ID 041004, 2008.

47. Smith RM, R Visweswaran, I Talkachova, JK Wothe and EG Tolkacheva. Uncoupling the mitochondria facilitates alternans formation in the isolated rabbit heart. American Journal of Physiology—Heart and Circulatory Physiology, vol. 305, no. 1, pp. H9–H18, 2013.

48. Cram AR, HM Rao and EG Tolkacheva. Toward prediction of the local onset of alternans in the heart. Biophysical Journal, vol. 100, no. 4, pp. 868–874, 2011.

49. Weiss JN, A Karma, Y Shiferaw, PS Chen, A Garfinkel and Z Qu. From pulsus to pulseless: the saga of cardiac alternans. Circ. Res. vol. 98, no. 10, pp. 1244–1253, 2006

50. Kulkarni K, SW Lee SW and EG Tolkacheva. Pro-arrhythmic effect of heart rate variability during periodic pacing. Conf Proc IEEE Eng Med Biol Soc. Aug;2016:149-152, 2016.

51. van Ravenswaaij-Arts CMA, LAA Kollee, JCW Hopman, GBA Stoelinga and HP van Geijn. Heart Rate Variability. Annals of Internal Medicine. 118:436-447, 1993

52. Stauss HM. Heart rate variability. American Journal of Physiology - Regulatory, Integrative and Comparative Physiology. 285 (5) R927-R931, 2003

53. Dvir H and S Zlochiver. The interrelations among stochastic pacing, stability and memory in the heart. Biophysical Journal. 107(4):1023-34, 2014

54. Dvir H and S Zlochiver. Stochastic cardiac pacing increases ventricular electrical stability--a computational study. Biophysical Journal. 105(2):533-42, 2013

55. Dvir H and S Zlochiver. Stochastic pacing effect on cardiac alternans--simulation study of a 2D human ventricular tissue. Conf Proc IEEE Eng Med Biol Soc. 2013:1514-7, 2013

56. Prudat Y, RV Madhvani, M Angelini, NP Borgstom, A Garfinkel, HS Karagueuzian, JN Weiss, E de Lange, R Olcese and JP Kucera. Stochastic pacing reveals the propensity to cardiac action potential alternans and uncovers its underlying dynamics. J Physiol. 2015

57. Visweswaran R, SD McIntyre, K Ramkrishnan, X Zhao and EG Tolkacheva. Spatiotemporal evolution and prediction of $[Ca(^{2+})]_i$ and APD alternans in isolated rabbit hearts. J Cardiovasc Electrophysiol. 24(11):1287-95, 2013

58. Sookan T and AJ McKune. Heart rate variability in physically active individuals: reliability and gender characteristics. Cardiovasc J Afr. Mar;23(2):67-72. 2012

59. Banville I and RA Gray. Effect of action potential duration and conduction velocity restitution and their spatial dispersion on alternans and the stability of arrhythmias. J Cardiovasc. Electrophysiol. 13(11):1141-9, 2002

60. Sved AF, S Ito and JC Sved. Brainstem mechanisms of hypertension: role of the rostral ventrolateral medulla. Curr. Hypertens. Rep. 5:262–268, 2003

61. Guyenet PG. The sympathetic control of blood pressure. Nat. Rev. Neurosci. 7:335–346, 2006

62. Zhang Y, ZB Popović, S Bibevski, I Fakhry, DA Sica, DR Van Wagoner and TN Mazgalev. Chronic Vagus Nerve Stimulation Improves Autonomic Control and Attenuates Systemic Inflammation and Heart Failure Progression in a Canine High-Rate Pacing Model. Circulation: Heart Failure. 2:692-699, 2009

63. Bibevski S and ME Dunlap. Evidence for impaired vagus nerve activity in heart failure. Heart Fail. Rev. 16:129–135, 2011

64. Armour JA, DA Murphy, BX Yuan, S Macdonald and DA Hopkins. Gross and microscopic anatomy of the human intrinsic cardiac nervous system. Anat. Rec. 247:289–298, 1997

65. Randall DC, DR Brown, AS McGuirt, GW Thompson, JA Armour and JL Ardell. Interactions within the intrinsic cardiac nervous system contribute to chronotropic regulation. Am. J. Physiol. Regul. Integr. Comp. Physiol. 285:R1066–R1075, 2003

66. Ulphani JS, JH Cain, F Inderyas, D Gordon, PV Gikas, G Shade, D Mayor, R Arora, AH Kadish and JJ Goldberger. Quantitative analysis of parasympathetic innervation of the porcine heart. Heart Rhythm. 7:1113–1119, 2010

67. Coote JH. Myths and realities of the cardiac vagus. J. Physiol. 591(Pt 17): 4073–4085, 2013

68. Annoni EM, X Xie, SW Lee, I Libbus, BH KenKnight, JW Osborn and EG Tolkacheva. Intermittent electrical stimulation of the right cervical vagus nerve in salt-sensitive hypertensive rats: effects on blood pressure, arrhythmias, and ventricular electrophysiology. Physiol. Rep. 2015

69. Beaumont E, EM Southerland, JC Hardwick, GL Wright, S Ryan, Y Li, BH KenKnight, JA Armour and JL Ardell. Vagus nerve stimulation mitigates intrinsic cardiac neuronal and adverse myocyte remodeling postmyocardial infarction. Am. J. Physiol. Heart Circ. Physiol. 309:H1198–H1206, 2015

70. De Ferrari GM and PJ Schwartz. Vagus nerve stimulation: from pre-clinical to clinical application: challenges and future directions. Heart Fail. Rev. 16:195–203, 2011

71. Schwartz PJ and GM De Ferrari. Vagal stimulation for heart failure: background and first in-man study. Heart Rhythm. 6(11 Suppl.):S76–S81, 2009

72. Wickman K and DE Clapham. G-protein regulation of ion channels. Curr Opin Neurobiol. 5:278-85, 1995

73. DiFrancesco D, P Ducouret and RB Robinson. Muscarinic modulation of cardiac rate at low acetylcholine concentrations. Science. 243:669-71, 1989

74. Posokhova E, D Ng, A Opel, I Masuho, A Tinker, LG Biesecker, K Wickman and KA Martemyanov. Essential Role of the m2R-RGS6- I KACh Pathway in Controlling Intrinsic Heart Rate Variability. PloS one. 8:e76973, 2013

75. Yang J, J Huang, B Maity, Z Gao, RA Lorca, H Gudmundsson, J Li, A Stewart, PD Swaminathan, SR Ibeawuchi, A Shepherd, CK Chen, W Kutschke, PJ Mohler, DP Mohapatra, ME Anderson and RA Fisher. RGS6, a modulator of parasympathetic activation in heart. Circ Res. 107:1345-9, 2010

76. Posokhova E, N Wydeven, KL Allen, K Wickman and KA Martemyanov. RGS6/Gbeta5 complex accelerates I KACh gating kinetics in atrial myocytes and modulates parasympathetic regulation of heart rate. Circ Res. 107:1350-4, 2010

77. Wickman K, J Nemec, SJ Gendler and DE Clapham. Abnormal heart rate regulation in GIRK4 knockout mice. Neuron. 20:103-14, 1998

78. Rorabaugh BR, B Chakravarti, NW Mabe, SL Seeley, AD Bui, J Yang, SW Watts, RR Neubig and RA Fisher. Regulator of G Protein Signaling 6 Protects the Heart from Ischemic Injury. J.of Pharm. and Experimental Therapeutics. 360 (3) 409-416, 2017

79. Maity B, A Stewart, Y O'Malley, RW Askeland, SL Sugg and RA Fisher. Regulator of G protein signaling 6 is a novel suppressor of breast tumor initiation and progression. Carcinogenesis. 34 (8): 1747-1755, 2013

80. Yang J, B Maity, J Huang, Z Gao, A Stewart, RM Weiss, ME Anderson and RA Fisher. G-protein Inactivator RGS6 Mediates Myocardial Cell Apoptosis and Cardiomyopathy Caused By Doxorubicin. Cancer Res. (73) (6) 1662-1667, 2013

81. Stewart A, J Huang and RA Fisher. RGS proteins in heart: brakes on the vagus. Front Physiol. Apr 13;3:95, 2012.

82. Kovacs RJ and JC Bailey. Effects of acetylcholine on action potential characteristics of atrial and ventricular myocardium after bilateral cervical vagotomy in the cat. Circ Res. Apr;56(4):613-20, 1985

83. Verkerk AO, GSC Geuzebroek, MW Veldkam and R Wilders. Effects of Acetylcholine and Noradrenalin on Action Potentials of Isolated Rabbit Sinoatrial and Atrial Myocytes. Frontiers in Physiology. 3:174, 2012

84. Ravens U, C Poulet, E Wettwer and M Knaut. Atrial selectivity of antiarrhythmic drugs. The Journal of Physiology. 591: 4087–4097, 2013

85. Ravens U and A Zielgler. Effects of Carbachol on Contractile Force and Action Potentials of Isolated Atria at Different Rates of Stimulation. Journal of Cardiovascular Pharmacology. 1980

86. Martins JB and DP Zipes. Epicardial phenol interrupts refractory period responses to sympathetic but not vagal stimulation in canine left ventricular epicardium and endocardium. Circ Res. 1980

87. Ng GA, KE Brack KE and JH Coote. Effect of direct sympathetic and vagus nerve stimulation on the physiology of the whole heart – a novel Langendorff perfused rabbit heart with intact dual autonomic innervation. Exp Physiol. 2001

88. Brack KE, JH Coote JH and GA Ng. Vagus nerve stimulation protects against ventricular fibrillation independent of muscarinic receptor activation. Cardiovasc Res. 91(3):437-46, 2011.

89. Brack KE, VH Patel, JH Coote and GA Ng. Nitric oxide mediates the vagal protective effect on ventricular fibrillation via effects on action potential duration restitution in the rabbit heart. The Journal of Physiology. 583: 695–704. 2007

90. Kulkarni K and EG Tolkacheva. Real-time feedback based control of cardiac restitution using optical mapping. Conf Proc IEEE Engineering in Medicine and Biology Society, 5920 - 5923, 2015